



UNIVERSITÀ DEGLI STUDI DI CAGLIARI

DOTTORATO DI RICERCA IN FISICA

Ciclo XXVI

**STUDIES ON MONOLITHIC ACTIVE PIXEL SENSORS AND
DETECTOR PERFORMANCE FOR THE INNER TRACKING
SYSTEM UPGRADE OF ALICE**

Settore scientifico disciplinare di afferenza
FIS/04

Presentata da:	Sabyasachi Siddhanta
Coordinatore Dottorato:	Prof. Paolo Ruggerone
Relatore:	Prof. Gianluca Usai

Esame finale anno accademico 2012-2013



कर्मण्येवाधिकारस्ते मा फलेषु कदाचन।
मा कर्मफलहेतुर्भूर्मा ते सङ्गोऽस्त्वकर्मणि॥

श्रीमद्भगवद्गीता

Πάντες ἄνθρωποι τοῦ εἰδέναι ὀρέγονται φύσει.

τὰ μετὰ τὰ φυσικά - Ἀριστοτέλης

Felix qui potuit rerum cognoscere causas
atque metus omnis et inexorabile fatum
subiecit pedibus strepitumque Acherontis avari

Georgica, II, 489 - Vergilius

Fatti non foste per viver come bruti, ma per seguir virtute e canoscenza

Canto XXVI, Inferno - Dante Alighieri

জ্ঞানর মাঝে অজ্ঞানার করেছি পঙ্কান,

বিস্মরে তাই জাগে আমার গান ।।

রবীন্দ্রনাথ ঠাকুর

Contents

1	ALICE Inner Tracking System Upgrade	1
1.1	Introduction	1
1.1.1	ALICE (A Large Ion Collider Experiment)	1
1.1.2	ALICE upgrade strategy	3
1.2	ALICE Inner Tracking System upgrade	4
1.2.1	Current ITS	4
1.2.2	Physics motivations for the ITS upgrade	5
1.2.3	Current ITS limitations and improvement possibilities with the ITS upgrade	7
1.2.4	ITS upgrade concept	9
1.3	Document summary	11
2	Monolithic Active Pixel Sensors for ALICE Upgrade	13
2.1	Detection principle of semiconductors	13
2.1.1	Interaction with charged particles	13
2.1.2	Interaction with electromagnetic radiation	15
2.1.3	Detection principle	16
2.2	Monolithic Active Pixel Sensors for ALICE	17
2.2.1	Detector Technology	19
2.2.2	Principle of Operation of MAPS	19
2.2.2.1	MAPS in a standard CMOS process	19
2.2.2.2	Detection principle in MAPS	21
2.2.2.3	Front end readout	21
2.2.3	MAPS prototypes for the ALICE ITS upgrade	22

CONTENTS

3	Characterisation of Monolithic Active Pixel Sensors	25
3.1	Observables and Methods	25
3.1.1	Correlated Double Sampling	25
3.1.2	Laboratory measurements with ^{55}Fe source	26
3.1.3	Measurements with minimum ionizing particles	31
3.1.4	Measurements for irradiated chips	31
3.2	MIMOSA32 and MIMOSA32Ter	32
3.2.1	Test set up for MIMOSA32 and MIMOSA32Ter	35
3.2.2	Characterization of MIMOSA32 and MIMOSA32Ter	37
3.2.2.1	MIMOSA32	37
3.2.2.2	Tests with irradiated MIMOSA32	41
3.2.2.3	MIMOSA32Ter	42
3.2.2.4	Tests with irradiated MIMOSA32Ter	45
3.2.3	MIMOSA32 and MIMOSA32Ter tests summary	46
3.3	Explorer	47
3.3.1	Design motivation	47
3.3.2	Explorer prototypes	49
3.3.3	Characterization of Explorer-1	52
3.3.3.1	Tests with standard epitaxial layer thickness (18 μm)	52
3.3.3.2	Comparison between different starting materials	56
3.3.3.3	Tests with irradiated chips	60
3.3.4	Explorer-1 tests summary	62
3.4	Developments towards a full scale pixel chip	64
3.4.1	MISTRAL	64
3.4.2	ASTRAL	66
3.4.3	CHERWELL	67
3.4.4	ALPIDE	67
3.5	Future plans	69
4	Detector Performance	71
4.1	Introduction	71
4.2	Experimental conditions (ALICE Run 3) for simulation studies	72
4.3	Detector specification	75

4.3.1	Number of layers and their radii:	75
4.3.1.1	Layout overview	75
4.3.1.2	Layer radii optimization	77
4.3.2	Material budget:	78
4.3.3	Detector intrinsic resolution:	78
4.3.4	Acceptance:	79
4.3.5	Timing and readout rate:	80
4.4	Simulation tools	80
4.5	Detector performance studies	81
4.5.1	Comparison with the current ALICE ITS	81
4.5.1.1	Impact parameter resolution	81
4.5.1.2	Momentum resolution	84
4.5.1.3	Tracking efficiency	86
4.5.2	Performance for improved or degraded sensor parameters	86
4.5.2.1	Performance with variations in the sensor intrinsic res- olution	87
4.5.2.2	Performance with variations in the material budget	89
4.5.3	Performance with a further reduction of beam pipe radius	92
4.5.4	Redundancy studies	94
5 Conclusion		99
Acknowledgements		101
Thank you ..		103
Bibliography		105

CONTENTS

1

ALICE Inner Tracking System Upgrade

Contents

2.1	Detection principle of semiconductors	13
2.2	Monolithic Active Pixel Sensors for ALICE	17

1.1 Introduction

1.1.1 ALICE (A Large Ion Collider Experiment)

ALICE (A Large Ion Collider Experiment) is a general-purpose, heavy-ion detector at the CERN LHC. It is designed to study the physics of strongly interacting matter, and in particular the properties of the Quark-Gluon Plasma (QGP), using nucleus-nucleus collisions at unprecedented energy densities. Lead (Pb) nuclei are used as the heavy ion for these collisions. Apart from Pb–Pb collisions, ALICE also does precision measurements with proton-proton (pp) and proton-lead (p-Pb) collisions to provide a reference for the Pb–Pb collisions. The scientific plans and detector specifications of ALICE are defined in the ALICE Physics Performance Report Vol. I [1] and Vol. II [2]. An updated description of the ALICE detector can be found in [3].

The apparatus of ALICE (Fig.1.1) consists of a central barrel and a forward muon spectrometer along with some smaller detectors for trigger and event characterisation.

1. ALICE INNER TRACKING SYSTEM UPGRADE

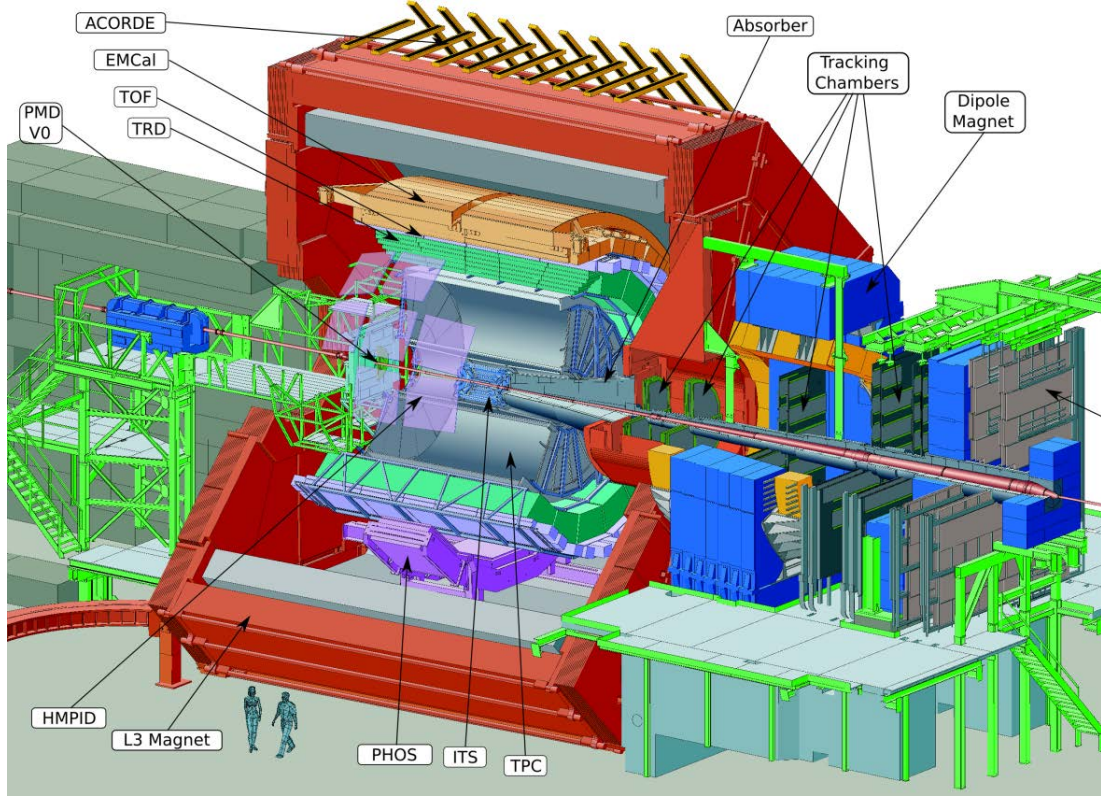


Figure 1.1: ALICE detector

The central barrel is mounted inside a solenoidal magnet which provides a magnetic field of 0.5 T parallel to the beam axis. The detectors in the central barrel are mainly dedicated to vertex reconstruction, tracking, particle identification and momentum measurement. The main tracking detectors in the central barrel are the Time Projection Chamber (TPC) and the Inner Tracking System (ITS). The ITS performs vertexing and is composed of six layers of silicon detectors: two layers each of Silicon Pixel Detector (SPD), Silicon Drift Detector (SDD) and Silicon Strip Detector (SSD). The other detectors in the central barrel are the Time Of Flight (TOF) detector for particle identification, High Momentum Particle Identification (HMPID), the Transition Radiation (TRD) counters for electron identification and two electromagnetic calorimeters - PHOTon Spectrometer (PHOS) and ElectroMagnetic CALorimeter (EMCAL). There are other smaller detectors for trigger and multiplicity measurement: the Photon Multiplicity Detector (PMD), Forward Multiplicity Detector (FMD), V0 and T0. There are two sets of hadronic calorimeters which provides the centrality measurements: the

Zero Degree Calorimeters (ZDC) located on both sides of ALICE along the beam line at 115 m from the interaction point. In addition, there is an array of scintillators (ALICE COsmic Ray DEtector, ACORDE) installed on top of the solenoid to trigger on cosmic rays for calibration purposes.

The forward muon spectrometer designed to study single muons and dimuons, consists of a combination of tracking and trigger chambers, absorbers and a dipole magnet.

Equipped with these wide range of detectors, ALICE enables a comprehensive study of hadrons, electrons, muons, and photons produced in the Pb–Pb collisions.

1.1.2 ALICE upgrade strategy

During the first three years of running (two years of Pb–Pb and one year of p-Pb), ALICE has already demonstrated very good capabilities for measurements at high energy nucleus collisions. Before the start of the LHC, results from the experiments at CERN SPS and BNL RHIC suggested that QGP is an almost perfect liquid. ALICE has confirmed this basic picture and observed the creation of hot hadronic matter at unprecedented temperature and densities. In only three years, ALICE has exceeded the precision and kinematic reach of all significant probes of the QGP measured in the last decade.

However, there are certain measurements like high precision measurements of rare probes over a broad range of momenta (specially at low p_T), which are not possible or not satisfactory with the present experimental setup. This scenerio can be improved significantly by detector upgrades combined with an increase in luminosity, thus enhancing the physics capabilities of ALICE greatly. This forms the starting motivation for ALICE upgrade program planned to be implemented during the LHC long shutdown two (LS2) in 2018-2019.

The upgrade strategy for ALICE is formulated on the fact that after LS2, LHC will provide Pb–Pb collisions at an interaction rate of upto 50 kHz corresponding to an instantaneous luminosity, $\mathcal{L} = 6 \times 10^{27} \text{cm}^{-2}\text{s}^{-1}$. To cope with this luminosity and to perform the measurements defined by the upgrade program, detector upgrades are necessary. The detector upgrades should help to improve tracking and vertexing capabilities, radiation hardness and allow for readout of all interactions to accumulate enough statistics for the upgrade physics program. The objective is to accumulate 10nb^{-1} of Pb–Pb collisions, recording about 10^{11} interactions.

1. ALICE INNER TRACKING SYSTEM UPGRADE

The upgrades include:

- A new beampipe with smaller diameter.
- A new, high-resolution, low-material Inner Tracking System (ITS).
- Upgrade of the Time Projection Chamber (TPC), consisting of the replacement of the wire chambers with Gas Electron Multiplier (GEM) detectors and new pipelined read-out electronics.
- A new Muon Forward Telescope (MFT) to add vertexing capabilities to the current Muon Spectrometer.
- Upgrade of the read-out electronics of Transition Radiation Detector (TRD), Time Of Flight detector (TOF), and Muon Spectrometer for high rate operation.
- Upgrade of the forward trigger detectors.
- Upgrade on the online systems and offline reconstruction and analysis framework.

1.2 ALICE Inner Tracking System upgrade

1.2.1 Current ITS

The current ITS consists of six layers of silicon detectors placed coaxially around the beam pipe (Fig.1.2) with their radii ranging from 3.9 cm to 43 cm. They cover a pseudorapidity range of $|\eta| < 0.9$ for vertices located within $z = \pm 60$ mm with respect to the nominal interaction point ($\pm 1\sigma$ of the luminous region). To sustain a high particle hit density and to perform an efficient vertex reconstruction, the first two layers were made of Silicon Pixel Detectors (SPD) with state-of-the-art hybrid pixel detectors. The two middle layers are made of Silicon Drift Detectors (SDD) followed by two layers of double sided Silicon Strip Detectors (SSD). The last four layers have analog readout with PID capabilities through dE/dx measurement in the non-relativistic ($1/\beta^2$) region.

The ITS is localized using the ALICE Global Reference system: z axis on the beam line, x axis in the LHC (horizontal) plane, pointing to the center of the accelerator, and the y axis pointing upward. In the transverse plane, the cylindrical coordinates and r and ϕ localize the radial coordinate of the point with respect the center of axis and the azimuthal angle, respectively.

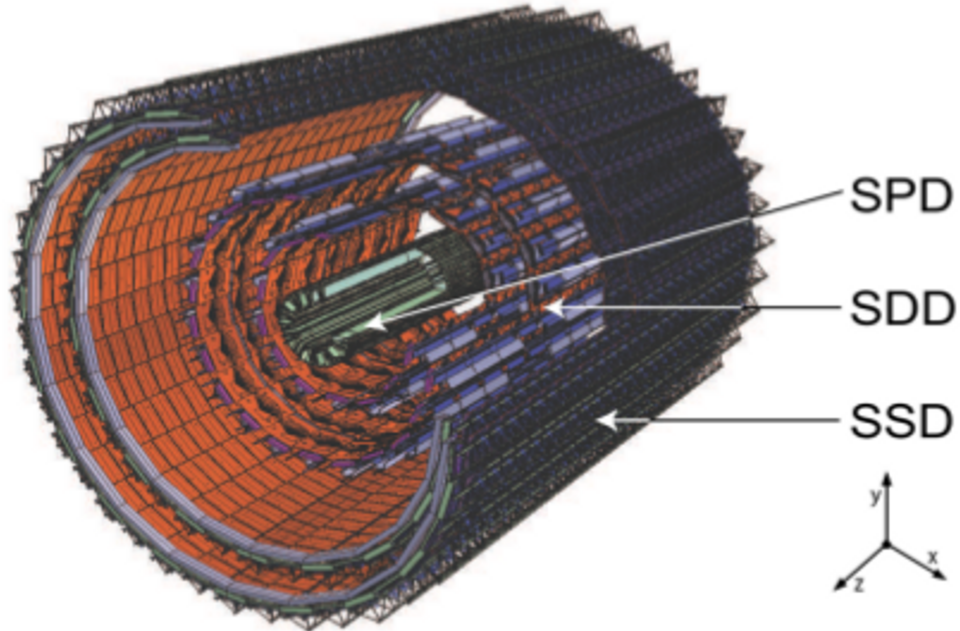


Figure 1.2: The current Inner Tracking System of ALICE. It consists of six layers of silicon detectors placed coaxially around the beam pipe. The first two layers consist of Silicon Pixel Detectors (SPD) with hybrid pixel detectors. The two middle layers are made of Silicon Drift Detectors (SDD) followed by two layers of double sided Silicon Strip Detectors (SSD).

The layer parameters were optimized for efficient tracking performance in combination with the TPC and high precision in determining the charged particle distance of closest approach to the primary vertex. Thus, the first layer has a radius as small as possible, defined by the radius of the beam pipe. The outermost radius was defined in a way to optimize the track matching efficiency with the TPC. The first layer has an acceptance of $|\eta| < 1.98$, which along with the FMD gives continuous coverage to the charge particle multiplicity. The layer parameters are shown in Table 4.2 in Chapter 4, where a performance comparison is made between the current and the upgraded ITS (Section 4.5), specifically in terms of tracking efficiency and resolutions.

1.2.2 Physics motivations for the ITS upgrade

The long-term physics goal of ALICE is to study and provide a characterisation of the Quark Gluon Plasma (QGP) state of matter. This requires the measurement of

1. ALICE INNER TRACKING SYSTEM UPGRADE

heavy-flavour hadrons, quarkonia, and low-mass dileptons at low transverse momenta, together with novel measurements of jets and their constituents. To achieve this goal, high statistics measurements are required, as these will give access to the very rare physics channels needed to understand the dynamics of QGP. The ALICE long-term physics goals, its experimental strategy and the upgrade plans are discussed in the ALICE Upgrade Letter of Intent [4], its addendum [5] and in the ALICE Inner Tracking System Upgrade Technical Design Report [6].

The primary scope of ITS upgrade is to provide measurements for heavy-flavour interactions with the QGP medium with highly improved tracking and readout capabilities. These measurements include:

- Study of the thermalisation of heavy quarks, specially charm and beauty in the QGP. This is possible by measuring the baryon/meson ratio for charm (Λ_c/D) and for beauty (Λ_b/B) and the azimuthal anisotropy, v_2 for charm mesons and baryons. At low momentum the azimuthal anisotropy is determined by the elliptic flow, which provides the most direct evidence of the collective hydrodynamical behaviour of the medium. In this respect, the new ITS will have a significant impact on the following measurements:
 - D mesons, including D_s , down to zero p_T will be accessible for the first time.
 - Charm and beauty baryons, Λ_c and Λ_b . The former will be measured, for the first time, through the decay $\Lambda_c \rightarrow pK^- \pi^+$. The latter will be measured through the decay $\Lambda_b \rightarrow \Lambda_c + X$. and also this will be accessible for the first time.
 - Baryon/meson ratios for charm (Λ_c/D) and for beauty (Λ_b/B), will also be accessible for the first time.
 - The elliptic flow of charmed and beauty mesons and baryons down to low p_T will also be accessible for the first time.
- In-medium energy loss of the high momentum partons are measured in terms of the nuclear modification factor (R_{AA}) as a function of p_T of the open heavy flavours. This energy loss can also be measured via the semi-leptonic decay channel. The new ITS will significantly improve or make accessible for the first time the following measurements in Pb–Pb collisions:

- Measurement of beauty via the decay channels $B \rightarrow D + X$, $D^0 \rightarrow K\pi$, which will be accessible for the first time.
- Measurement of beauty via displaced $J/\psi \rightarrow ee$, which will also be accessible for the first time.
- Improve measurement of single displaced electrons.
- Improve beauty decay vertex reconstruction, using any of the previous three channels plus an additional track.

Additionally, the new ITS will also allow the measurement of low-mass dielectrons. This measurement gives access to:

- Thermal radiation from the QGP, via real and virtual photons detected as dielectrons.
- In-medium modifications of hadronic spectral functions related to chiral symmetry restoration, in particular for the ρ meson in its e^+e^- decay mode.

1.2.3 Current ITS limitations and improvement possibilities with the ITS upgrade

As far as the physics performance in heavy flavour detection is concerned, the current ITS have significant limitations. For example, the study of charm baryons is not feasible with the current setup. The current ITS has an impact parameter resolution larger than the decay length of Λ_c ($c\tau \approx 60 \mu\text{m}$ [7]) which is the most abundantly produced charm baryon, thus making it inaccessible in Pb–Pb collisions in ALICE.

Another disadvantage of the current ITS is its limited readout capabilities: a maximum rate of 1 kHz (with dead time close to 100%), irrespective of the detector occupancy. This is a crucial limitation since it prevents ALICE to exploit the full Pb–Pb collision rate of 8 kHz, which the LHC can deliver presently. This results in inadequate statistics, specially for the physics channels which cannot be selected by a trigger. This renders the current ITS incompatible with the long term physics plans of ALICE.

Finally, the present ITS is inaccessible for maintenance and repair interventions during the yearly LHC shutdowns. This could lead to a significant compromise in maintaining high data quality. So, it is a high priority in the design of the upgraded ITS to have rapid accessibility.

1. ALICE INNER TRACKING SYSTEM UPGRADE

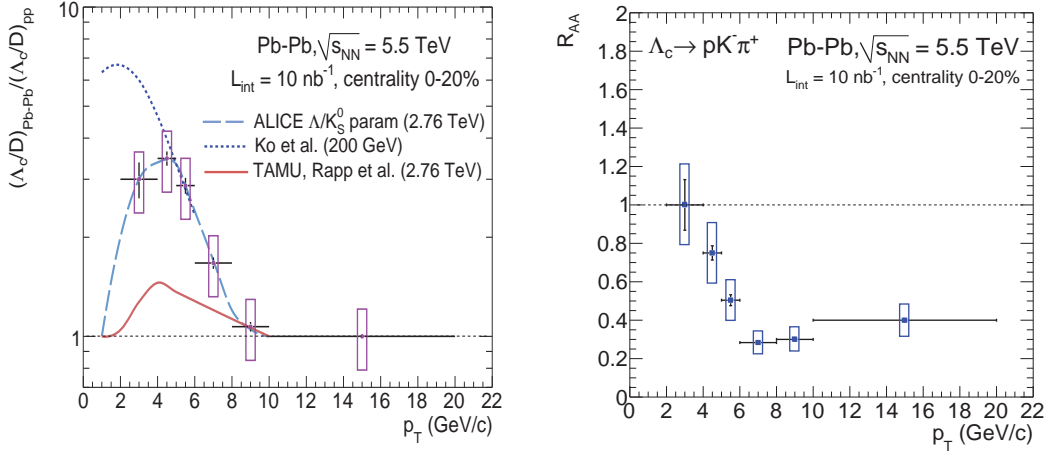


Figure 1.3: Left: Enhancement of the Λ_c/D ratio in central Pb–Pb (0 – 20%) for $L_{\text{int}} = 10 \text{ nb}^{-1}$ with respect to pp collisions. Two model calculations [8],[9] are also shown. Right: Λ_c nuclear modification factor (R_{AA}) in central Pb–Pb collisions (0 – 20%) for $L_{\text{int}} = 10 \text{ nb}^{-1}$.

The physics performance studies for the new ITS predicts the enhancement of the Λ_c/D_0 ratio in central Pb–Pb (0 – 20%) for $L_{\text{int}} = 10 \text{ nb}^{-1}$ with respect to pp collisions. This is shown in the left panel of Fig.1.3. It is assumed that the statistical uncertainties for the D_0 measurements and for the Λ_c measurement in pp are negligible with respect to those for the Λ_c measurement in Pb–Pb. The points are drawn on a line that captures the trend and magnitude of the Λ/K_0 double-ratio. Two model calculations [8],[9] are shown to illustrate the expected sensitivity of the measurement.

The right panel of Fig. 1.3 shows the $\Lambda_c R_{AA}$ as a function of p_T in central Pb–Pb collisions (0 – 20%) for $L_{\text{int}} = 10 \text{ nb}^{-1}$. Also in this case, it is assumed that the statistical uncertainties for the Λ_c measurement in pp are negligible with respect to those in Pb–Pb. The prompt $D^0 R_{AA}$ is also shown for comparison.

On the other hand, to study the production of charm mesons in exclusive decay channels (e.g. $D^0 \rightarrow K\pi$ and $D^+ \rightarrow K\pi\pi$), the impact parameter of the current ITS is adequate, but only in a certain transverse momentum range. At $p_T < 1 \text{ GeV}/c$, the statistical significance of the measurements is insufficient. The left panel of Fig.1.4 shows the measurement of D meson R_{AA} using ALICE data from 2010 and 2011. The analysis was restricted to $p_T > 2 \text{ GeV}/c$ with the 2010 data[10] and to $p_T > 1 \text{ GeV}/c$ using higher-statistics data from the 2011 Pb–Pb run[11]. Reaching zero transverse momentum

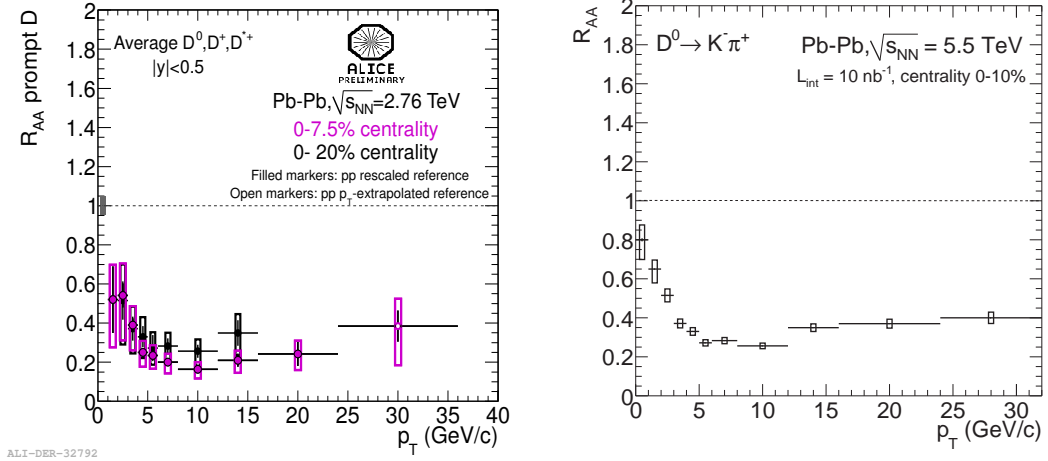


Figure 1.4: Left: Comparison of average D meson R_{AA} vs p_T in $|y| < 0.5$ in 0–20% (2010 data)[10] and 0–7.5% (2011 data) central Pb–Pb events[11]. Right: Nuclear modification factor of prompt D^0 mesons in central Pb–Pb for $L_{int} = 10 \text{ nb}^{-1}$ with statistical and systematic uncertainties.

seems to be precluded with the current setup, due to the large background level. In addition, the present accuracy of the R_{AA} measurement is limited to 30–40% by the systematic uncertainties on the B feed-down correction, the signal yield extraction, and the efficiency evaluation. All these contributions could be substantially reduced with an upgraded vertex detector. The right panel of Fig.1.4 shows the nuclear modification factor of prompt D^0 with the systematic and the statistical uncertainties expected for 8.5×10^9 central (0–10%) Pb–Pb events, corresponding to $L_{int} = 10 \text{ nb}^{-1}$.

The study of beauty mesons and beauty baryons would also be possible with the upgraded ITS, since their production would be enhanced in the upgrade scenario, thanks to the high interaction rate and the improved impact parameter resolution.

1.2.4 ITS upgrade concept

Based on the upgrade physics motivations and the limitations of the present ITS, the design motivations for the upgraded ITS are:

- Highly efficient tracking, both in standalone mode and in association with the TPC, over an extended momentum range, with special emphasis on very low momenta.

1. ALICE INNER TRACKING SYSTEM UPGRADE

- Very precise reconstruction of secondary vertices from decaying charm and beauty hadrons.

The requirement for an efficient tracking in ITS standalone mode and in combination with the TPC drove the design and geometry of the layers of the upgraded ITS. This translates to a barrel geometry with seven layers and their radii optimized to fit the tracking requirements. This is discussed in Section 4.3.

As demonstrated in [12], the two possible options for the ITS Upgrade were as follows:

- inner layers consisting of silicon pixel detectors with binary readout and the outer layers with silicon strip detectors with analog readout measuring the ionisation in silicon, and
- all layers consisting of monolithic pixel detectors.

Recent studies [6] on the assesment of PID capabilities motivated the selection of the layout consisting of all layers of monolithic pixel detectors with binary readout. The new detector will not measure the ionisation in the silicon layers. PID capabilities of this layout were studied on benchmark measurements of the upgrade programme which should be most sensitive to low-momentum PID, namely the low-mass di-electron analysis and the $\Lambda_c \rightarrow pK\pi$ reconstruction. These studies confirmed that the new ITS with the same PID capabilities as the current ITS would have only a marginal improvement on the selected benchmark channels.

The requirement for improved vertexing capability translates to an improved impact parameter resolution. In the upgrade scenerio, there are two facts to consider in this respect, which guided the design considerations of the sensors:

- installation of a narrower beam pipe;
- increase in the interaction rate.

A narrower beam pipe would enable the installation of the first layer closer to the primary vertex which would in turn improve the impact parameter resolution. This, coupled with the higher interaction rate would need the sensor to be sufficiently radiation hard which was a requirement for the choice of the sensor

technology. The sensor should also have faster readout rates to readout all the interactions.

To improve the impact parameter resolution, one would need to reduce the effects of multiple scattering in the innermost layers. This can be ensured by reducing the material budget of the innermost layers. This in turn would require thin sensors, which drove the choice of monolithic pixels for ITS upgrade.

Another requirement for improving the impact parameter resolution is to improve the detector intrinsic resolution. This translates to a requirement of pixels with small feature size. This drove the choice of the TowerJazz 0.18 μm technology for the monolithic pixels.

The motivations behind the choice of monolithic pixels using TowerJazz 0.18 μm technology is discussed in Section 2.2.

A detailed discussion on the contributions to the improvement of the impact parameter resolution is done in Section 4.5.1.1. The specifications for the upgraded ITS is discussed in Section 4.3.

1.3 Document summary

This document is organized in the following manner. Chapter 2 gives an overview of the principle of operation of Monolithic Active Pixel Sensors (MAPS) and the motivation behind the adopted technology for ALICE ITS upgrade.

Chapter 3 presents the test procedures and observables for characterising the analog prototype circuits developed for the optimization of the sensor performance for the ITS upgrade, followed by the results of the tests conducted on some of the prototype circuits.

Chapter 4 discusses the performance of the upgraded ITS with its expected final layout and studies the effects of varying parameters for optimizing the final specifications.

Chapter 5 concludes this document with an outlook for the future of the ITS Upgrade programme.

1. ALICE INNER TRACKING SYSTEM UPGRADE

2

Monolithic Active Pixel Sensors for ALICE Upgrade

Contents

3.1	Observables and Methods	25
3.2	MIMOSA32 and MIMOSA32Ter	32
3.3	Explorer	47
3.4	Developments towards a full scale pixel chip	64
3.5	Future plans	69

2.1 Detection principle of semiconductors

The detection principle of semiconductor detectors is based on the detection of charge carriers generated by the interaction of radiation or charge particles with the material (sensor) of the detector. The interaction process depends on the type, charge or energy of the particles traversing the sensor material.

2.1.1 Interaction with charged particles

The charge particles traversing the sensor undergo scattering processes with the electrons of the interacting medium. These processes are dominant for particles heavier than electrons and can be characterized by the average energy loss suffered by the particle,

2. MONOLITHIC ACTIVE PIXEL SENSORS FOR ALICE UPGRADE

expressed by the Bethe-Bloch formula [13].

$$-\frac{dE}{dx} = \kappa z^2 \cdot \frac{Z}{A} \frac{1}{\beta^2} \left[\frac{1}{2} \ln \frac{2m_e c^2 \beta^2 \gamma^2 T_{\max}}{I^2} - \beta^2 \right] \quad (2.1)$$

with,

$$\kappa = 4\pi N r_e^2 m_e c^2 = 0.307075 \text{MeVcm}^2 \quad (2.2)$$

where,

N = Avogadro number,

z = charge of the traversing particle in units of the electron charge,

r_e = the classical electron radius,

$m_e c^2$ = electron rest mass energy,

Z = atomic number of the sensor material,

A = atomic mass of the sensor material,

I = mean excitation energy,

β = velocity of the traversing particle in units of the speed of light,

γ = Lorentz factor $\left(\frac{1}{\sqrt{1-\beta^2}} \right)$.

There are additional correction terms, like the density correction for high particle energies and the shell correction for lower energies[7]. The maximum kinetic energy which can be transferred to an electron by a particle of mass M is

$$T_{\max} = \frac{2m_e c^2 \beta^2 \gamma^2}{1 + 2\gamma m_e/M + (m_e/M)^2} \quad (2.3)$$

For particles much heavier than electrons, $M \gg m_e$, the energy loss mainly depends on β and γ . However, at high energy, the Lorentz factor, γ can have comparable magnitude to the ratio m_e/M and cannot be neglected. For electrons and positrons, corrections to the Bethe-Bloch formula are required since they interact in the traversing medium with identical particles (i.e. electrons) and additional energy loss mechanisms like bremsstrahlung have to be considered[14].

For low energies, the energy loss is dominated by the factor $1/\beta^2$. For a particle velocity of $\beta = 0.96$, the energy loss from the Bethe-Bloch equation 2.1 reaches a

2.1 Detection principle of semiconductors

minimum. A particle with an energy loss in the minimum of the Bethe-Bloch formula is called a minimum ionizing particle (MIP).

The number of charge carriers (electron and holes) generated in the semiconductor by the traversing particle is determined by dividing the deposited energy by the mean energy required for ionization (3.6 eV for silicon).

The ionization process during the passage of a charge particle through matter is subject to statistical fluctuation resulting in fluctuations of the energy loss in the medium. The equation 2.1 gives the average energy loss per path unit. The probability distribution of the energy loss depends on the thickness of the absorber. For thick absorbers, the energy loss distribution has a Gaussian shape. In thin absorbers, the fluctuation is higher and the distribution is asymmetric. For silicon sensors, the energy loss distribution was calculated by Landau[15] and Vavilov [16]. Further corrections were incorporated later by Blunck and Leisegang[17], Shulek[18] and Bichsel[19].

Apart from energy loss, charged particles traversing a detector suffers from Multiple Coulomb Scattering. This results in small deviations of the track due to successive small angle deflections symmetrically distributed around the incident direction. The scattering angle follows roughly a Gaussian distribution[20] with an rms of

$$\theta_{\text{rms}} = \frac{13.6 \text{ MeV}}{\beta \cdot p \cdot c} \cdot z \cdot \sqrt{\frac{X}{X_0}} [1 + 0.038 \log(\frac{X}{X_0})] \quad (2.4)$$

where β , p and z are the velocity, momentum and charge of the particle, respectively. The thickness of the detector material through which the particle traversed is represented by X and X_0 is the radiation length for the scattering medium. The ratio $\frac{X}{X_0}$ (material budget) gives the thickness of the absorption medium in units of radiation length.

The performance of semiconductor tracking and vertex detectors, in particular the impact parameter resolution is affected by the multiple scattering effects, This is discussed in Section 4.5.1.1.

2.1.2 Interaction with electromagnetic radiation

Electromagnetic radiation interact in semiconductor detectors in the form of three main processes: photoelectric effect, Compton effect and pair production. In these interactions, the incident radiation is either completely absorbed in the sensor material like

2. MONOLITHIC ACTIVE PIXEL SENSORS FOR ALICE UPGRADE

in photoelectric effect and pair production or is scattered (Compton effect). Thus, a monochromatic photon beam traversing the sensor material is attenuated in intensity:

$$I(x) = I_0 e^{-x/\mu} \quad (2.5)$$

where I_0 and $I(x)$ are the initial and final beam intensity after traversing a material of thickness x . The attenuation length, μ is the property of the medium and depends on the photon energy. At low energies (below 100 keV for silicon), photoelectric effect is the dominant process. At higher energies, the scattering process becomes dominant. Silicon is used for photon detection up to energies of about 100 keV. A detailed description of these processes can be found in literature [14].

2.1.3 Detection principle

The simplest semiconductor detector is based on a reverse biased diode (Fig. 2.1). Electromagnetic radiation interacting with the semiconductor would produce electron-hole pairs near the point of interaction whereas charged particles would produce electron-hole pairs along their path through the semiconductor. The produced charge carriers move by drift due to the applied reverse bias or by diffusion due to concentration variation and are collected by the electrodes associated to the front end readout electronics.

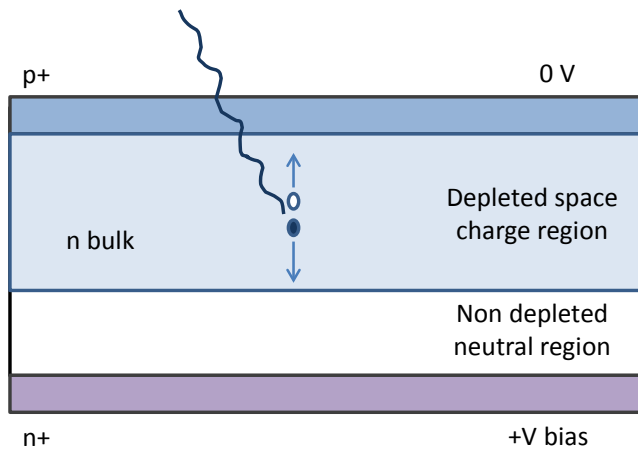


Figure 2.1: Schematic structure of a reverse biased semiconductor diode used as photon detector and connected to a read-out amplifier.

2.2 Monolithic Active Pixel Sensors for ALICE

Presently, silicon based semiconductor sensors and CMOS technology based front end readout electronics form the basis of the innermost vertexing and tracking detection systems in particle physics experiments, catering to the stringent requirements in terms of material budget, granularity, power consumption, readout speed and radiation hardness. The innermost vertexing and tracking detectors in the experiments at the LHC (ATLAS, CMS, LHCb, ALICE) use state of the art hybrid pixel detectors. A hybrid pixel detector is schematically illustrated in Fig.2.2 left. In these detectors, the silicon sensor and the front end readout electronics are separate components attached by bump-bonding.

The advantage of this technology is that the sensor and the frontend chip can be optimized separately and sensor materials other than silicon can be used. The technology for the different parts of the detector are provided by standard industrial processes and are available from a large number of industrial vendors.

However, there are technical limitations of this technology and the hybrid pixel detectors used in the LHC experiments are already optimized close to these limits. The main limitations are related to the bump bonding technology and the power density. Another limitation is that the front end electronics is confined to the same area as the detecting electrode. The projected pixel size in a $0.1\ \mu\text{m}$ CMOS technology could be as small as $10 \times 80\ \mu\text{m}^2$ or $25 \times 25\ \mu\text{m}^2$ for a square geometry. This leads to an estimated power density of $30\ \text{mW mm}^{-2}$ or $30\ \text{kW m}^{-2}$ detector [13]. The pitch for the PbSn bump bonding technology is limited to about 10-15 μm .

For the LHC upgrade scenario, pixel detectors are considered for a larger area coverage than the existing detectors. Upgrade requirements are driven by the demands on high resolution (i.e. small size), low material budget, low power density and high speeds. The present hybrid technology with one-to-one coverage of the area with the sensor, frontend chips and module interconnect layer would contribute to a significant material budget issue. Cost would also be a factor for pixel detectors at larger radii.

Further improvement of these detection systems can be done in terms of higher granularity and reduced material budget if, for example, the sensor and the front end readout are implemented on a single silicon substrate. This approach led to the development of CMOS Monolithic Active Pixel Sensors (MAPS). A schematic design of MAPS

2. MONOLITHIC ACTIVE PIXEL SENSORS FOR ALICE UPGRADE

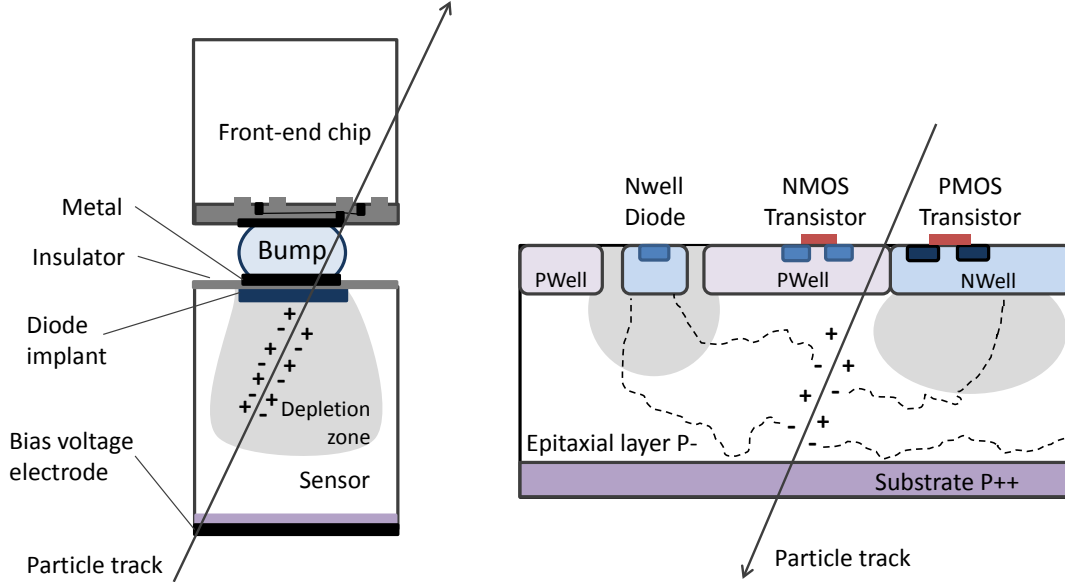


Figure 2.2: Left: Hybrid pixel. The sensor and the front-end chip are two separate components attached by a bump bond. Right: Monolithic pixel. The sensor and the front-end are developed on the same silicon substrate.

is shown in Fig.2.2 right, to compare this basic difference with the hybrid pixels. Extensive research and development in the last decade on MAPS made it an option for future vertexing and tracking silicon detectors. There are limitations of MAPS with respect to radiation hardness and readout speed due to which they are still not suitable for the LHC experiments like ATLAS, CMS and LHCb. But they can be a very good option in ultra-relativistic heavy ion experiments like ALICE where the radiation tolerance and readout requirements are less stringent. The ULTIMATE sensor [21] developed for the STAR Heavy Flavor Tracker (HFT) at RHIC was the first application of MAPS in a heavy-ion experiment. However, this sensor developed with AMS 0.35 μm technology does not satisfy the requirements of ALICE ITS upgrade, specially in terms of radiation hardness and readout time. These limitations could be overcome by the 0.18 μm technology provided by TowerJazz which is the technology selected for the ALICE ITS upgrade.

2.2.1 Detector Technology

The 0.18 μm technology provided by TowerJazz offers certain features which makes it suitable for the ALICE ITS upgrade. The 0.18 μm feature size and 4 nm (or less) gate oxide thickness would expectedly make the process more effective against the total ionising dose compared to the 0.35 μm technology used in the STAR HFT. Also, the following features offered by this process would result in improved sensor characteristics:

- The process allows for a nominal thickness of the epitaxial layer of 18 μm . This would contribute to the reduction of material budget, an essential requirement for ALICE ITS upgrade.
- Epitaxial layers with resistivity from 1 $\text{K}\Omega\text{cm}$ to 6 $\text{K}\Omega\text{cm}$ could be developed. This translates into bigger depletion area in the epitaxial layer which in turn would improve the signal to noise ratio of the sensor.
- The technology allows for 6 metal lines. This, in addition to the small feature size enables implementation of high density and low power digital circuits. This would reduce the area of the digital circuitry located at the periphery of the pixel matrix and would thus reduce the insensitive area of the pixel chip.
- The technology provides access to a stitching technology allowing the production of sensors with dimensions exceeding those of a reticle and enables the manufacturing of die sizes up to a single die per 200 mm diameter wafer. As a result, insensitive gaps between neighbouring chips could be removed.
- One of the most important features offered by this technology is the availability of a deep p-well option in the CMOS process. This would significantly enhance the sensor functionality, as explained in detail in the next section.

2.2.2 Principle of Operation of MAPS

2.2.2.1 MAPS in a standard CMOS process

The main components of MAPS in a standard CMOS process are shown in the left panel of Fig.2.3.

2. MONOLITHIC ACTIVE PIXEL SENSORS FOR ALICE UPGRADE

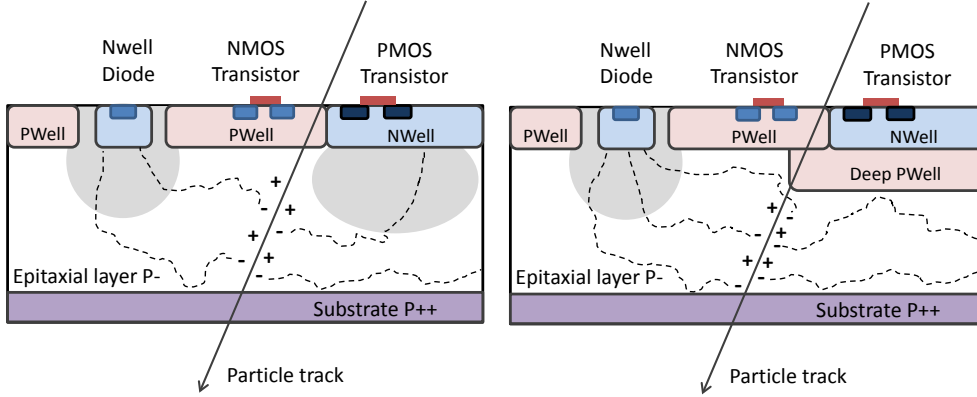


Figure 2.3: Left: Schematic cross section of MAPS in a standard CMOS process. Right: Schematic cross section of MAPS in the TowerJazz 0.18 μm technology with the deep p-well feature.

- Substrate: It is the lowest layer made of highly doped (p type), crystalline silicon with low resistivity. It provides mechanical stability and hosts all other structures.
- Epitaxial layer: The epitaxial layer is grown on top of the substrate. This layer is lightly doped (p type) and forms the active volume of the detector where charge carriers are generated by the impinging particles. The active devices are embedded in this layer.
- Well implantations: They serve as a bulk for the Field Effect Transistors. N-well and p-well implantations are used to integrate PMOS and NMOS transistors respectively.
- Diffusion implantations: They form the source and drain of the transistors. They have higher doping than the wells in which they are embedded into. P-type and N-type implantations are done for PMOS and NMOS respectively.
- Collection diode: The diode collects the charge generated in the epitaxial layer. The depletion region is formed at the junction between the diode n-well and the p-epitaxial layer.
- Metal lines: They connect the different silicon structures. They are generally made of aluminum or copper and embedded into silicon oxide, which serves as an insulator.

2.2.2.2 Detection principle in MAPS

The detection principle in MAPS is based on charge collection by diffusion. The different doping concentrations in different layers of MAPS facilitates the diffusion process. The charge carriers (electron-hole pairs) are generated in the epitaxial layer by the impinging particles. The electrons generated are deflected by the substrate due to a potential barrier formed between the lightly doped p-type epitaxial layer and the heavily doped p-type substrate. Similarly, a potential barrier exists between the lightly doped epitaxial layer and the heavily doped p-wells of the NMOS transistors. This results in the containment of the majority of the electrons within the epitaxial layer which diffuse randomly in the epitaxial layer and are guided towards the n-well of the collection diode. Diffusing electrons in the electric field due to the reverse biased diode near the n-well of the sensing diode are then collected as a signal.

As far as the charge collection mechanism in MAPS is concerned, the presence of the n-well of the PMOS transistor in a standard CMOS process poses a significant problem (Fig.2.3, left panel). This n-well which is at a positive potential, could also collect the diffusing electrons and thus compete with the collection diode. This would result in the reduction of signal charge collected and hence contribute to a reduction of the charge collection efficiency.

The TowerJazz 0.18 μm technology offers a deep p-well option to overcome this problem as illustrated in the right panel of Fig.2.3. A deep p-well (heavily doped) is implanted in the region where the front-end electronics is foreseen. The n-wells that accommodate the PMOS transistors are fabricated on top of the deep p-well. The potential barrier between the deep p-well and the epitaxial layer deflects the diffusing electrons and are thus collected by the sensing diode alone. The size of the deep p-well can be tailored to optimize the charge collection efficiency and the signal-to-noise ratio and full CMOS front-end electronics can be implemented in the pixel. The detailed fabrication process of the deep p-well implantation is described elsewhere [22].

2.2.2.3 Front end readout

The most common in-pixel architectures are the so called 2T and 3T architectures, as shown in Fig.2.4. The architecture consists of a source follower transistor (M1) connected to the sensing diode. The charge collected by the sensing diode results in a

2. MONOLITHIC ACTIVE PIXEL SENSORS FOR ALICE UPGRADE

voltage drop at the gate of the source follower transistor which acts as a voltage buffer. The output of the buffer is connected to a second transistor (M2) which acts as a switch. This switch enables the read out of the buffer output at the end of column circuitry.

The sensing diode suffers a continuous voltage decay due to leakage current since the parasitic capacitance of the collection diode discharges continuously. This is compensated at regular intervals by connecting the diode to a reference potential using a reset transistor (M3), in case of a 3T structure. The reset transistor is replaced by a forward biased diode in a 2T structure (self-bias).

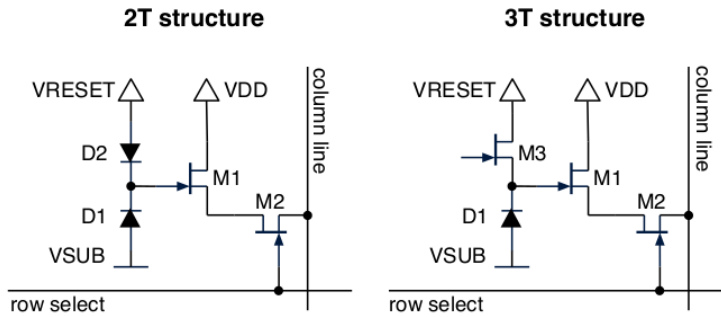


Figure 2.4: Pixel architectures: 2T structure (left) and 3T structure (right).

Such an arrangement is often readout by a method called the rolling shutter readout: rows are read out one after the other by selecting the row switches (M2) and in case of 3T - applying the reset pulse shortly after. In this way each row integrates the signal between two consecutive passings of the row select signal (the shutter) and each row is essentially continuously sensitive. The biggest advantage of this architecture is the very small number of transistors needed within each pixel and can be implemented with transistors of the same polarity, which is a requirement in standard CMOS imaging processes.

2.2.3 MAPS prototypes for the ALICE ITS upgrade

Several MAPS prototypes are being developed for the ALICE ITS upgrade. These prototypes address design features of different building blocks of the pixel sensor. Prototypes corresponding to different design architectures are being investigated which exploit the wide range of features provided by the TowerJazz 0.18 μm technology. The

2.2 Monolithic Active Pixel Sensors for ALICE

next chapter deals with some of these prototypes elaborating the characterization procedures and results. These studies would validate the different building blocks of the pixel sensor and lead to the selection of the final architecture for the upgrade.

2. MONOLITHIC ACTIVE PIXEL SENSORS FOR ALICE UPGRADE

3

Characterisation of Monolithic Active Pixel Sensors

Contents

4.1	Introduction	71
4.2	Experimental conditions (ALICE Run 3) for simulation studies	72
4.3	Detector specification	75
4.4	Simulation tools	80
4.5	Detector performance studies	81

3.1 Observables and Methods

3.1.1 Correlated Double Sampling

The Correlated Double Sampling (CDS) is used to extract the signal from the data and to mitigate the effects of low frequency noise components. Two consecutive samples are taken between known intervals and the difference between those samples gives the signal. The following example with the 3T architecture, illustrated in Fig. 3.1, demonstrates CDS. First, the pixels are subjected to a reset. The reset transistor injects charge into the sensing diodes which are set to the reset voltage. Then the matrix is readout row by row in a rolling shutter mode. After the reading the last row, the readout starts from the first row. The entire matrix is readout twice, consecutively followed by a reset. The time to readout the entire matrix is the integration time, which is the time interval

3. CHARACTERISATION OF MONOLITHIC ACTIVE PIXEL SENSORS

between two consecutive readouts of a pixel. The difference between the two samples gives the signal integrated by the pixels during the integration time.

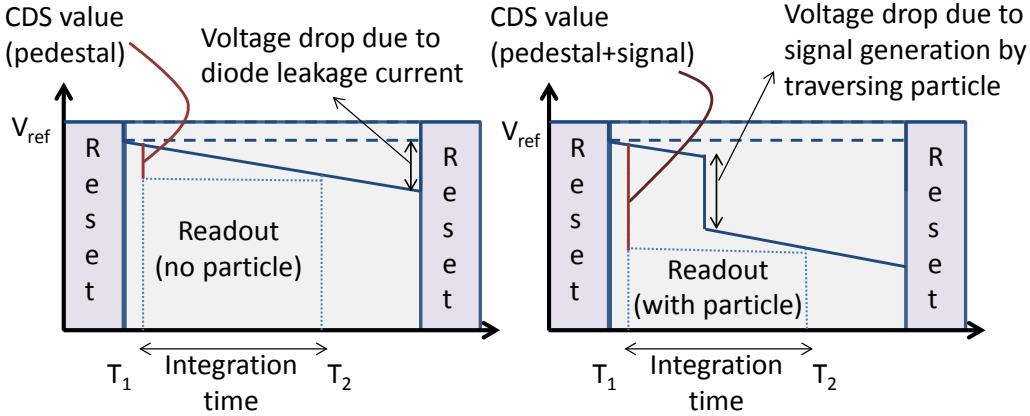


Figure 3.1: The Correlated Double Sampling.

3.1.2 Laboratory measurements with ^{55}Fe source

The purpose of the laboratory tests using a radioactive source is to measure the following sensor parameters:

- Equivalent Noise Charge (ENC)
- Charge Collection Efficiency (CCE)

The ENC of a sensor is expressed in terms of number of electrons. The analog data from the pixels are readout in ADC units. A calibration procedure is needed to quantify the ADC units in electrons to express the ENC. This is generally done using a radioactive source with a known spectrum. For this thesis, the calibration is done using a ^{55}Fe source for X-ray photons with $K_{\alpha} = 5.9 \text{ keV}$ and $K_{\beta} = 6.49 \text{ keV}$.

The procedure is explained by the following example using the matrix P7 of Mimos32Ter chip (explained in Section 3.2). The matrix consists of sixty four rows and sixteen columns.

First, a pedestal run without the source is performed. Each event contains the data from two consecutive frames. Each frame corresponds to the entire pixel matrix which is readout row by row. The difference between the two consecutive readings for each

event are taken (correlated double sampling). Then the average of the CDS value for each pixel over all events is mapped. This gives the pedestal value in ADC units for each pixel. In Fig.3.2, the top panels show the pedestal map and distribution for the pixel matrix. The standard deviation of the pedestal distribution for each pixel gives the noise value in ADC units for each pixel. The average value of the noise of all the pixels gives the noise of the entire matrix. The bottom panels Fig. 3.2 show the noise map and distribution for the same matrix. In this case, the noise of the P7 matrix is 1.04 ADC.

Next, a run with the ^{55}Fe source is performed. The CDS data is computed from the raw data. The pedestal value for each pixel (from the previous pedestal run) is subtracted from the CDS value of the corresponding pixel. Then, the pixel with the highest signal is searched. If the signal is above a certain threshold, then the pixel is defined as the seed pixel. In this case, the threshold value of each pixel is five times the noise value for that particular pixel. This procedure is repeated for all the events. The distribution of charge in the seed pixel over all events gives the ^{55}Fe spectrum. Fig.3.3 shows the ^{55}Fe spectrum for the Mimosas32Ter P7 matrix. The lowest possible ADC value is user defined by a hardware threshold of the readout system.

The different peaks in the ^{55}Fe spectrum can be explained as follows. The X-ray photons from the ^{55}Fe source generate electron-hole pairs in the epitaxial layer. The charge carriers are generated close to the interaction point (few microns). The electrons diffuse randomly in the epitaxial layer and are reflected from the substrate and the p-wells, which results in the movement of a part of these electrons into the neighboring pixels. Thus there is a charge spread and a cluster of charge is formed. In these events, only a part of the signal generated is collected by the seed pixel. This corresponds to the broad peak around 40 ADC counts in the Fig.3.3 which is the signal peak. When the photons interact at points very close to the depletion region of the sensing diode, the generated electrons are collected entirely by the sensing diode, resulting in a single-pixel cluster. In Fig.3.3, this is visible in the extreme right of the spectrum where there are two peaks at 85 and 92 ADC counts. In these events, the seed pixel collects the entire charge generated. The smaller peak around 92 ADC counts corresponds to $K_\beta = 6.49\text{ keV}$. The larger peak at around 85 ADC counts correspond to $K_\alpha = 5.9\text{ keV}$. This peak is used as the calibration peak and is used to convert the ADC counts to electrons.

3. CHARACTERISATION OF MONOLITHIC ACTIVE PIXEL SENSORS

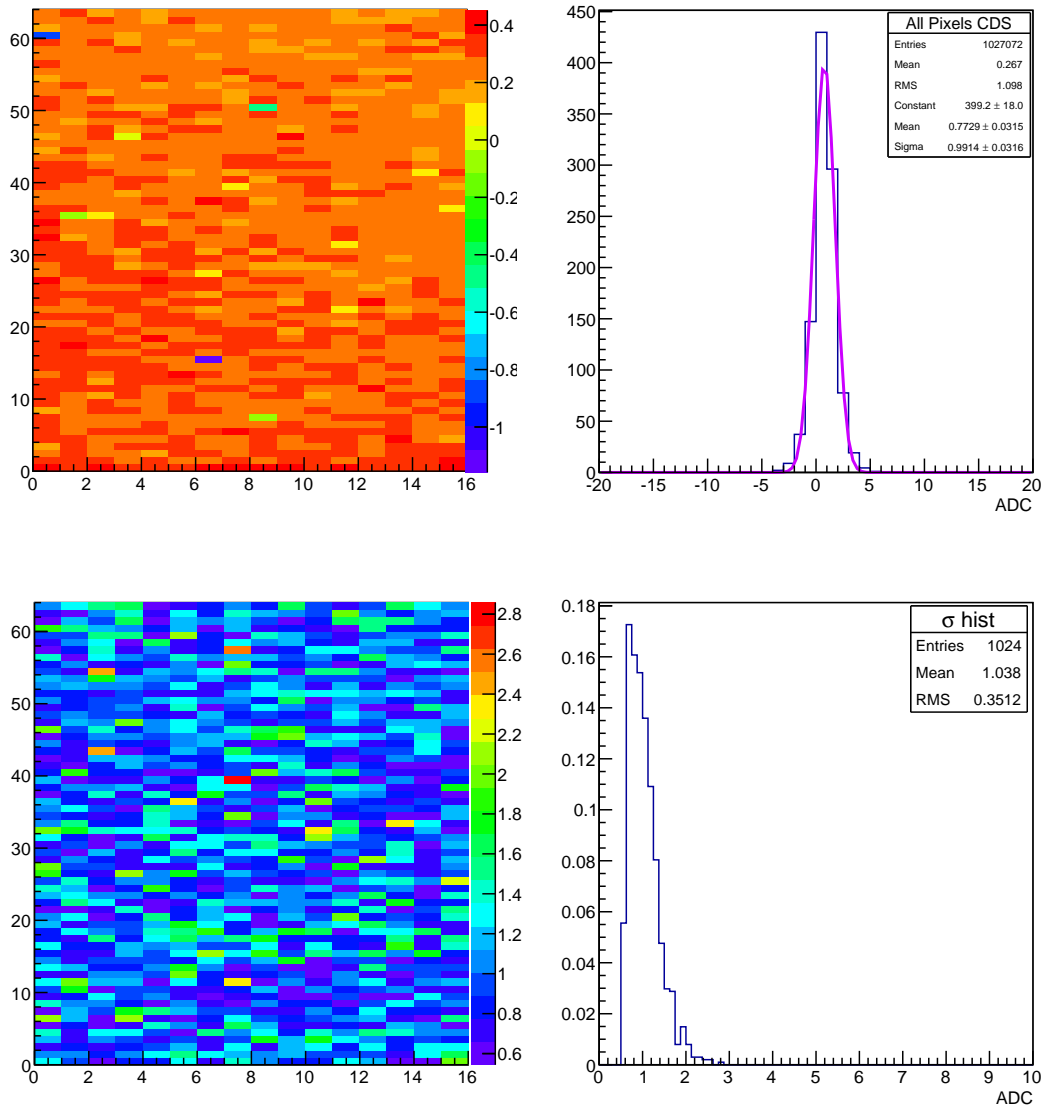


Figure 3.2: Top panels: Pedestal map (left) and distribution (right) of Mimosa32Ter P7 matrix. The matrix consists of sixty-four rows and sixteen columns. The readout is done row by row. The matrix is readout twice and then the difference between the two consecutive values for each pixel is calculated for each event and then averaged over all the events. This gives the pedestal for each pixel. Bottom panels: The noise map (left) and distribution (right) of the same matrix. The standard deviation of the pedestal distribution of the matrix gives the noise of the matrix.

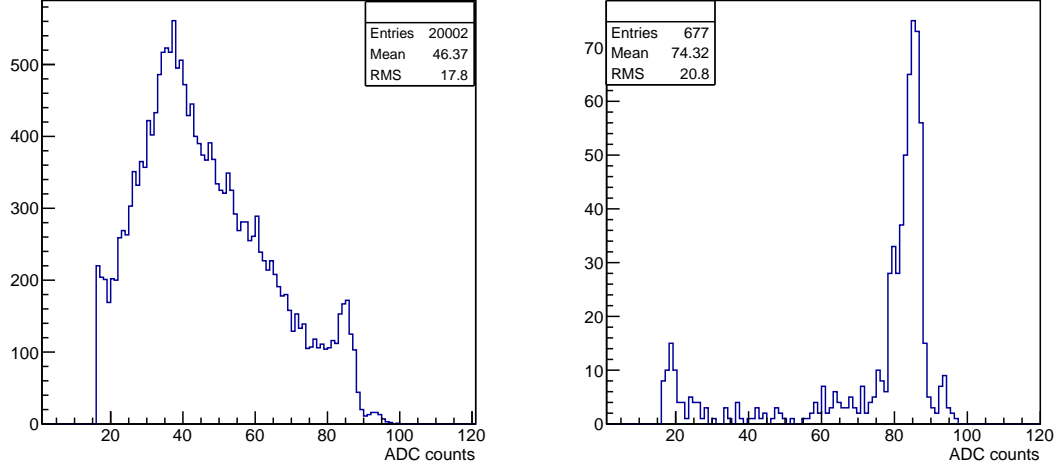


Figure 3.3: ^{55}Fe spectrum of Mimoso32Ter P7 matrix. The seed pixel is searched for each event in a source run. The pixel with the highest signal in the matrix for each event which satisfies a 5σ cut is the seed pixel for that event. The distribution of the seed pixel charge over all events give the ^{55}Fe spectrum.

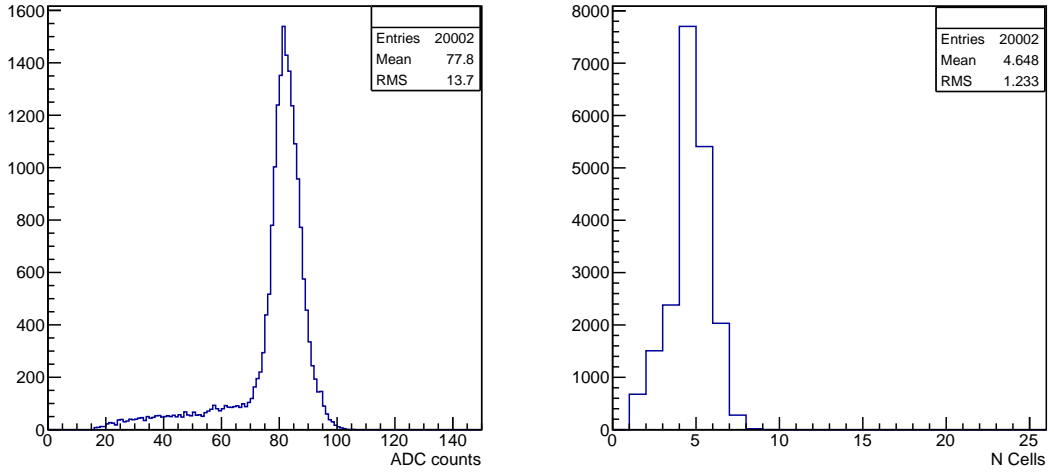


Figure 3.4: Cluster signal distribution and cluster multiplicity for Mimoso32Ter P7 matrix. CLuster pixels are searched in a 5×5 matrix around the seed. The pixels with a signal above 3σ are considered here. The sum of the signals in the cluster including the seed gives the cluster signal distribution.

3. CHARACTERISATION OF MONOLITHIC ACTIVE PIXEL SENSORS

The right panel of the Fig.3.3 shows the single-pixel cluster distribution, extracted from the seed spectrum.

The search for the seed pixel excludes the borders of the matrix. The borders consist of first two and last two rows and columns of the matrix. This is done to accommodate potential candidates for a cluster of neighboring pixels around a seed. After the seed pixel is found, a matrix of 5x5 pixels is considered around the seed pixel to search for clusters. A neighboring pixel of the seed having a signal above a certain threshold is considered as a cluster pixel. In this case, the threshold selected for a pixel is three times the noise for that pixel. Once a cluster is identified, the total charge in the cluster (including the seed) is computed for all events. In Fig.3.4, the left panel shows the cluster signal distribution over all events. The cluster peak is around 83 ADC counts. The right panel of the Fig.3.4 shows the cluster multiplicity. The cluster signal distribution is also computed without applying any cut on the neighboring pixels of the seed in the 5x5 matrix around the seed.

The steps mentioned above provide the required information to calculate the ENC and CCE of the sensor as explained in the following:

- Equivalent Noise Charge:

3.6 eV is necessary to generate 1 e-h pair in silicon. Hence, the Fe peak of 5.9 KeV (calibration peak) corresponds to the generation of 1640 e-h pairs. In the Fig.3.3, the Fe peak corresponds to 85 ADC counts, which are equivalent to 1640 e/h pairs. Hence,

$$1 \text{ ADC} = 1640/85 = 19.3 \text{ electrons (calibration factor).}$$

$$\text{Noise (from previous pedestal run)} = 1.04 \text{ ADC} = 1.04 \times 19.3 = 20.19 \text{ electrons (ENC).}$$

- Charge Collection Efficiency:

The CCE is given by the ratio of the cluster signal peak to the single-pixel cluster peak.

$$\begin{aligned} \text{CCE} &= \text{Cluster peak} / \text{Single-pixel cluster peak} \\ &= 83/85 = 97.6\% \end{aligned}$$

Hence the sensor parameters for the Mimoso32Ter P7 matrix are:

$$\text{ENC: } 20 \text{ electrons} \quad \text{CCE: } 98\%$$

3.1.3 Measurements with minimum ionizing particles

The sensors performance is also measured with minimum ionizing particles. The particles passing through the epitaxial layer generate electron-hole pairs along their trajectory. The electrons then move randomly by diffusion and are then collected by the collection diode. The sensor parameters which are measured are:

- Signal to noise ratio (SNR)
- Detection Efficiency

The data acquisition and data treatment procedure for the beam tests are similar to that of the ^{55}Fe source. The noise of the matrix is found from the pedestal run. Then a beam run is performed and the data is analyzed to find the seed pixels and the clusters. The seed signal distribution for MIPs gives a Landau-like distribution. The cluster signal distribution is also similar. The seed signal can then be divided by the noise of the corresponding seed pixel to give the SNR for that pixel. The SNR shows a Landau-like distribution over all the events and the peak value of the distribution gives the SNR of the pixel matrix.

The detection efficiency is related to the SNR. If a sensor have a low SNR, it may not be possible to detect a signal generated by MIPs over the noise and hence this would translate into a low detection efficiency. The detection efficiency is measured with the use of a beam telescope. The sensor under test is placed between the planes of a telescope. Tracks are reconstructed from the hits in the planes of the telescope. Then hits are searched in the sensor under test for the corresponding tracks reconstructed in the telescope planes. The ratio between the hits detected in the sensor to the number of reconstructed tracks in the telescope planes gives the detection efficiency of the sensor.

3.1.4 Measurements for irradiated chips

The measurements described for the sensor with ^{55}Fe source and minimum ionizing particles are performed both for non irradiated and irradiated sensors. The sensors are irradiated with neutrons and the effects of Non Ionising Energy Loss (NIEL) are studied. The irradiation would cause bulk defects on silicon and would create recombination points in the epitaxial layer which would reduce the number of electrons which could be collected. This could result in the degradation of the sensor performance.

3. CHARACTERISATION OF MONOLITHIC ACTIVE PIXEL SENSORS

3.2 MIMOSA32 and MIMOSA32Ter

MIMOSA32 was the first prototype for ALICE ITS Upgrade which was designed using the TowerJazz 0.18 μm technology. As discussed in Chapter 2, one of the most attractive options provided by this technology is the possibility to implement a deep p-well under a competing n-well. Traditionally only NMOS transistors were used for MAPS, to avoid the effect of an n-well (housing a PMOS transistor) which competes with the n-well of the collection diode in terms of charge collection. A deep p-well under the n-well is designed to prevent this competing charge collection and facilitate the implementation of full CMOS circuit in MAPS design. This has implications in terms of implementing sophisticated signal processing circuits inside the pixel using both PMOS and NMOS transistors.

MIMOSA32 is an exploratory chip consisting of prototype pixel structures. The properties of these structures were studied, in particular their charge collection properties, to validate the TowerJazz 0.18 μm technology for the ALICE ITS Upgrade programme. MIMOSA32 includes traditional MAPS structures with NMOS transistors and also structures with a deep p-well implementation. The pixel circuits with the deep p-well implementation does not include PMOS transistors but the motivation is to study the effects of this deep p-well, if its presence produces any effects and if it disturbs the performance. The tests also include irradiated chips to study the technology's radiation tolerance to Non Ionising Energy loss (NIEL).

MIMOSA32 was submitted for fabrication in October 2011 and was received from the foundry in April 2012. The top panel of Fig.3.5 shows the overview of the MIMOSA32 chip. There are several blocks implemented in the chip for studying different aspects of pixel sensors like discriminators, steering circuits etc. The block named Diodes & Ampli consists of thirty-two pixel matrices with different architectures. There are twenty two matrices where the sensing diode is connected with a source follower (both 3T and 2T: Section 2.2.2.3). The remaining ten matrices contain an additional preamplification chain.

The bottom panel of Fig. 3.5 shows the overview of MIMOSA32Ter. It was submitted for fabrication in July 2012 and received from the foundry in October 2012. It retains some matrices from MIMOSA32 as reference and include other matrices with different input source follower transistor sizes. The pixel circuits implement NMOS

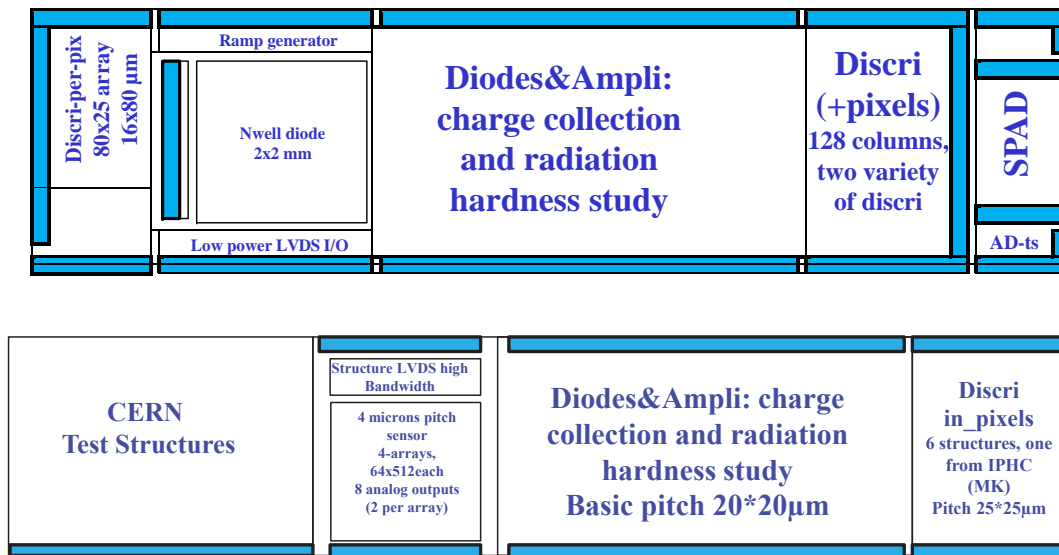


Figure 3.5: Overview of MIMOSA32 (top panel) and MIMOSA32Ter (bottom panel) chips. There are several components like discriminators, steering circuits etc. to study different parts of a pixel sensor. The central part named Diodes and Ampli area consists of thirty two pixel matrices with different architectures.

transistors and some structures implement deep p-well of different sizes. Like in MIMOSA32, PMOS transistors are not implemented. Different sizes of the deep p-well are implemented. Optimizing the acceptable area covered by the deep p-well would help to define the maximum area that is possible to allocate for the implementation of the PMOS transistors in the pixel in the future prototypes. The size of the source follower input transistor affects the input capacitance of the circuit which in turn affect the charge collection properties. There are some structures with the input transistors in an Enclosed Transistor Layout (ELT). In such a configuration, the transistor drain is enclosed by the poly-silicon gate. The transistor source region is placed outside and surrounded with a guard-ring, insulating the transistor [23]. ELT is implemented to improve the radiation tolerance to total ionisation dose (TID).

MIMOSA32Ter consists of fifteen source follower structures (including 2T and 3T structures) and fifteen structures with an additional preamplification chain. The pixel pitch in these matrices is $20\ \mu\text{m}$. There are two elongated pixel matrices of $20\ \mu\text{m} \times 33\ \mu\text{m}$.

This thesis studies the 3T pixels of MIMOSA32 and MIMOSA32Ter as mentioned in Table 3.1.

3. CHARACTERISATION OF MONOLITHIC ACTIVE PIXEL SENSORS

Table 3.1: Pixel matrices having a source follower 3T architecture in MIMOSA32 and MIMOSA32Ter. The collection diode in all the matrices is octagonal in shape covering an area of $11 \mu\text{m}^2$

- . All the matrices use NMOS transistors. Some matrices have a deep p-well (without PMOS transistors), along with the traditional MAPS circuit, to study its effects on the sensor performance.

Chip	Matrix name	Characteristic
MIMOSA32	P2	Enclosed Layout Transistor (ELT)
	P6	Non ELT
	P8	Deep Pwell small
	P9	Deep Pwell medium
	P10	Deep Pwell large
MIMOSA32Ter	P2	Non ELT (M32 P6)
	P3	Non ELT, small SF transistor, Deep Pwell ($33 \mu\text{m}^2$)
	P4	ELT, small SF transistor, Deep Pwell ($33 \mu\text{m}^2$)
	P5	Non ELT, smaller SF transistor
	P6	Non ELT, small SF transistor
	P7	Non ELT, small SF transistor, Deep Pwell, $6 \mu\text{m}$ spacing from the diode
	P8	Non ELT, small SF transistor, Deep Pwell, $10 \mu\text{m}$ spacing from the diode

The matrices can be readout one at a time. Each matrix has sixty four rows and sixteen columns. The readout is done row by row in a rolling shutter mode. The columns are readout in parallel. The readout sequence consists of a reset phase, done row by row and followed by reading out the matrix. After the reading the last row, the readout sequence starts again from the first row. Thus the matrix is readout two times consecutively. The integration time is the readout time for one matrix: $32\ \mu\text{s}$ with a 2 MHz clock. The data is then subjected to Correlated Double Sampling (CDS).

3.2.1 Test set up for MIMOSA32 and MIMOSA32Ter

A readout system was developed in Cagliari for the MIMOSA32 and MIMOSA32Ter chips. The readout system consists of a principal readout card (ZRC), an auxiliary card and a web user interface. Fig.3.6 shows a schematic view of the test readout system. The ZRC (ZDC Readout Card) is presently being used by the ALICE Zero Degree Calorimeters [24]. The ZRC is a general purpose card with options of attaching different application specific mezzanine cards (Fig. 3.7, left panel). The ZRC provides an interface to the ALICE DATE (ALICE Data Acquisition and Test Environment) via DDL (Detector Data Link) interface or Ethernet. It also provides an interface to the ALICE trigger system.

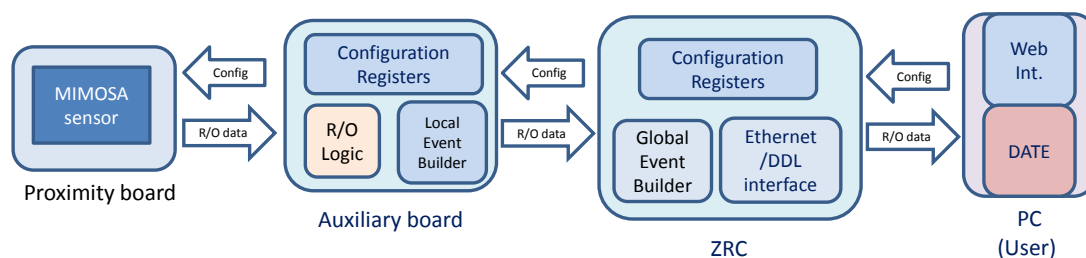


Figure 3.6: Readout system schematic for MIMOSA32 and MIMOSA32Ter. The main components include a principal readout card (ZRC), an auxiliary card and a web user interface.

For the readout of MIMOSA pixel sensors, the ZRC is equipped with a mezzanine board which can be interfaced with up to four various application specific auxiliary cards (Fig. 3.7, right panel), which are the interface between the ZRC and the proximity (or carrier) board on which the pixel sensor is housed. The ZRC is also equipped with

3. CHARACTERISATION OF MONOLITHIC ACTIVE PIXEL SENSORS

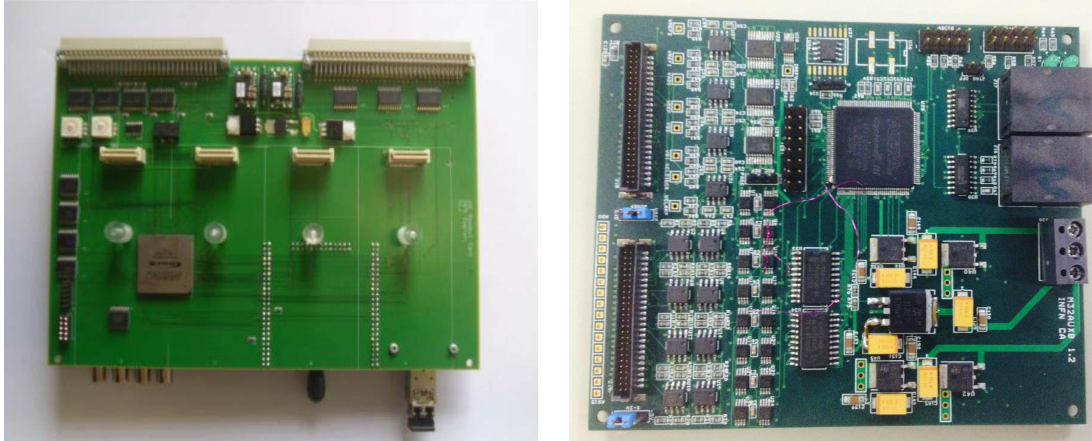


Figure 3.7: Left: The principal readout card for the MIMOSA32 and MIMOSA32Ter, based on the readout card (ZRC) used currently in ALICE Zero Degree Calorimeters. Right: The auxiliary card which interfaces the ZRC to the sensor carrier board.

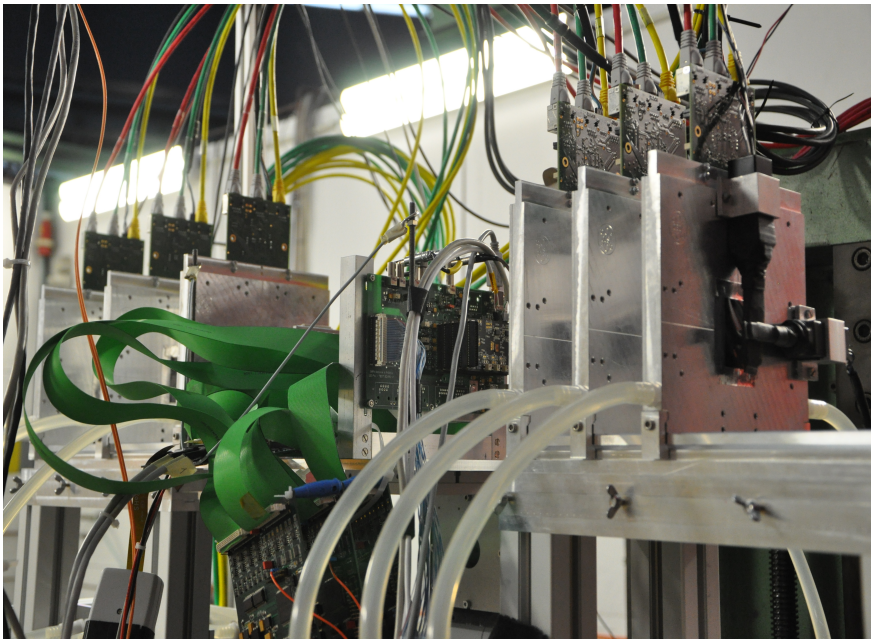


Figure 3.8: Setup at DESY for beam tests for MIMOSA32 and Explorer sensors. Explorer results are discussed later in this chapter.

a NIM-LVDS I/O mezzanine card to interface with the ALICE trigger system or to receive and process external trigger signals.

The user can configure the readout system through a web interface which communi-

cates with the Ethernet interface on the ZRC. The configuration data are sent from the ZRC to the auxiliary card and also to the pixel sensor. After initializing the readout, the data coming from the pixel sensor are received by the auxiliary card and then sent to the ZRC card, which performs an event building by combining data from the sensors, attaches a common data header and then sends the event to ALICE DATE. The system can be configured to work with a trigger or in a continuous mode.

For beam tests, a set of three MIMOSA planes were used to form a telescope. These were readout by a single ZRC through a set of three auxiliary cards. Fig.3.8 shows a setup for beam tests at DESY.

3.2.2 Characterization of MIMOSA32 and MIMOSA32Ter

The MIMOSA32 and MIMOSA32Ter matrices with 3T structures were tested in the laboratory with ^{55}Fe source. They were also tested with 4 GeV positron beams at DESY in March and June 2013. The results show the performance of a reference matrix followed by the performance comparison with the other matrices of the respective chip.

3.2.2.1 MIMOSA32

In Fig.3.9, the top panel shows the pedestal map (left) and distribution (right) of the MIMOSA32 P8 matrix having a full deep-Pwell. The bottom panel shows the noise map (left) and distribution (right). The noise of the matrix ≈ 2.06 ADC units. The Equivalent Noise Charge (ENC) can be determined from the Fig. 3.10 which shows the results with the ^{55}Fe source. The cut used on the seed pixel is five times the mean noise of the matrix (5σ) and that of the neighbours in a cluster is three times the mean noise of the matrix (3σ). The top panel shows the seed spectrum with ^{55}Fe source (left) and the single pixel cluster distribution (right). The single pixel cluster distribution, derived from the seed spectrum, gives the distribution of the charge collected by a single pixel, where the ^{55}Fe peaks can be identified. The ^{55}Fe peak (5.49 KeV) ≈ 166 ADC counts, which gives the calibration factor: 1 ADC ≈ 9.88 electrons. Thus the ENC of the P8 matrix is 20.36 electrons. The bottom panel of Fig. 3.10 shows the cluster signal distribution (left) and the cluster multiplicity (right). The ratio of the cluster signal peak to the ^{55}Fe peak (5.49 keV) gives the charge collection efficiency (CCE), which in this case is 97.06%.

3. CHARACTERISATION OF MONOLITHIC ACTIVE PIXEL SENSORS

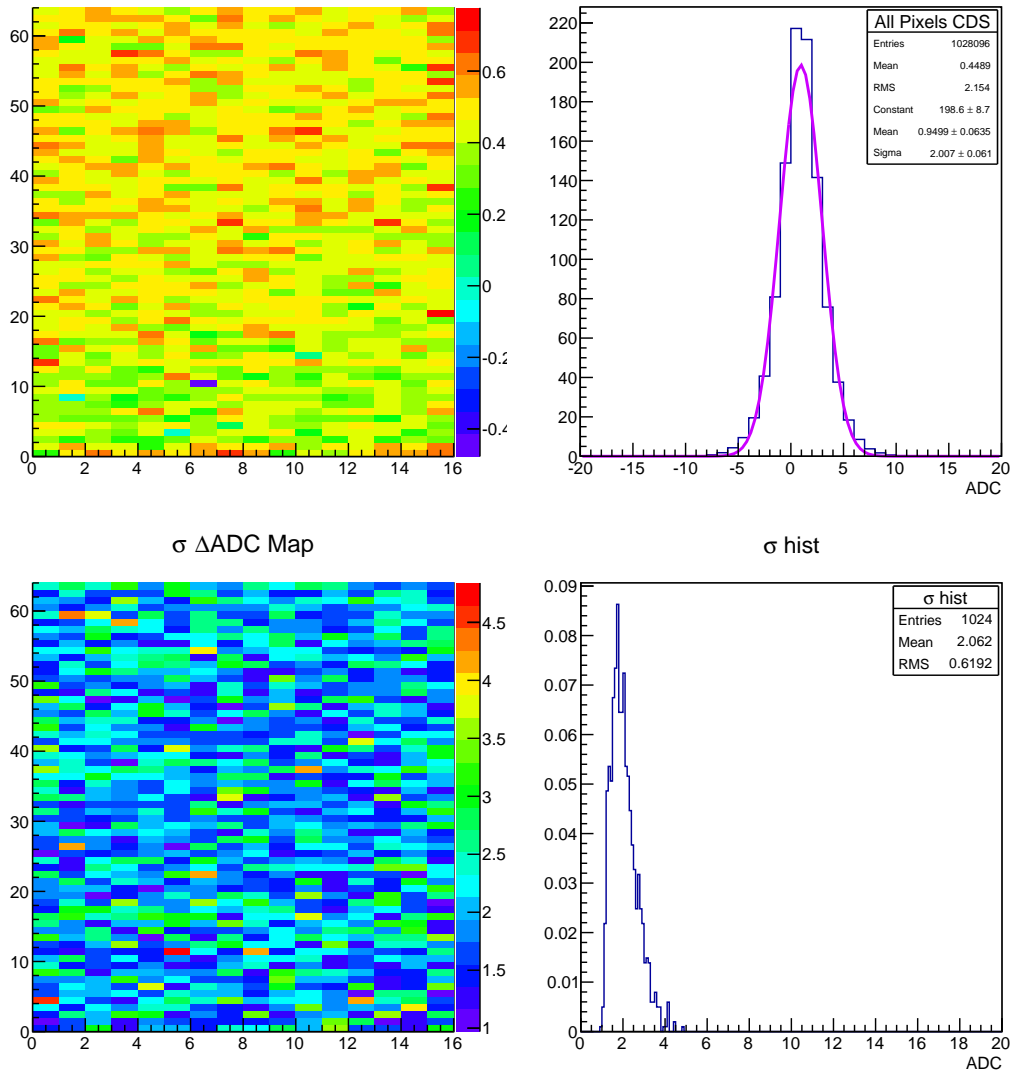


Figure 3.9: Top panels: Pedestal map (left) and distribution (right) of MIMOSA32 P8 matrix. The matrix consists of sixty-four rows and sixteen columns. Bottom panels: The noise map (left) and distribution (right) of the same matrix. The standard deviation of the pedestal distribution of the matrix gives the noise of the matrix.

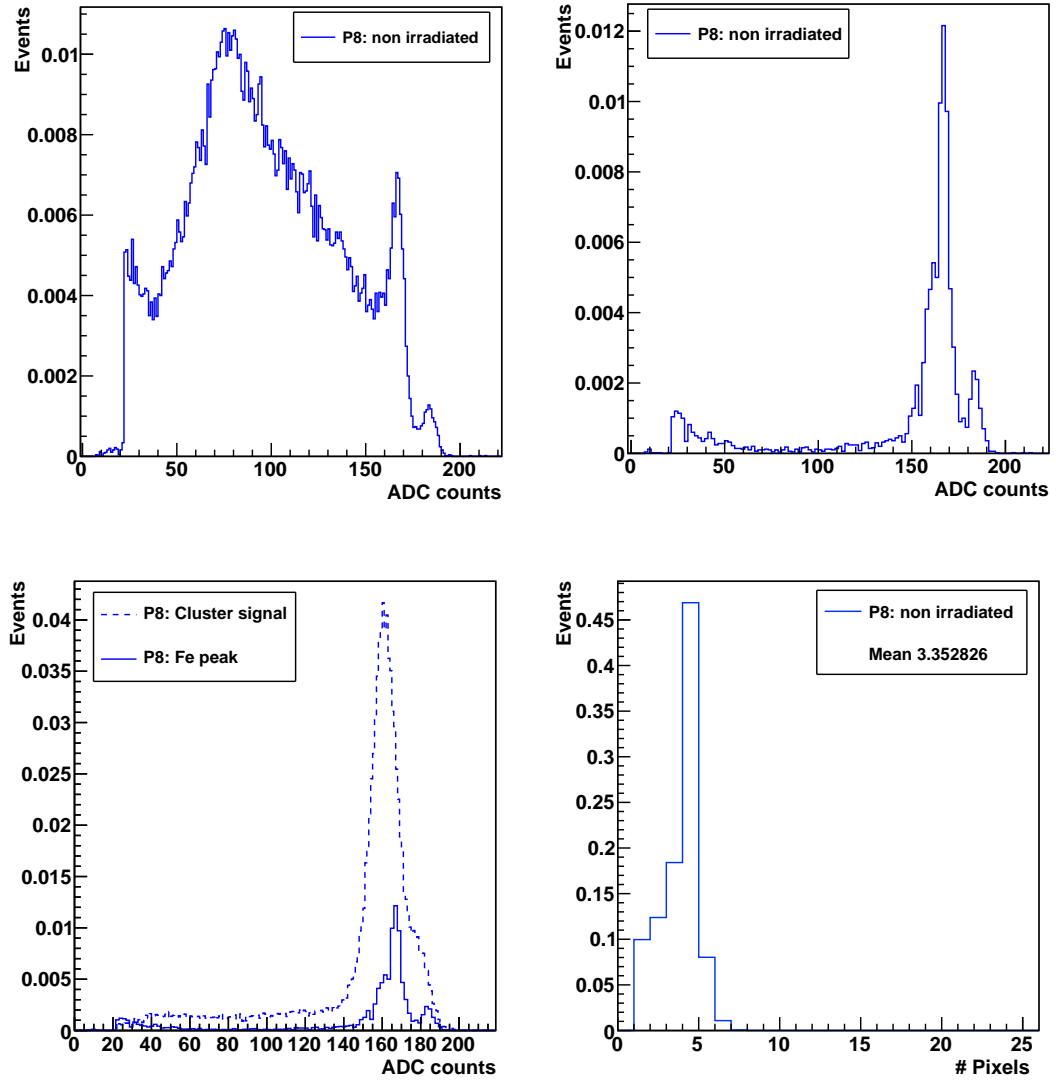


Figure 3.10: Top panels: Seed signal spectrum (left) and single pixel cluster signal distribution (right) for MIMOSA32 P8 matrix. Bottom panels: Cluster signal distribution (left) and cluster multiplicity (right) of the same matrix.

3. CHARACTERISATION OF MONOLITHIC ACTIVE PIXEL SENSORS

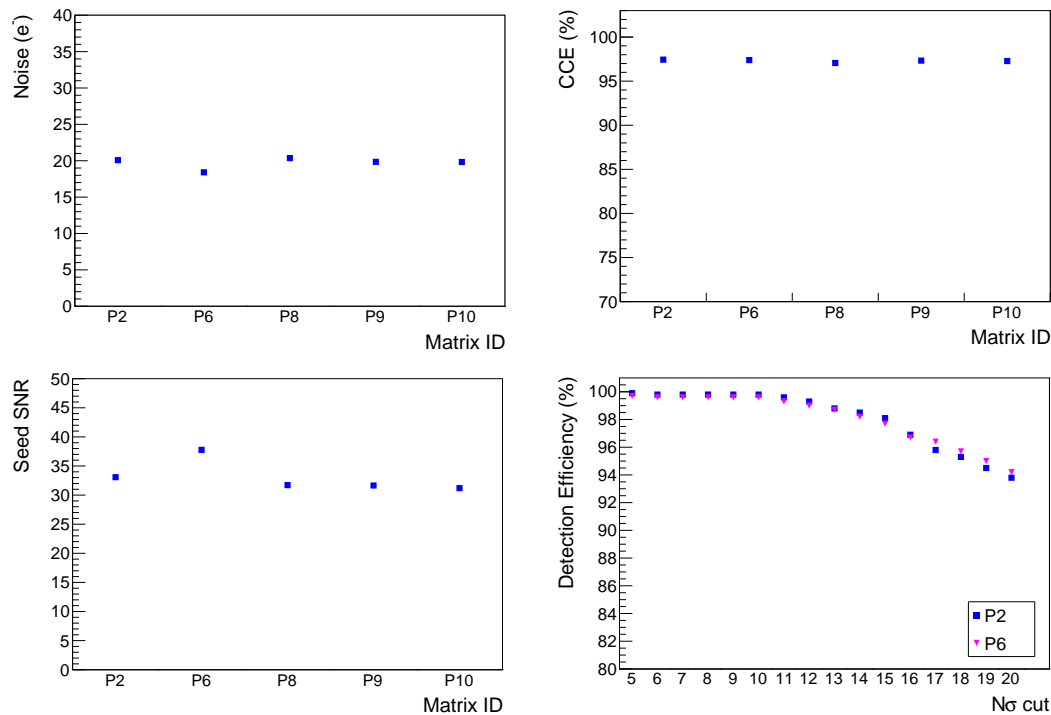


Figure 3.11: Top panels: ENC (left) and CCE (right) performances of the different matrices of MIMOSA32. Bottom panels: The seed signal to noise ratio is shown for the same matrices (left). The detection efficiency of P2 and P6 matrices is also shown (right).

Fig.3.11 shows the comparison of the MIMOSA32 matrices which are mentioned in Table.3.1. The P6 matrix consists of square pixels of $20\ \mu\text{m}$ pitch, based on a 3T structure. The P2 matrix is similar to P6, but has an Enclosed Layout Transistor (ELT) structure. The matrices P8, P9 and P10 have a deep p-well implemented along with a traditional MAPS design with NMOS transistors. All the matrices have an octagonal collection electrode of area $11\ \mu\text{m}^2$.

The top left panel of Fig.3.11 show the comparison of the ENC. All the matrices have comparable ENCs around 20 electrons. The CCE of all the matrices are also similar around 98%. These matrices were also tested with 4 GeV positron beams in March 2013. The seed SNR of the matrices, determined from the beam tests are compared in the bottom panel of Fig.3.11. All the matrices have a seed SNR above 30.

Fig.3.11 shows also the detection efficiency of the P2 and P6 structures. A custom telescope using three planes of MIMOSA32 sensors was used with the middle plane as the

device under test. Only events with a single hit in the first plane are considered. These hits are then associated with the hits in the last plane and tracks are reconstructed. A cut of 10σ and 3σ are considered for the seed pixel and the neighboring pixels of the seed in the cluster. Hits are then searched in the middle plane corresponding to these tracks, in a zone of 5×5 pixels around the reconstructed track. The ratio of the number of these hits found in the middle plane to the number of reconstructed tracks gives the detection efficiency. The detection efficiency for both the structures were above 98%.

All the five structures tested have satisfactory charge collection properties, which shows that the technology is promising for further optimization of the pixel properties in future prototypes. The results show that the presence of a deep p-well in the pixels (which have a traditional design with NMOS transistors) does not affect the performance of the pixel and maintain similar charge collection properties like the pixels without the deep p-well. Thus the deep p-well in a pixel does not introduce any degradation in performance. This validates the use of the deep p-well option in future prototypes for implementing full CMOS in-pixel circuits thereby allowing sophisticated in-pixel signal processing circuits.

3.2.2.2 Tests with irradiated MIMOSA32

To test the effects of NIEL on the performance of MIMOSA32. Before being bonded on the test boards the chips were subjected to three levels of irradiation: $0.66 \times 10^{13} n_{eq}/cm^2$, $1.33 \times 10^{13} n_{eq}/cm^2$ and $2.66 \times 10^{13} n_{eq}/cm^2$ from the TRIGA MarkII Reactor at JSI in Ljubljana.

Fig.3.12 shows the ENC comparison between the matrices P2, P6, P8, P9 and P10 with different radiation fluences (left). The right panel shows the CCE comparison. The structures have similar performance at different radiation fluences. This shows that the presence of deep p-well does not affect the pixel performance even after irradiation, further validating its use in future prototypes.

3. CHARACTERISATION OF MONOLITHIC ACTIVE PIXEL SENSORS

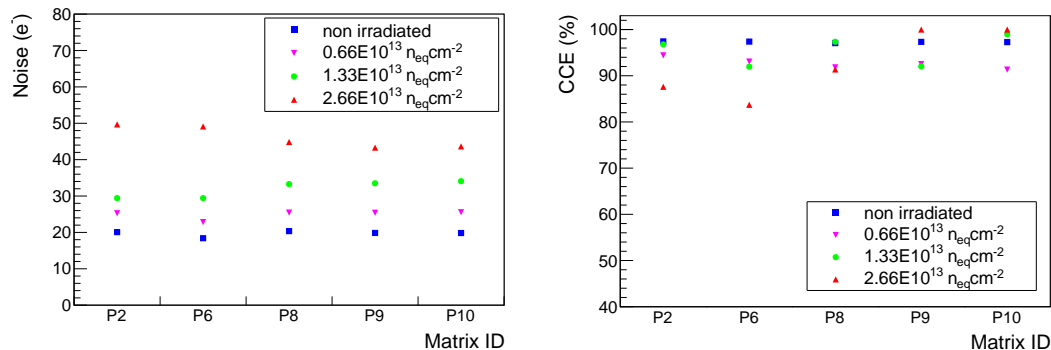


Figure 3.12: ENC (left) and CCE (right) comparison between non irradiated and irradiated matrices of MIMOSA32.

3.2.2.3 MIMOSA32Ter

In Fig.3.13, the top panel shows the pedestal map (left) and distribution (right) of the MIMOSA32Ter P7 matrix having a deep p-well. The bottom panel shows the noise map (left) and distribution (right). The ENC and CCE are derived from the results with ⁵⁵Fe source as shown in Fig.3.14, where the top panel shows the seed spectrum with ⁵⁵Fe source (left) and the single pixel cluster distribution (right). The bottom panel shows the cluster signal distribution (left) and the cluster multiplicity (right). The cut used on the seed pixel is five times the mean noise of the matrix (5σ) and that of the neighbours in a cluster is three times the mean noise of the matrix (3σ). The Equivalent Noise Charge (ENC) ≈ 20 electrons and the Charge Collection Efficiency (CCE) $\approx 97\%$.

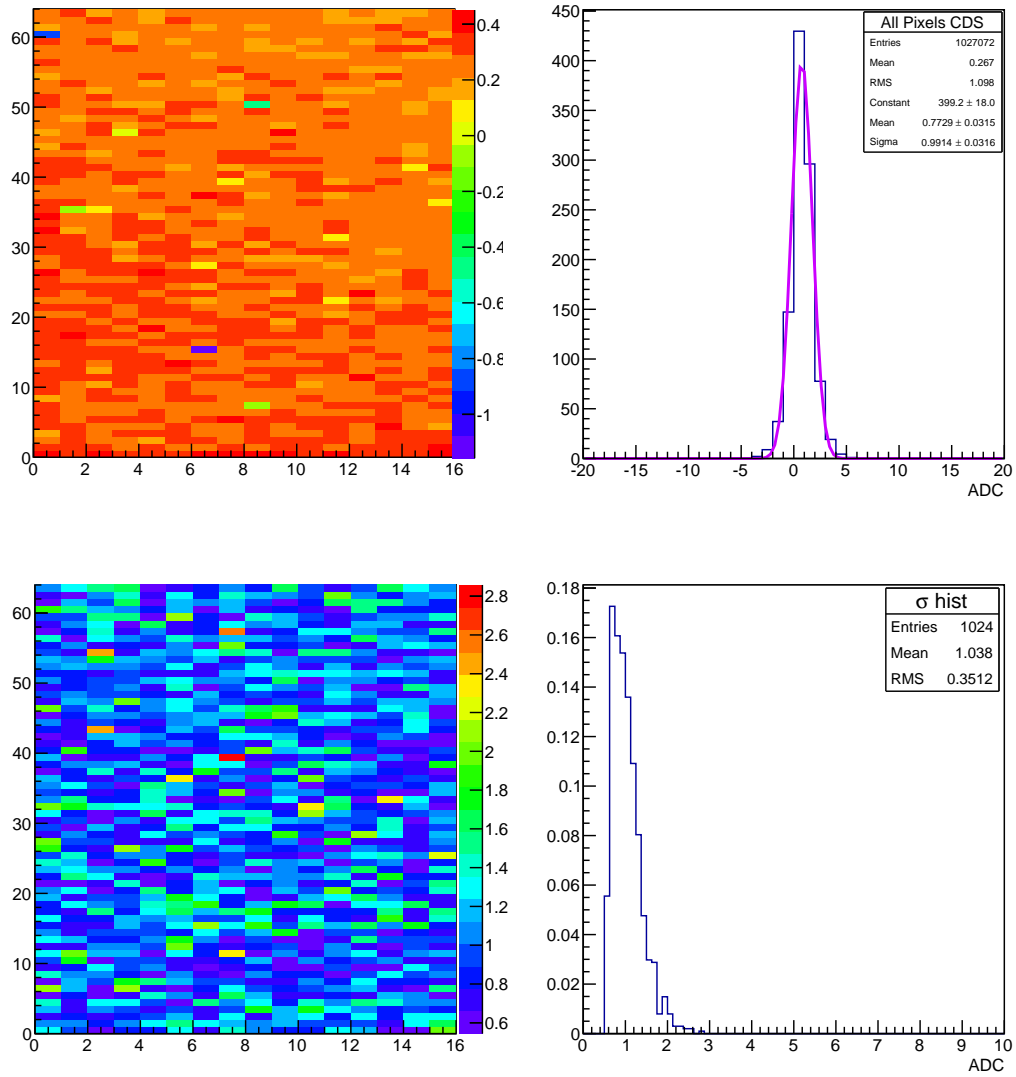


Figure 3.13: Top panels: Pedestal map (left) and distribution (right) of MIMOSA32Ter P7 matrix . The matrix consists of sixty-four rows and sixteen columns. Bottom panels: The noise map (left) and distribution (right) of the same matrix. The standard deviation of the pedestal distribution of the matrix gives the noise of the matrix.

3. CHARACTERISATION OF MONOLITHIC ACTIVE PIXEL SENSORS

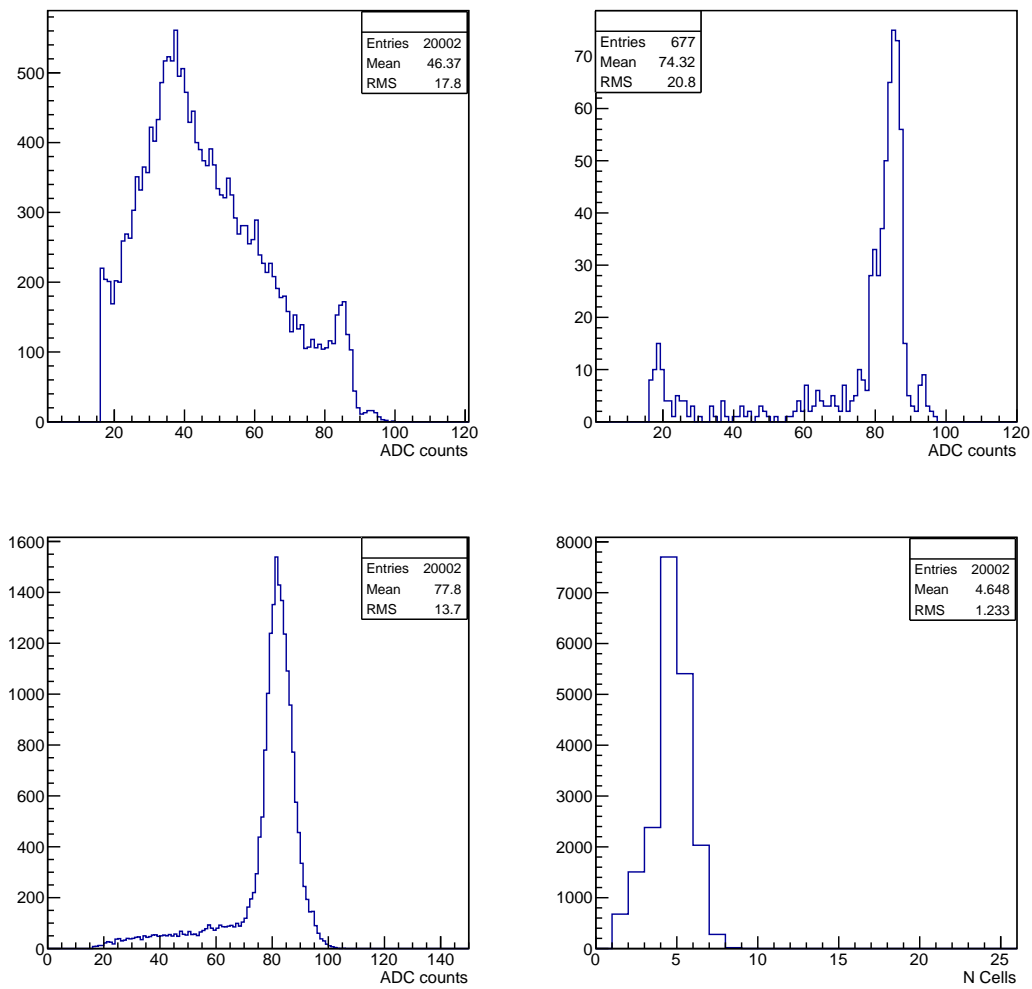


Figure 3.14: Top panels: Seed signal spectrum (left) and single pixel cluster signal distribution (right) for MIMOSA32Ter P7 matrix. Bottom panels: Cluster signal distribution (left) and cluster multiplicity (right) of the same matrix.

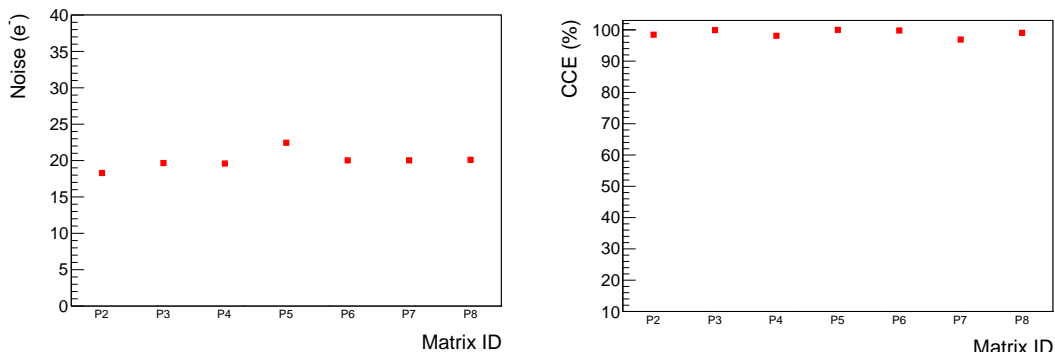


Figure 3.15: Comparison between the different matrices of MIMOSA32Ter in terms of ENC (left) and CCE (right).

Fig.3.15 shows the comparison of the MIMOSA32Ter matrices which are mentioned in Table.3.1. Each of the matrices have an octagonal collection electrode covering an area of $11 \mu\text{m}^2$. Each of them (except P2) also have a small source follower transistor (area: $11 \mu\text{m}^2$), to reduce the input capacitance which improves the charge collection properties. The P2 matrix is similar to the P6 matrix of MIMOSA32 which has pixels with only NMOS transistors. P3 and P4 matrices have a deep p-well implementation (area: $33 \mu\text{m}^2$) along with the NMOS transistor circuit. P7 and P8 also have deep p-well implementation with different spacing to the adjacent n-well of the collection electrode. P5 and P6 have small source follower transistors with a traditional MAPS circuit and without the deep p-well.

The top left panel show the comparison of the ENC. All the matrices have comparable ENC's around 20 electrons. The CCE of all the matrices are also similar around 99%, which is slightly higher than the MIMOSA32 matrices. This is due to the lower input capacitance due to smaller input transistors which increases the collected signal amplitude. The matrices with deep p-well have similar performance as the matrices without the deep p-well.

3.2.2.4 Tests with irradiated MIMOSA32Ter

The MIMOSA32Ter chips were subjected to a radiation fluence of $1 \times 10^{13} n_{eq}/\text{cm}^2$ to study the effects of NIEL on their performance. Fig.3.16 shows the ENC comparison between the non irradiated and irradiated matrices. The ENC increases to around 50

3. CHARACTERISATION OF MONOLITHIC ACTIVE PIXEL SENSORS

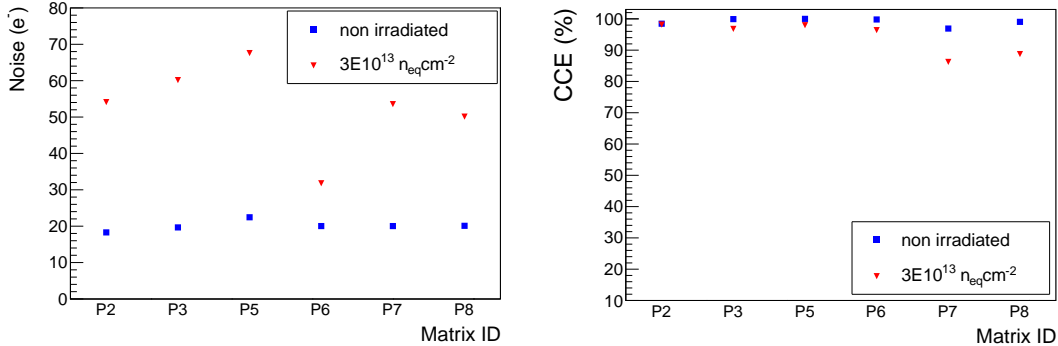


Figure 3.16: ENC (left) and CCE (right) comparison between non irradiated and irradiated matrices of MIMOSA32Ter.

electrons for the irradiated sensors. The right panel shows the CCE comparison. The irradiated P7 and P8 have some degradation in CCE.

3.2.3 MIMOSA32 and MIMOSA32Ter tests summary

MIMOSA32 and MIMOSA32Ter were the first exploratory prototypes using the TowerJazz 0.18 μm technology in the ALICE ITS Upgrade programme. They also implemented the deep p-well option to qualify the use of full CMOS inside a pixel in future prototypes. The motivation was to validate the technology for the upgrade programme and to test if the deep p-well introduces any degradation of performance in a traditional MAPS circuit. The results showed that presence of a deep p-well does not affect the performance of a traditional MAPS circuit. This validates the use of deep p-well in future prototypes with full CMOS circuitry, providing a way to proceed forward with optimization and implementation of sophisticated in-pixel circuits for the upgrade requirements. The use of small source follower transistors was to improve the charge collection properties by reducing the input capacitance of the pixel, but the small size also introduces Random Telegraph Signal (RTS) noise ([25]). There has to be a tradeoff between the input capacitance and RTS noise while optimizing the size of the input transistors in the future prototypes.

3.3 Explorer

The Explorer series are analog prototypes developed at CERN as a part of the ongoing research and developments for the ALICE ITS Upgrade to optimize the diode layout, for what concerns in particular the charge collection efficiency. This is driven by the need to decrease the power density in the detection layers of the upgraded ITS. The amount of material that can be used for power distribution and detector cooling contributes to the overall material budget of the detection layers. This has a direct effect on the maximum power density. The material budget requirement for the upgraded ITS are $0.3\%X_0$ and $0.8\%X_0$ for the inner and outer barrel respectively, as discussed in the detector specifications in Chapter 4. To respect the material budget requirements, the maximum sensor power density permissible for the upgraded ITS are $300\text{ mW}/\text{cm}^2$ for the Inner Barrel and $100\text{ mW}/\text{cm}^2$ for the Outer Barrel [6]. The detector design motivation is to reduce the power density to a much lower value than the acceptable limits.

3.3.1 Design motivation

The major contributors for power consumption in a pixel detector are the analog front-end, the digital data-processing circuits and the off-chip data transmission circuits. If we consider a pixel circuit where the collection electrode is connected to an amplifier, the analog power consumption is defined by the signal (S) to noise (N) ratio at the output of the amplifier.

The signal to noise ratio at the output of the amplifier is determined by comparing Q/C to the noise, where Q is the amplitude of the collected signal at the input and C is the equivalent pixel input capacitance [26]. In a low-power analog circuit optimized for low noise, the power consumption is dominated by the bias current (I_{bias}) of the input transistor. For a low integration time, the major noise source is the thermal noise of the input transistor which is proportional to the transistor transconductance, g_m .

$$N \propto \frac{1}{\sqrt{g_m}} \quad (3.1)$$

The transconductance, g_m is proportional to the transistor bias current, I_{bias} .

$$g_m \propto \sqrt[m]{I_{bias}} \quad (3.2)$$

3. CHARACTERISATION OF MONOLITHIC ACTIVE PIXEL SENSORS

where m is a parameter that depends on the transistor operating point ($m = 2$ in strong inversion and $m = 1$ in weak inversion).

Thus, the signal to noise ratio at the output of the amplifier is a function of the bias current, I_{bias} , which dominates the front end power consumption P .

$$\frac{S}{N} \propto \frac{Q}{C} \sqrt[2m]{I_{bias}} \propto \frac{Q}{C} \sqrt[2m]{P} \quad (3.3)$$

This gives,

$$P \propto \left(\frac{S/N}{Q/C} \right)^{2m} \quad (3.4)$$

For a given S/N and bandwidth, a higher Q/C decreases the power consumption. Thus, a low input capacitance is an important factor to reduce the analog power consumption. The design goal of the Explorer prototypes is to study and characterize the sensor Q/C .

The signal collection performance of the sensor depends on the width of the depletion layer formed under the collection electrode. In a reverse biased p-n junction, the depletion width, W is given by:

$$W = x_n + x_p = \sqrt{\frac{2\varepsilon_{Si}\varepsilon_0}{e} \left(\frac{1}{N_D} + \frac{1}{N_A} \right) (V + V_{bi})} \quad (3.5)$$

where x_n and x_p are the parts of the depletion width in the n- and p-side respectively, ε_{Si} is the relative permittivity of silicon, ε_0 is the permittivity of vacuum, e is the elementary charge, V_{bi} is built in voltage, V is the externally applied voltage and N_A and N_D are the acceptor and donor concentrations respectively.

In MAPS, the junction is usually realized by a highly doped ($N_D > 10^{18}cm^{-3}$) n implant in a low-doped ($N_A > 10^{12}cm^{-3}$) p epitaxial layer. So, the term $1/N_D$ in the above expression can be neglected, meaning that the space charge region is reaching much deeper into the epitaxial layer.

This gives,

$$W \approx x_p \approx \sqrt{\frac{2\varepsilon_{Si}\varepsilon_0}{eN_A} (V + V_{bi})} \quad (3.6)$$

Thus the depletion width, W increases with increasing reverse bias voltage, V across the junction and with decreasing dopant concentration, N_A of the (p^- epitaxial layer). A high resistivity epitaxial layer would thus facilitate larger depletion width (resistivity, $\rho \propto 1/N_A$). In a high resistivity process ($\rho = 1 \text{ k}\Omega \text{ cm}$, $N_A = 10^{13} \text{ cm}^{-3}$), the depletion width would be larger by an order of magnitude compared to a standard CMOS process ($\rho = 10 \text{ }\Omega \text{ cm}$, $N_A = 10^{15} \text{ cm}^{-3}$).

The equivalent junction capacitance per unit area can be expressed as:

$$C = \frac{\epsilon_{Si}\epsilon_0}{W} \quad (3.7)$$

An increased depletion width would reduce the capacitance of the sensing element improving Q/C .

3.3.2 Explorer prototypes

The first version of the chip, Explorer-0, was submitted in July 2012 and the second version (Explorer-1) in April 2013. Different variations of Explorer-1 were fabricated with different starting materials, namely with different thickness and resistivity of the epitaxial layer.

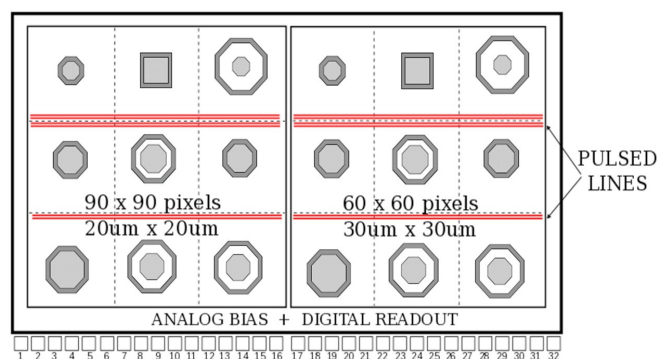


Figure 3.17: Explorer-0 floorplan.

The Explorer chip is divided into two submatrices containing pixels with two different pixel pitches: a 90x90 matrix of $20 \mu\text{m} \times 20 \mu\text{m}$ pixels and a 60x60 matrix of $30 \mu\text{m} \times 30 \mu\text{m}$ pixels. Each submatrix is divided into nine sectors, each having a different pixel variant (Fig.3.17). The cross section of the Explorer sensor input circuit is shown in Fig.3.18(a). The sensor is an n-well/p-epi reverse biased diode which is connected to

3. CHARACTERISATION OF MONOLITHIC ACTIVE PIXEL SENSORS

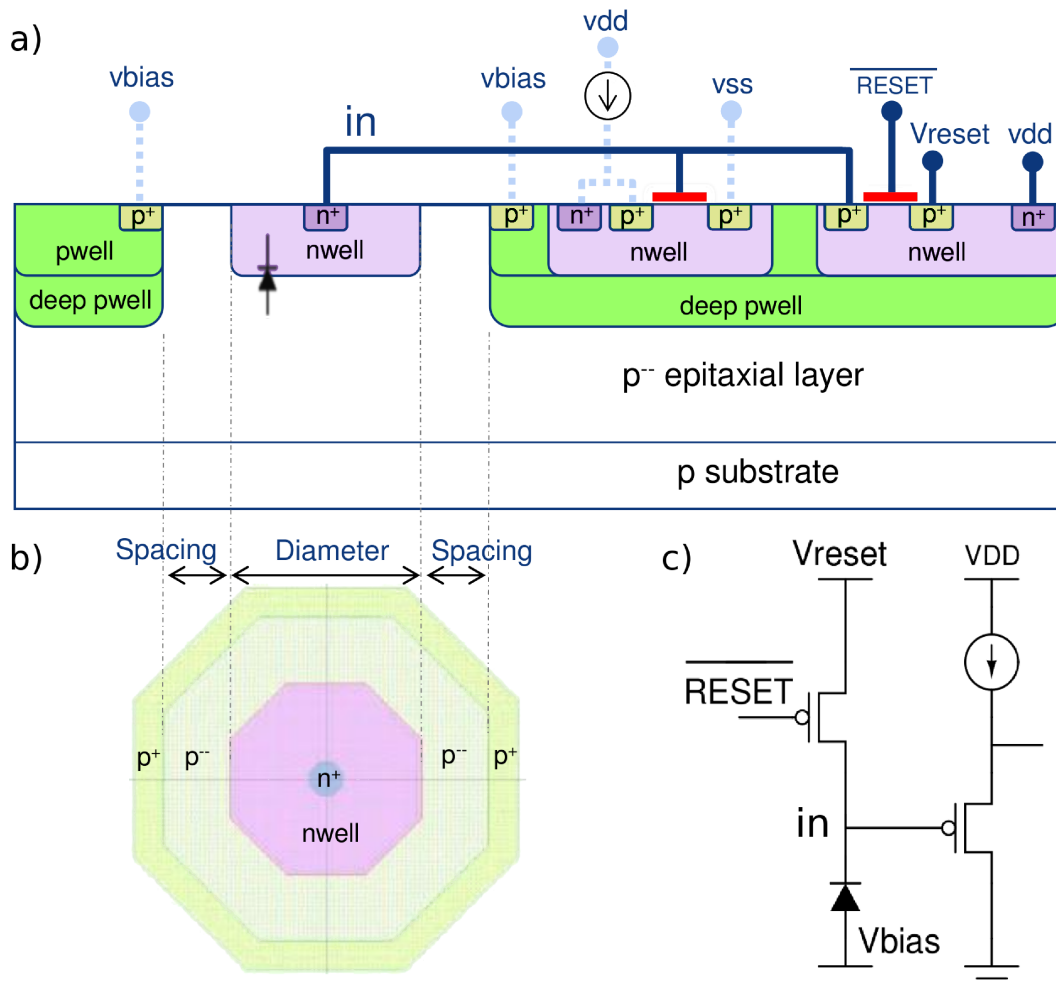


Figure 3.18: Collection electrode and pixel circuit. a) Cross section. b) Top view. c) Circuit schematic. .

a PMOS source follower. A PMOS switch resets the input node to a defined positive reset voltage V_{reset} (0.8V for tests). An important feature is the possibility to apply a negative bias (V_{bias}) to the p-epitaxial layer. A spacing is added between the n-well and p-well. Fig.3.18(b) shows a layout example (top view) with an octagonal shape n-well surrounded by a p^- spacing (epitaxial layer) and a p^+ ring used to bias the adjacent p-well. In Explorer-1, the width allocated for the collection electrode is kept constant at $7.2 \mu\text{m}$, which includes the n-well diameter plus the spacing as shown in Fig.3.18(b). The size and shape of the n-well and the spacing are varied to implement the different

pixel variants for each of the nine sectors. The shape, size of the collection electrode and the spacing for the different sectors are given in Table 3.19. The corresponding values for Explorer-0 are also given for comparison.


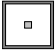

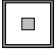

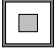



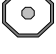



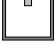



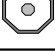
Explorer0				Explorer1			
Sector	Shape	Diameter [μm]	Spacing [μm]	Sector	Shape	Diameter [μm]	Spacing [μm]
1		2	0	1		1.13	3.035
2		3	0	2		2	2.6
3		4	0	3		3	2.1
4		3	0	4		1.13	3.035
5		3	0.6	5		2	2.6
6		3	1.04	6		3	2.1
7		2	1.54	7		1.13	0.635 (top)
8		3	0	8		1.13	0.635 (top)
9		3	1.04	9		2	2.6

Figure 3.19: Diode geometries and spacing in different sectors of Explorer-0 and Explorer-1.

The schematic diagram of Explorer front-end circuitry is shown in Fig.3.20. The PMOS source follower is connected to two independent analog memory cells. The reset transistor, which is set to a predefined voltage level, is turned on for a reset operation. This sets the output of the collection diode to a nominal value, which is immediately stored in the first memory cell. After the integration time, the signal at the output of the

3. CHARACTERISATION OF MONOLITHIC ACTIVE PIXEL SENSORS

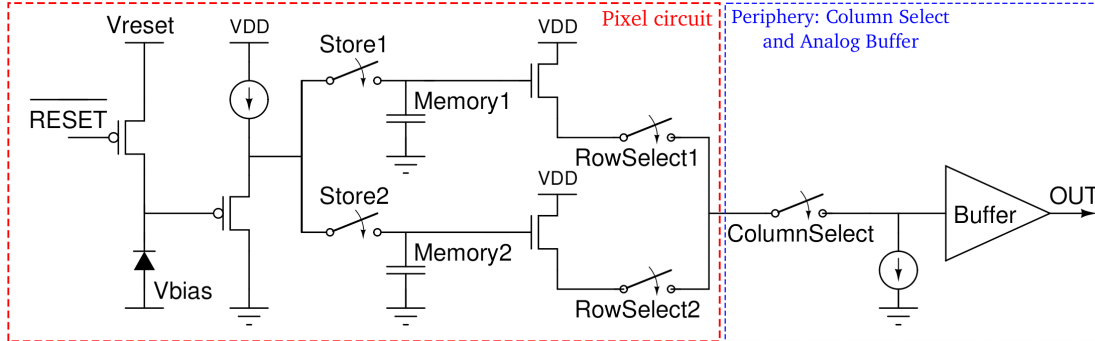


Figure 3.20: Explorer front end circuitry schematic.

collection diode is stored in the second memory cell. The memory cells are then readout sequentially by the periphery-circuit which sends the data to the off-chip digitizer. The data is then subjected to CDS and further analysis.

3.3.3 Characterization of Explorer-1

This section shows results of the tests for Explorer-1, based on the beam tests with 3.2 GeV/c positrons, conducted at DESY in November and December 2013. A test system based on a Scalable Readout System (SRS) developed at CERN [27] was used for these tests. The analysis is done using a framework developed by the CERN ITS Upgrade characterisation group. The tests are carried out on Explorer-1 with a standard epitaxial layer thickness of 18 μm and a thicker epitaxial layer of 30 μm . The tests also include the performance of irradiated Explorer-1 to study the effects of NIEL on sensor performance. First, the performance of a reference sector (Sector 5) with variations in the back-bias voltage for both 20 μm x 20 μm pixels and 30 μm x 30 μm pixels is shown. Sector 5 has an octagonal diode (diameter 2 μm) with a spacing of 2.6 μm from the neighboring p-well. A performance comparison between different sectors follows suit.

3.3.3.1 Tests with standard epitaxial layer thickness (18 μm)

(a) Study of dependence on the back bias voltage:

Fig.3.21 shows the cluster signal distribution (top panels) followed by seed signal distribution, seed signal to noise ratio and cluster multiplicity (bottom panels) for sector 5 for back bias voltages of -1V and -6V. The left and right panels correspond to 20 μm x 20 μm pixels and 30 μm x 30 μm pixels respectively.

As mentioned in the previous section, the output signal amplitude is proportional to the ratio between the signal charge collected by the pixel (Q) and the input capacitance (C).

The cluster signal represents the total charge in a cluster. It is higher for a back bias voltage of $-6V$ as shown in the top panels of Fig.3.21. The input capacitance is lower for a back bias voltage of $-6V$, improving the Q/C ratio, with respect to a back bias voltage of $-1V$. This accounts for a larger cluster signal at $-6V$.

The fraction of the total cluster charge collected in the seed pixel is higher at a back bias voltage of $-6V$ compared to that corresponding to $-1V$. This is due to the increased depletion width at $-6V$. The bigger depletion volume has a higher probability of collecting the diffusing electrons which may have diffused into the neighboring pixels in case of a smaller depletion volume at $-1V$ resulting in the increased signal charge collection in the seed pixel in a cluster. The seed signal to noise ratio is also higher at $-6V$. The ratio between the seed signal and the seed signal to noise ratio is almost the same for $-1V$ and $-6V$, implying that the difference between the noise at the two back bias voltages is not significant.

The bigger depletion volume at $-6V$ also affects the cluster multiplicity. The higher seed signal collection at $-6V$ reduces the cluster multiplicity.

The results for the $30\mu\text{m}$ pitch pixels show similar trends as that in $20\mu\text{m}$ pitch pixels.

(b) Study of dependence on spacing:

Fig.3.22 shows the results for all the sectors of Explorer-1 for $-1V$ and $-6V$ back-bias voltage. The top panels show the cluster signal peak comparison, the middle panels show the seed signal to noise ratio peak comparison and the bottom panels show the cluster multiplicity comparison. The left and right panels show the results for $20\mu\text{m}$ pitch pixels and $30\mu\text{m}$ pitch pixels respectively. For each sector, the respective values for cluster signal is larger at $-6V$ than $-1V$ due to the reduced capacitance at $-6V$. The sectors differ in the geometries of the collection electrode and their distance to the adjacent deep P-well (spacing). Increased spacing between the collection electrode and the adjacent p-well increases the depletion width on the sides of the collection electrode and thus reducing the capacitance.

3. CHARACTERISATION OF MONOLITHIC ACTIVE PIXEL SENSORS

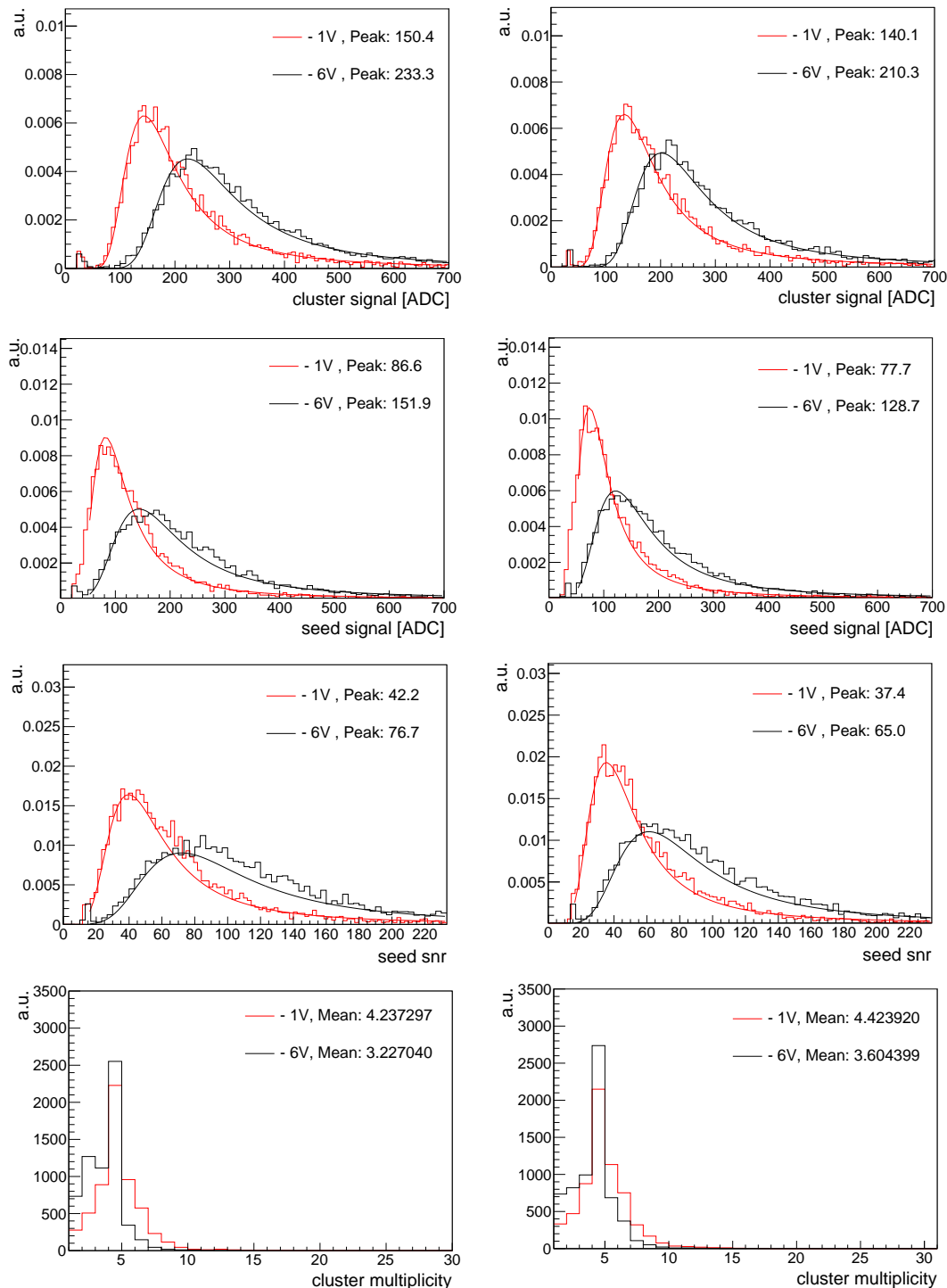


Figure 3.21: Performance of sector 5 of Explorer-1 with a standard epitaxial layer thickness of $18\ \mu\text{m}$ at a back bias voltage of -1V and -6V . From top to bottom, the panels show the cluster signal distribution followed by seed signal distribution, seed signal to noise distribution and cluster multiplicity respectively. The left and right panels represent $20\ \mu\text{m} \times 20\ \mu\text{m}$ pixels and $30\ \mu\text{m} \times 30\ \mu\text{m}$ pixels respectively.

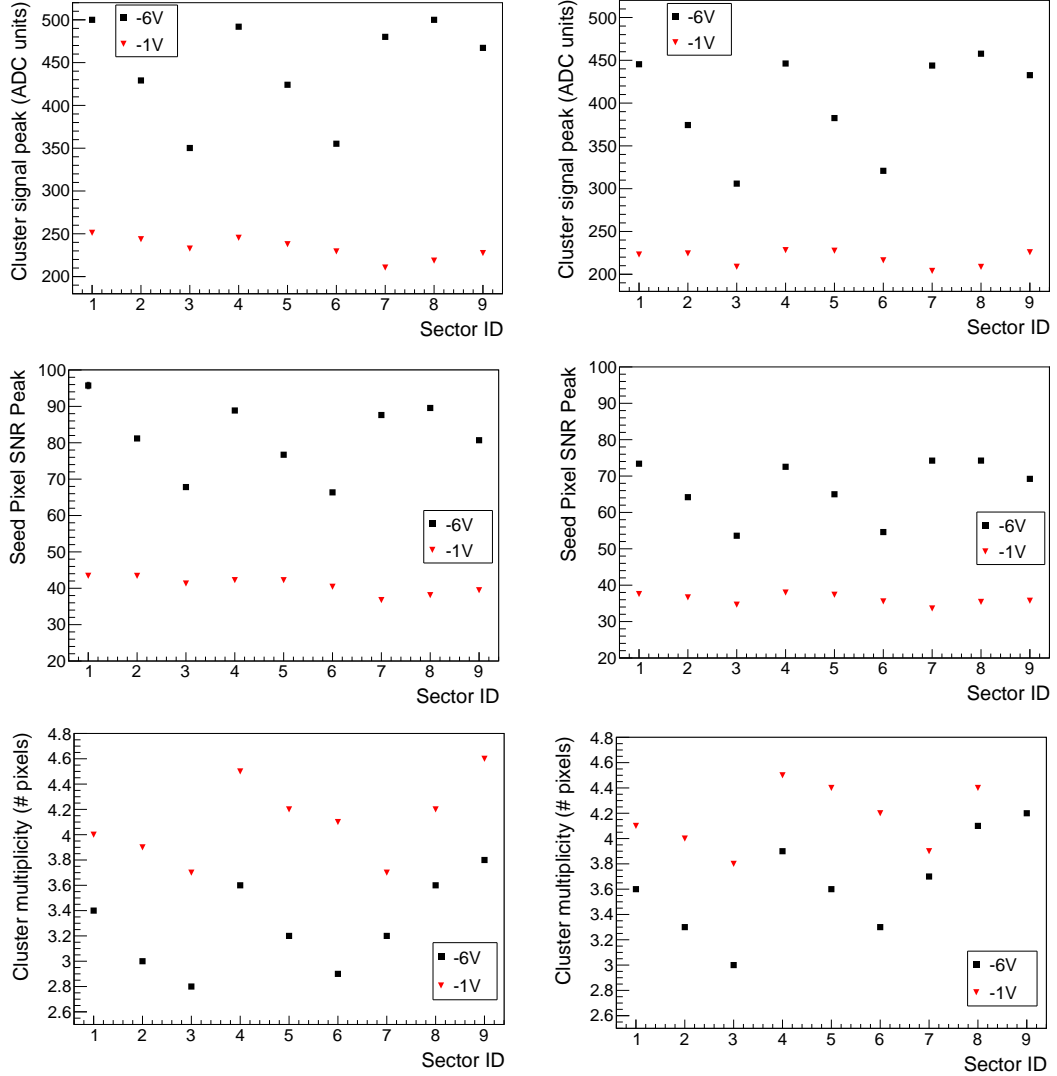


Figure 3.22: Comparison between the different sectors of Explorer-1 with a standard epitaxial layer thickness of $18\ \mu\text{m}$ for back bias voltage of -6V and -1V . The top panels show the cluster signal followed by seed signal to noise ratio (middle panels) and cluster multiplicity (bottom panels). The left and right panels represent $20\ \mu\text{m} \times 20\ \mu\text{m}$ pixels and $30\ \mu\text{m} \times 30\ \mu\text{m}$ pixels respectively.

Sectors 1 and 4 have the highest spacing ($3.035\ \mu\text{m}$) and hence have larger cluster signal than the other sectors as shown in the top panels of Fig. 3.22. Sectors 3 and 6 have the lowest spacing ($2.1\ \mu\text{m}$) translating to a higher capacitance and hence the lowest cluster signal among all the sectors. The seed signal to noise ratio shows the

3. CHARACTERISATION OF MONOLITHIC ACTIVE PIXEL SENSORS

same trend among the sectors since a large cluster signal also implies a large signal collected in the seed pixel.

The results are similar for the 30 μm pitch pixels.

3.3.3.2 Comparison between different starting materials

Fig.3.23 shows the effects of a 30 μm thick epitaxial layer and its comparison with the previous results for 18 μm thick epitaxial layer for sector 5 for back bias voltages of -1V and -6V. The top panels show the cluster signal distribution followed by seed signal distribution, seed signal to noise ratio and cluster multiplicity (bottom panels) for sector 5 for back bias voltages of -1V and -6V. The left and right panels show the results for 20 μm pitch pixels and 30 μm pitch pixels respectively.

A thicker epitaxial layer would result in an increase in the number of charge carriers generated. A thicker epitaxial layer also implies a larger non depleted volume with respect to a standard epitaxial layer for the same back bias voltage. These two effects are competing.

The increase of generated charge is demonstrated by the increased cluster charge for 30 μm thick epitaxial layer pixels as shown in Fig. 3.23 (top panels). This, along with the competing effect of larger non depleted volume influence the charge collection in the seed pixel. For a back bias of -6V, the seed charge is higher for the pixels with 30 μm epitaxial layer, whereas for a back bias of -1V, the seed charge is higher for the 18 μm epitaxial layer pixels. This is also reflected in the seed signal to noise ratio. A larger non depleted volume for 30 μm thick epitaxial layer results in a higher cluster multiplicity.

The results for the 30 μm pitch pixels are similar to that of the 20 μm pitch pixels.

Fig.3.24 shows the summary of these effects for sector 5 for both 20 μm pitch pixels (left panel) and 30 μm pitch pixels (right panel). The plots show the comparison between cluster signal peak, seed signal peak and mean cluster multiplicity for 18 μm and 30 μm thick epitaxial layers.

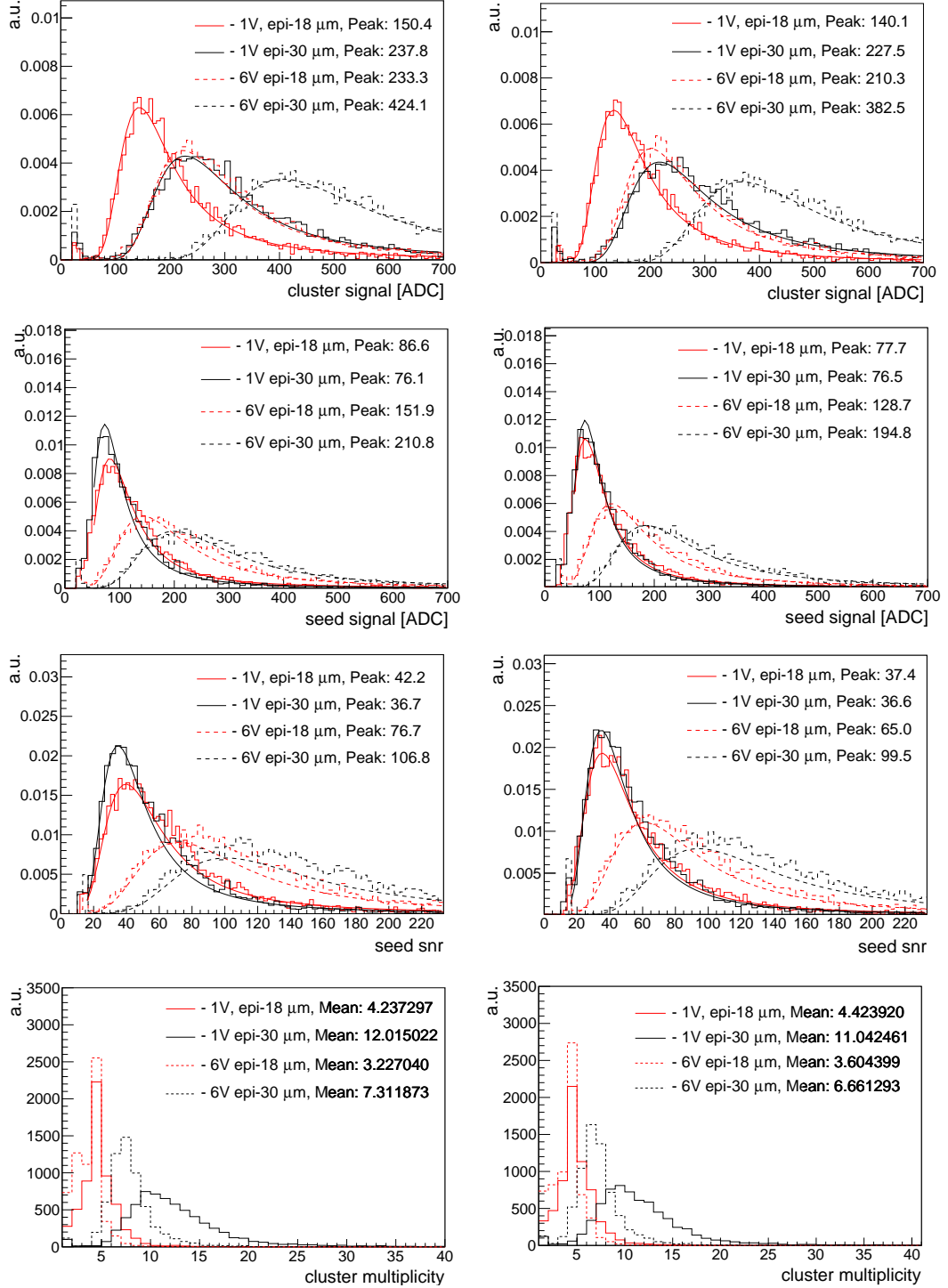


Figure 3.23: Performance comparison between two variants of Explorer-1 having an epitaxial layer thickness of 18 μm and 30 μm for sector 5 for a back bias voltage of -1V and -6V. From top to bottom, the panels show the cluster signal distribution followed by seed signal distribution, seed signal to noise distribution and cluster multiplicity respectively. The left and right panels represent 20 μm x 20 μm pixels and 30 μm x 30 μm pixels respectively.

3. CHARACTERISATION OF MONOLITHIC ACTIVE PIXEL SENSORS

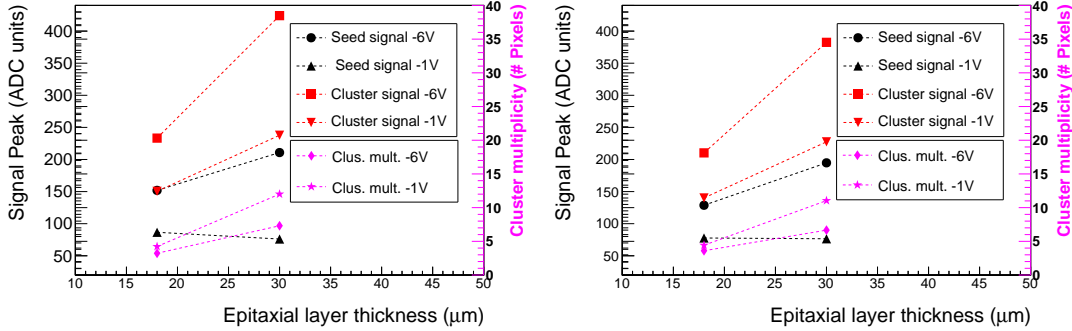


Figure 3.24: Performance comparison summary between two variants of Explorer-1 having an epitaxial layer thickness of 18 μm and 30 μm for sector 5 for a back bias voltage of -1V and -6V. The plots include cluster signal peak, seed signal peak and mean cluster multiplicity. The left and right panel represents 20 μm x 20 μm pixels and 30 μm x 30 μm pixels respectively.

Fig.3.25 shows the comparison between all the sectors of Explorer-1 with a 30 μm thick epitaxial layer for -1V and -6V back-bias voltage. The top panels show the cluster signal peak comparison. The middle panels show the seed signal to noise ratio peak and the bottom panels show the mean cluster multiplicity for all sectors. The left and right panels show the results for 20 μm pitch pixels and 30 μm pitch pixels respectively.

For each sector, the respective values for cluster signal is larger at -6V than -1V due to the reduced capacitance at -6V.

The cluster signal is higher in sectors 1 and 4 which have the largest spacing of 3.035 μm between the collection electrode and the adjacent p-wells. A larger spacing increases the depletion width in the sides of the collection electrode and reduces the input capacitance, resulting in a larger cluster signal. Sectors 3 and 6 have the smallest spacing (2.1 μm) contributing to a higher capacitance resulting in the lowest cluster signal among all the sectors. A large cluster signal also implies the increase in the seed signal of the cluster which also reflects in the seed signal to noise ratio. The sectors show the same trend in the seed signal to noise ratio.

The results show similar trends for both the pixel sizes.

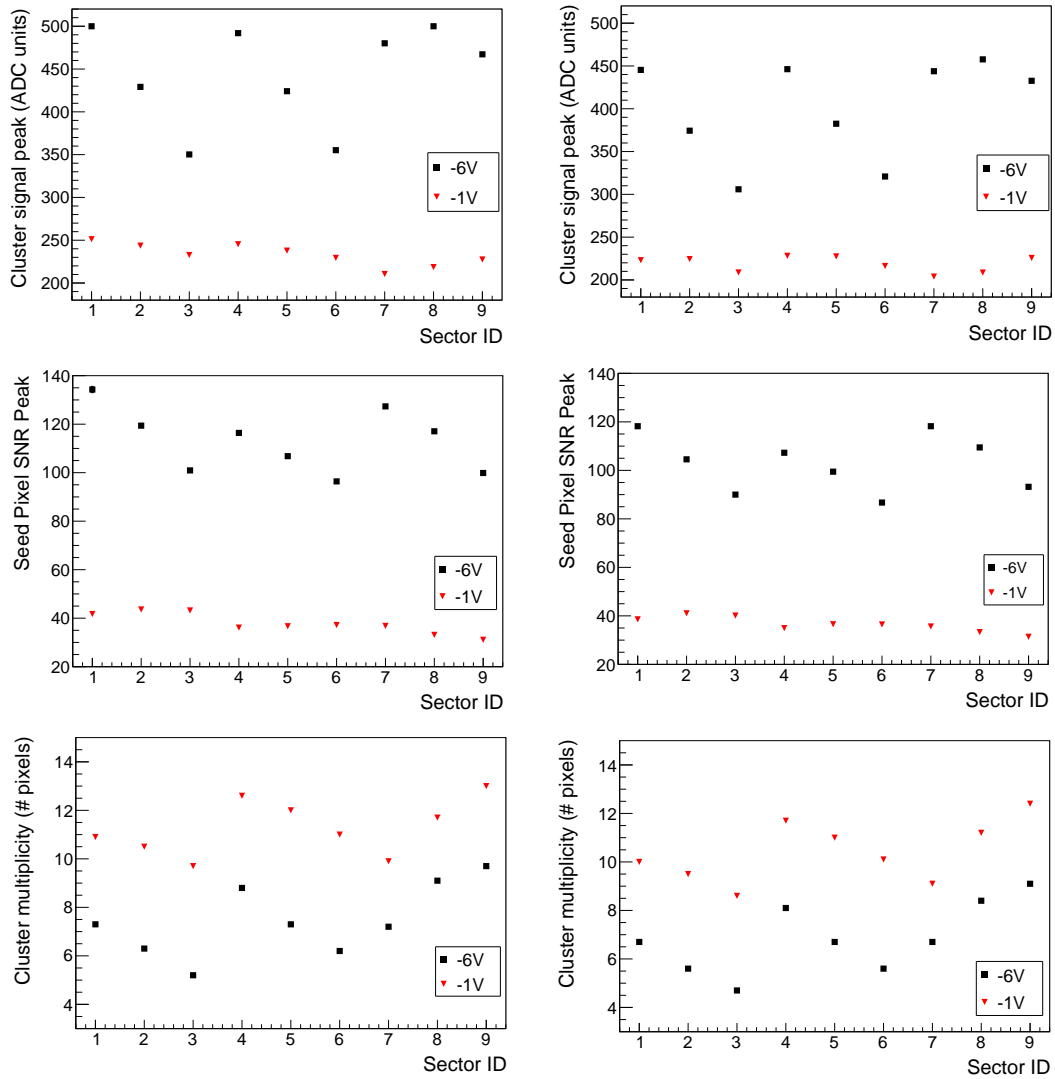


Figure 3.25: Comparison between the different sectors of Explorer-1 with an epitaxial layer thickness of $30\ \mu\text{m}$ for back bias voltage of -6V and -1V . The top panels show the cluster signal peak followed by seed signal to noise ratio peak (middle panels) and mean cluster multiplicity (bottom panels).

3. CHARACTERISATION OF MONOLITHIC ACTIVE PIXEL SENSORS

3.3.3.3 Tests with irradiated chips

To test bulk effects generated by NIEL, the Explorer sensor prototype structures have been irradiated with a fluence of $2.5 \times 10^{12} n_{eq}/cm^2$ and $1 \times 10^{13} n_{eq}/cm^2$ using neutrons from the TRIGA MarkII Reactor at JSI in Ljubljana, before being bonded on the test boards.

NIEL effects include bulk defects in silicon, introducing recombination points and charge trapping centres. This may lead to a decrease in the charge collected. Regeneration points may also be created which may increase the leakage current and hence the noise.

Fig.3.26 shows the cluster signal distribution (top panels) followed by seed signal distribution, seed signal to noise ratio and cluster multiplicity (bottom panels) of irradiated Explorer-1 with 18 μm thick epitaxial layer for -6V back bias voltage and compared with the non irradiated Explorer-1 results for the same back bias voltage. The left and right panels show the results for 20 μm pitch pixels and 30 μm pitch pixels respectively.

The recombination and trapping of the electrons leads to the decrease of signal charge. The cluster signal decreases with increasing fluence, though only slightly. The seed signal collection is affected marginally. The signal to noise ratio is almost unaffected for a fluence of $2.5 \times 10^{12} n_{eq}/cm^2$ but is reduced for a fluence of $1 \times 10^{13} n_{eq}/cm^2$.

The effects on 30 $\mu m \times 30 \mu m$ are similar.

Fig.3.27 shows the summary of these effects for both 20 μm pitch pixels (left panel) and 30 μm pitch pixels (right panel). The plots show the comparison between cluster signal peak, seed signal peak and seed signal to noise ratio for sector 5 of irradiated and non irradiated Explorer-1 with a standard epitaxial layer thickness of 18 μm .

Fig.3.28 shows the results for all the irradiated sectors of Explorer-1 for -6V back-bias voltage and are compared with the results for the non irradiated sectors. The top panels show the cluster signal peak comparison. The middle panels show the seed signal to noise ratio peak and the bottom panels show the mean cluster multiplicity for all sectors. The left and right panels show the results for 20 μm pitch pixels and 30 μm pitch pixels respectively.

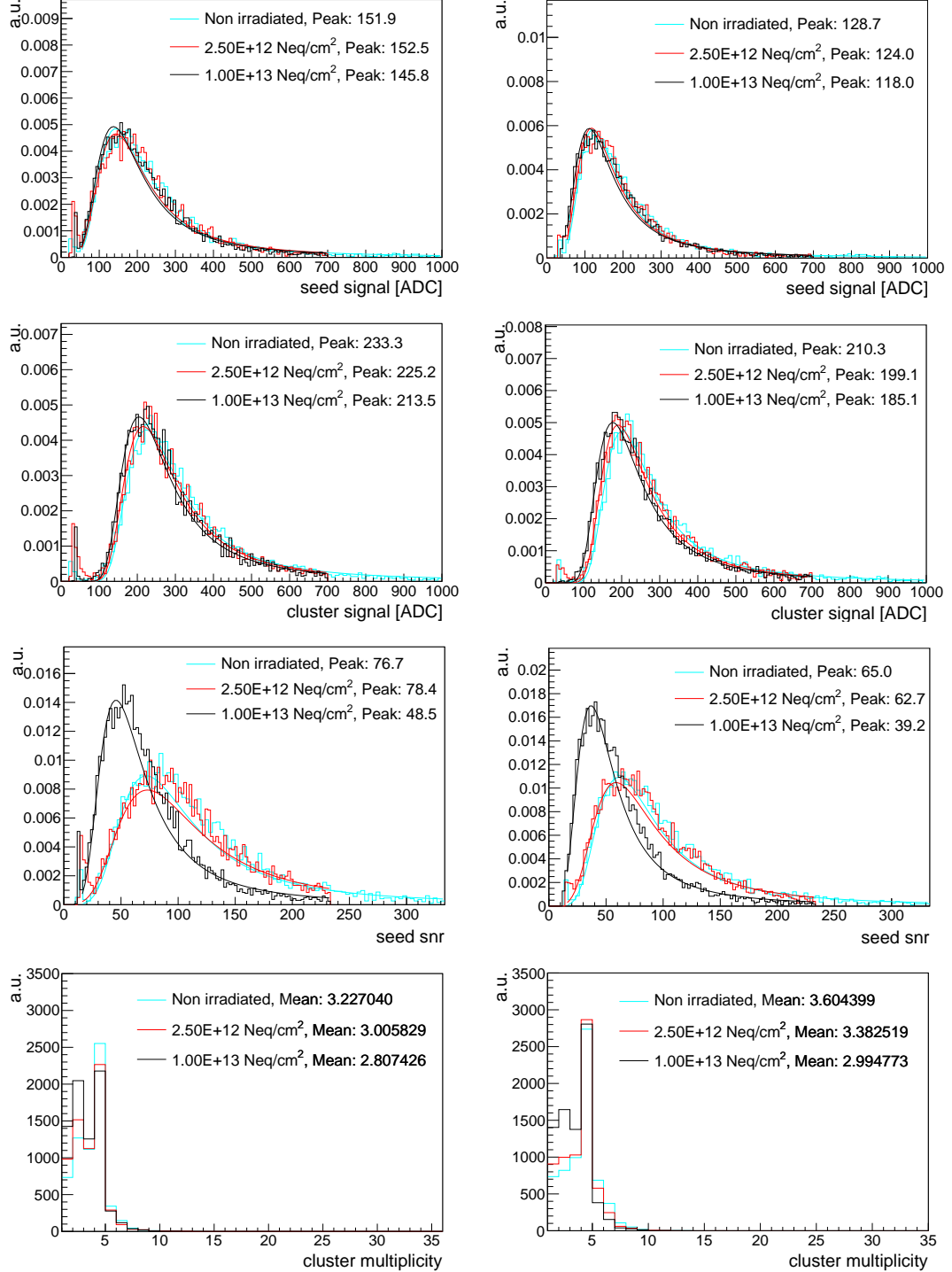


Figure 3.26: Comparison between the non irradiated and irradiated Explorer-1 (Sector 5) for a back bias voltage of -6V. The seed charge (top panel), cluster charge (middle panel) are slightly affected. The seed signal to noise ratio is reduced for the highest fluence. The left and right panels represents 20 μm x 20 μm pixels and 30 μm x 30 μm pixels respectively.

3. CHARACTERISATION OF MONOLITHIC ACTIVE PIXEL SENSORS

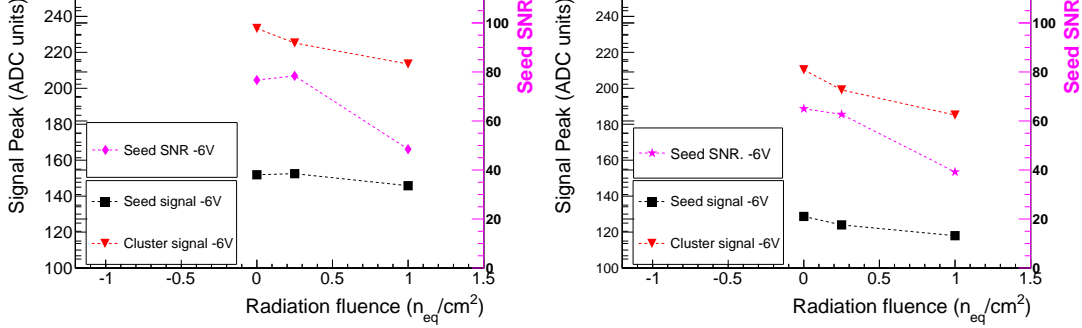


Figure 3.27: Comparison between the non irradiated and irradiated Explorer-1 of Sector 5 for a back bias voltage of -6V. The plots include cluster signal peak, seed signal peak and seed signal to noise ratio. The left and right panels represent 20 μm x 20 μm pixels and 30 μm x 30 μm pixels respectively.

The irradiated sectors follow the same trend as their non irradiated counterparts. For both the levels of irradiation, the cluster signal is higher in sectors 1 and 4 having the largest spacing of 3.035 μm between the collection electrode and the adjacent p-wells due to a reduced the input capacitance. Sectors 3 and 6 have the lowest cluster signal among all the sectors for all levels of irradiation due to the smallest spacing (2.1 μm). The sectors show the same trend in the seed signal to noise ratio.

The results are similar for the 30 μm x 30 μm pixels.

3.3.4 Explorer-1 tests summary

Explorer prototypes are developed at CERN to study the Q/C ratio of pixel circuits. The studies showed that the Q/C increases with increasing back bias voltage and with increasing spacing between the collection diode and the adjacent p-well due to reduced input capacitance resulting from a widening depletion region. Explorer-1 with different epitaxial layer thicknesses of 18 μm and 30 μm are also compared. A thicker epitaxial layer results in increased charge carrier generation leading to a larger cluster signal. The seed signal charge for the 30 μm , on the other hand increases at higher back bias voltage (-6V) but decreases at low back bias voltage (-1V) compared to the 18 μm thick epitaxial layer. This is because there are two competing effects in a thicker epitaxial layer- higher charge carrier generation, and larger non-depleted area for diffusing electrons to escape

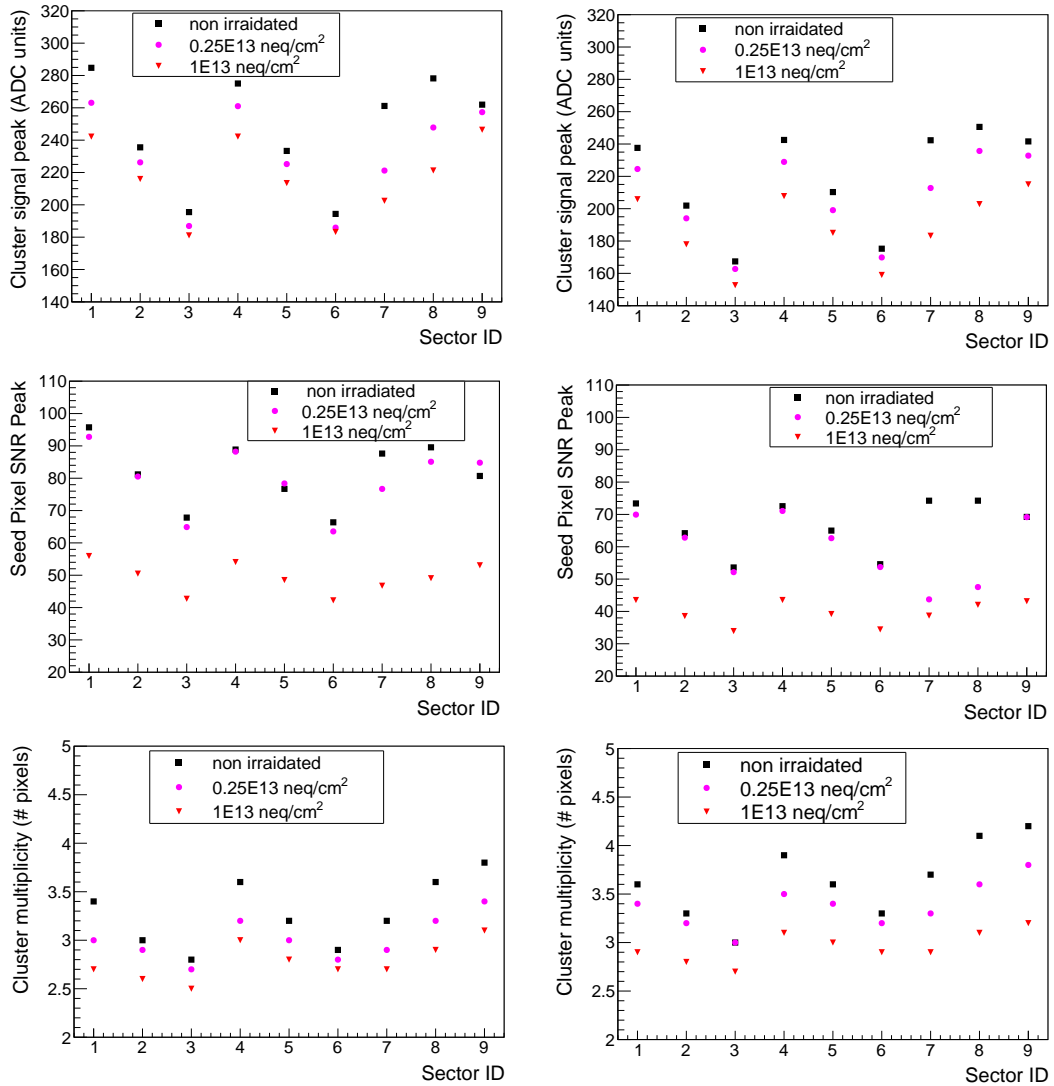


Figure 3.28: Comparison between the non irradiated and irradiated Explorer-1 for all sectors at a back bias voltage of -6V. The top panels show the cluster multiplicity. The middle panels show the seed pixel signal to noise ratio and the bottom panels show the noise. The left and right panels represents 20 μm x 20 μm pixels and 30 μm x 30 μm pixels respectively.

3. CHARACTERISATION OF MONOLITHIC ACTIVE PIXEL SENSORS

into neighboring pixels of a cluster. The dominance of one effect over another changes with the back bias voltage. The square and octagonal diodes have similar charge collection properties. The 30 μm pitch pixels show similar trends as their 20 μm pitch counterparts.

The understanding of the Q/C at the collection node of the pixel circuit and its dependence on the spacing and back bias voltage, along with the effects of different starting materials is an important step in the optimization process of the analog frontend and improve the signal to noise ratio of the full scale detector. Improvement of the signal to noise ratio has a direct effect on the reduction of the power density of the final detector.

3.4 Developments towards a full scale pixel chip

The pixel prototype circuits MIMOSA32, MIMOSA32Ter and Explorer-1 described in this chapter, form a part of a wide range of prototype circuits which are being developed within the ALICE ITS Upgrade collaboration. These prototypes address design features of various building blocks of a final architecture towards a full scale pixel chip.

There are four different architectures which are being developed and studied for the upgrade. These architectures explore a wide spectrum of implementations offered by the TowerJazz technology. These include MISTRAL (MIMOSA Sensor for the inner tracker of ALICE), ASTRAL (AROM Sensor for the inner tracker of ALICE), CHERWELL and ALPIDE (ALICE Pixel Detector). MISTRAL and ASTRAL are being developed at IPHC Strasbourg and Irfu Saclay and are evolved from the ULTIMATE sensor [21] developed for the STAR Heavy Flavor Tracker (HFT) at RHIC. CHERWELL is designed by the STFC-RAL group in the UK. ALPIDE is being developed by CERN, INFN (Cagliari and Torino, Italy), CCNU (Wuhan, China), NIKHEF (The Netherlands) and Yonsei (South Korea). The important features of these architectures are mentioned below. Further details can be found here [6].

3.4.1 MISTRAL

The design is based on a rolling-shutter readout with amplification and correlated double sampling inside each pixel. Fig.3.29 shows a prototype in-pixel circuit of this architecture. MISTRAL will be equipped with column level discriminators allowing simultane-

3.4 Developments towards a full scale pixel chip

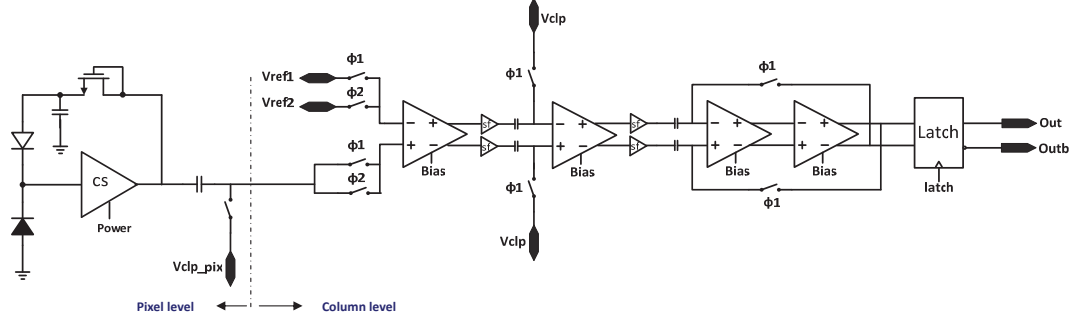


Figure 3.29: MISTRAL in-pixel and end of column circuit [6].

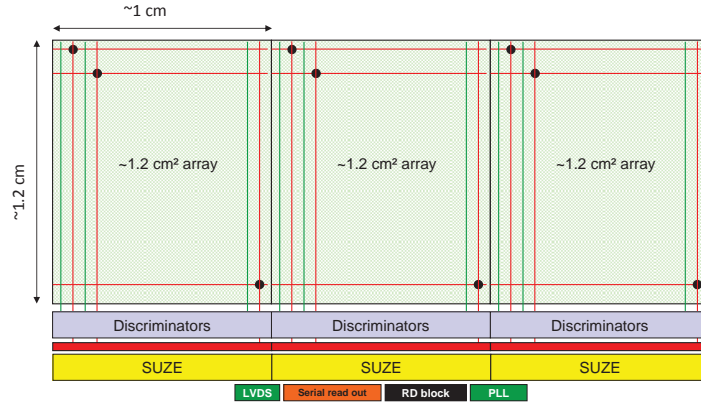


Figure 3.30: MISTRAL layout [6].

ous readout of two rows in rolling-shutter mode to give an integration time of $30 \mu\text{s}$. The target pixel size is about $22 \mu\text{m} \times 33.3 \mu\text{m}$, providing a single point resolution of about $5 \mu\text{m}$. The expected power consumption is about 200 mW cm^{-2} . The first prototypes for this architecture were MIMOSA32 and MIMOSA32Ter, which are explained earlier in this chapter.

MISTRAL will be built from three Full Scale Building Blocks (FSBB), as shown in Fig.3.30, with a surface of $1.5 \text{ cm} \times 3.0 \text{ cm}$ containing 375 rows and 1300 columns in total. The discriminator outputs will be processed through an integrated zero suppression logic: SUZE-02, which is the downstream part of both MISTRAL and ASTRAL. The data is stored in a memory of four SRAM blocks (32×512 bits), allowing both continuous or triggered readout. The data is shipped out with a high speed serial link, with a maximum SUZE-02 output rate of 640 Mbit s^{-1} .

3. CHARACTERISATION OF MONOLITHIC ACTIVE PIXEL SENSORS

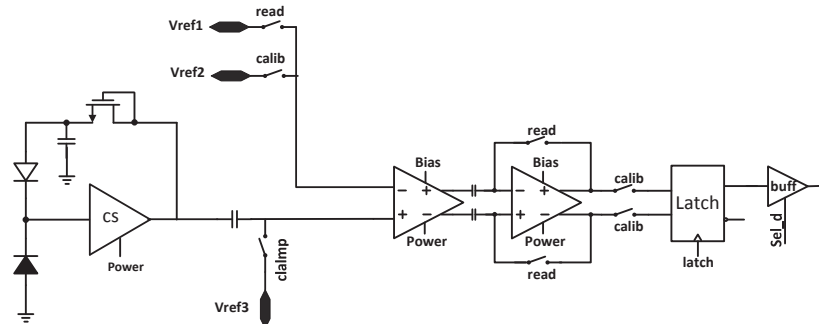


Figure 3.31: ASTRAL in-pixel circuit [6].

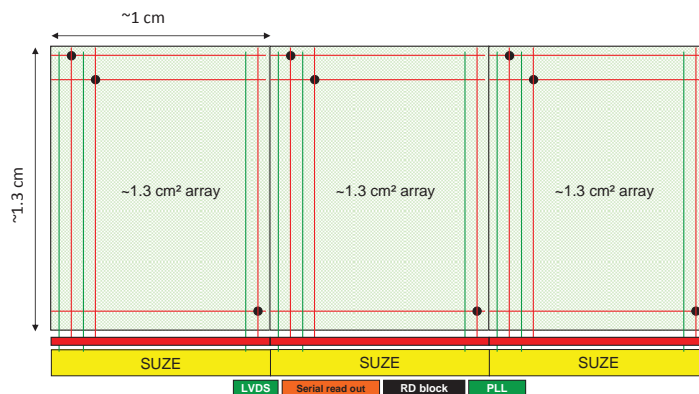


Figure 3.32: ASTRAL layout [6].

3.4.2 ASTRAL

This is an alternative design to the MISTRAL which is faster and less power consuming. The design consists of an accelerated read-out based on the AROM (accelerated read-out MIMOSA) concept. The prototype in-pixel circuit is shown in Fig.3.31. The architecture uses in-pixel signal discriminators which replaces the analogue signals driving over long traces with digital signals. This has certain advantages over the MISTRAL architecture, particularly the doubling of the pixel readout frequency and reduction of power consumption. The dimensions of the peripheral circuitry is also reduced due to the absence of the column level discriminators. The layout is shown in Fig.3.30.

There are two variants of ASTRAL which are considered: ASTRAL-IN (targeted for the ITS inner layers) and ASTRAL-OUT (suited for the ITS outer layers). ASTRAL-IN has a pixel size of about $24 \mu\text{m} \times 31 \mu\text{m}$, providing a single point resolution of about $5 \mu\text{m}$ and the expected power consumption is about 85 mW cm^{-2} . The expected frame

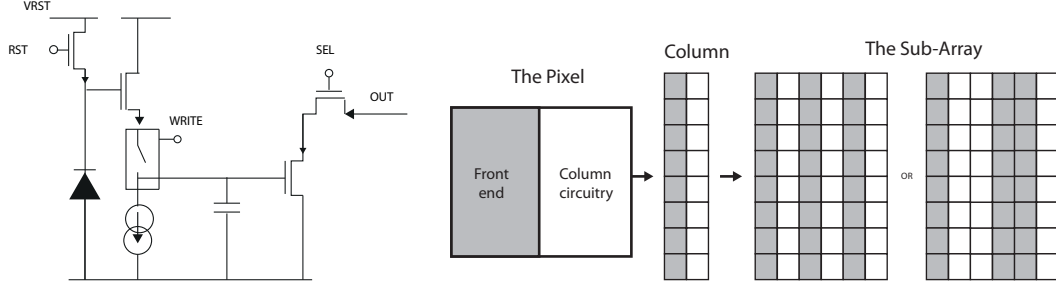


Figure 3.33: CHERWELL in-pixel circuit (left) and strixel architecture (right) [6].

read-out time is approximately $20 \mu\text{s}$, considering simultaneous double-row readout. ASTRAL-OUT has larger pixels ($36 \mu\text{m} \times 31 \mu\text{m}$) providing a lower power density of about 60 mW cm^{-2} . The expected single point resolution is about $7 \mu\text{m}$.

3.4.3 CHERWELL

The design is based on a rolling-shutter read-out and allows correlated double sampling. The in-pixel circuit is shown in the left panel of Fig.3.33. The pixels are grouped into strixels as shown in the right panel of Fig.3.33. This architecture allows reduction of dead area at the periphery by incorporating the amplifiers, comparators and memories within the matrix. The number of pixels in a strixel and their geometry (horizontal or vertical pitch) can be customized as per the requirements. Within a strixel, the pixels are read in rolling-shutter mode and the pseudo-differential signals are compared against a defined threshold to identify the particle hits. The address of hit-pixels are stored in SRAMs within the strixel itself.

In the latest prototype test structure, CHERWELL-2, each strixel consists of a column of 128 pixels of dimensions $20 \mu\text{m} \times 20 \mu\text{m}$. There are 128 strixels placed next to each other to make a 128×128 pixel array. The expected integration time and the power consumption is $30 \mu\text{s}$ and 90 mW cm^{-2} respectively.

3.4.4 ALPIDE

The design is based on a low-power in-pixel discriminator circuit that drives an in-matrix asynchronous address encoder circuit. The address encoder output is read out by an end-of-column lossless data compression and de-randomising circuit. The in-pixel discriminator eliminates the need for an analogue column driver, reducing significantly

3. CHARACTERISATION OF MONOLITHIC ACTIVE PIXEL SENSORS

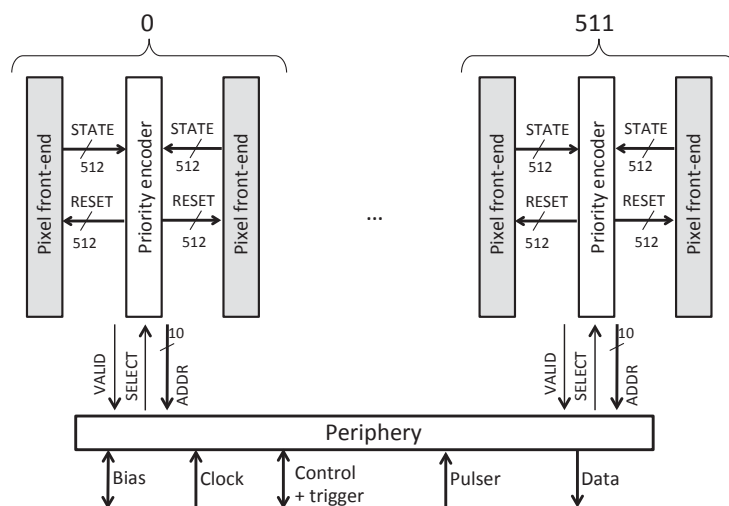


Figure 3.34: ALPIDE functional block diagram [6].

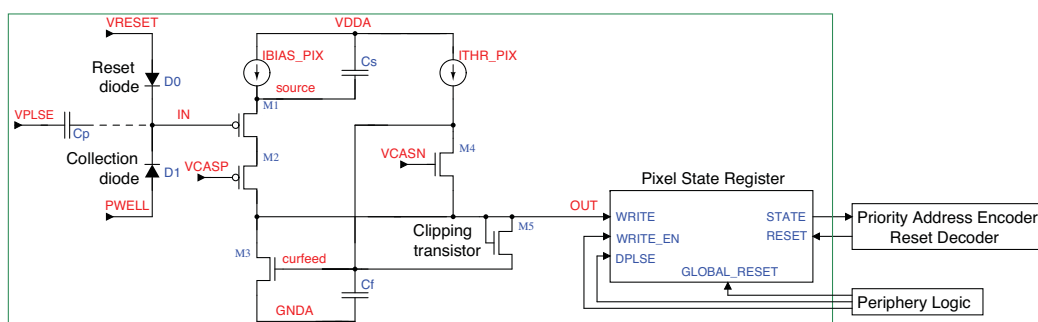


Figure 3.35: ALPIDE in-pixel circuit [6].

the power consumption and allowing a faster read-out. A functional diagram of the circuit is shown in Fig.3.34. The in-pixel circuit is shown in Fig.3.35. The circuit is operated in triggered mode. The output of the front-end is latched in the presence of a trigger. An asynchronous priority encoder network in every double column encodes the address of the hit pixels and feeds the end-of-column circuit. The end-of-column circuit compresses the data, after which the data of all columns is multiplexed into a common multi-event memory which serves as a de-randomising circuit.

The pixel size is $28 \mu\text{m} \times 28 \mu\text{m}$. The integration time is $4 \mu\text{s}$ and the expected power consumption is less than 50mW cm^{-2} . Explorer-0 and Explorer-1 are the prototypes for ALPIDE to optimize the pixel geometry and study the effects of back-bias which are explained earlier in this chapter.

3.5 Future plans

Several prototype structures of the different building blocks corresponding to the different architectures and their design streams have been fabricated and characterized throughout 2012 and 2013. The TowerJazz technology is qualified and the design streams have validated key components in terms of charge collection efficiency, detection efficiency and radiation tolerance, leading towards the development of full scale prototypes. The full prototypes of the different design streams will be fabricated and characterized throughout 2014 and early 2015. Based on these results, further optimizations and iterations will be carried out towards a decision on the final architecture for the upgrade. The submission of a prototype of the final circuit is foreseen in late 2015. After successful characterization, the final circuit will be sent for mass production planned in 2016.

3. CHARACTERISATION OF MONOLITHIC ACTIVE PIXEL SENSORS

4

Detector Performance

4.1 Introduction

This chapter studies the performance of the new ITS detector. In order to achieve the physics goals described in Chapter 1 , the ITS upgrade should allow to improve the following.

- the resolution of the track impact parameter by a factor ≈ 3 or better below $p_T = 1 \text{ GeV}/c$ with respect to the present ITS;
- the stand-alone tracking capability with a momentum resolution of a few percents up to $20 \text{ GeV}/c$ and coverage in transverse momentum as complete as possible, in particular down to very low momenta;
- the readout rate capabilities.

The performance of a baseline configuration (referred to as the 'Upgraded ITS' subsequently in this chapter) is studied and compared to the present ITS performance. Some alternative configurations with different characteristics such as different material budget and/or the intrinsic resolution and position of the layers are studied. The detector performance in case of a dramatic reduction of detector efficiency (presence of one dead layer) is also studied.

4.2 Experimental conditions (ALICE Run 3) for simulation studies

This section describes the conditions expected during ALICE Run 3 which guided the specifications for the upgraded ITS.

Beam pipe: The vacuum beam pipe represents the main interface between the experiment and the LHC. The present beam pipe is 4.82 m long with a central section made of a straight beryllium tube of length 3.95 m, wall thickness 0.8 mm and outer radius 29.8 mm [28]. Current studies indicate that it should be possible to arrive at a beampipe inner radius of 17.2 mm for the upgrade scenario, compared to the present value of 29 mm. Since its feasibility is yet to be confirmed by further studies, a conservative number of 19 mm is assumed for the beampipe inner radius. Thus, the baseline scenario for the ALICE upgrade includes the installation of a new beam pipe with a wall thickness of 0.8 mm and an outer radius of 19.8 mm.

Particle load:

The maximum hit density of particles in the layers of the detector is estimated from the charged particle density in central Pb–Pb collisions at the top LHC energy. This determines the occupancy per layer and in the individual channels of the detector. A relevant contribution to the hit density in a given layer comes from secondary particles, which are mostly produced in the interaction of other particles with the material of the beam pipe and of the inner layers.

The charged particle density in central Pb–Pb collisions at $\sqrt{s_{NN}} = 5.5$ TeV is estimated by extrapolating the measured charged particle density in central Pb–Pb collisions at $\sqrt{s_{NN}} = 2.76$ TeV using the $s_{NN}^{0.15}$ scaling [29] which gives $dN_{ch}/d\eta \simeq 1970$. The hit density of the primary and secondary charged particles has been estimated by a Monte Carlo simulation for central Pb–Pb collisions, using the HIJING generator[30] tuned to such a charged particle multiplicity.

The particle load includes an additional contribution from the electromagnetic interactions of the colliding ions, among which the dominant process in terms of cross

4.2 Experimental conditions (ALICE Run 3) for simulation studies

section is the multiple e^+e^- pair production (QED electrons) [31, 32].

$$AA \rightarrow AA + n(e^+e^-) \quad (4.1)$$

where n is the pair multiplicity.

The flux of these electrons through the detectors which are close to the beam pipe can be rather high [33] and would have to be considered for occupancy studies. The flux of QED electrons was estimated by a Monte Carlo generator [34] implemented in the ALICE software framework [35]. Since the cross section of single pair production (about 220 kb) is about 98% of the total cross section, only single e^+e^- pairs are considered. The mean cluster rate for each layer of the upgraded ITS are estimated. The QED electrons per unit area per event are then calculated.

An example calculation using the first layer is shown below. The parameters assumed are:

Pb-Pb interaction rate - 50 kHz ($\mathcal{L} = 6 \times 10^{27} \text{cm}^{-2} \text{s}^{-1}$)

Magnetic field - 0.2T

p_T range - $0.3 \times 10^{-3} < p_T < 1 \text{ GeV}/c$

Rapidity range - $|\eta| < 4$

Number of events - 100000

QED cross section, $\sigma_{QED} \approx 92.3 \times 10^{-21} \text{cm}^2$ (from the generator).

Number of clusters in L0 = 53258

For the first layer L0, the total area is given by length of the sensitive area and the L0 radius.

Length of L0 (sensitive area) = 27.1 cm

L0 radius = 2.34 cm

Sensitive area of L0 = 432.85cm^2

4. DETECTOR PERFORMANCE

Table 4.1: Expected hit densities in central Pb–Pb collisions (including secondaries produced in the materials) and QED electrons for an integration time of 10 μ s. Interaction rates of 50 kHz and a 0.5 T (0.2 T) magnetic field have been assumed. The two columns on the right show the expected radiation levels.

Radius (cm)	Particle flux			Radiation Dose	
	Primary and secondary particles per event (cm^{-2})	QED electrons ($p_T > 0.3$ MeV) for $\tau=10$ μ s (cm^{-2})		NIEL (1 MeV $n_{eq}\text{cm}^{-2}$)	TID (krad)
		0.2 T	0.5 T		
2.34	20.5	6.82 ± 0.08	4.27 ± 0.05	9.2×10^{12}	646
3.15	14.6	3.81 ± 0.05	2.09 ± 0.03	6.0×10^{12}	380
3.93	11.1	2.44 ± 0.04	1.12 ± 0.02	3.8×10^{12}	216
19.61	0.71	$(2.1 \pm 0.1) \times 10^{-2}$	$(3.7 \pm 0.3) \times 10^{-3}$	5.4×10^{11}	15
24.55	0.51	$(9.0 \pm 0.5) \times 10^{-3}$	$(1.6 \pm 0.2) \times 10^{-3}$	5.0×10^{11}	10
34.39	0.24	$(1.3 \pm 0.1) \times 10^{-3}$	$(2.6 \pm 0.5) \times 10^{-4}$	4.8×10^{11}	8
39.34	0.20	$(5.0 \pm 0.6) \times 10^{-4}$	$(2.0 \pm 0.5) \times 10^{-4}$	4.6×10^{11}	6

For an integration time of 10 μ s, the QED electrons per unit area per event for L0 is given by,

$$\frac{6 \times 10^{27} \text{cm}^{-2} \text{s}^{-1} \times 92.3 \times 10^{-21} \text{cm}^2 \times 10^{-6} \text{s} \times 53258}{432.85 \text{cm}^2 \times 100000} \approx 6.82 \pm 0.08 \text{cm}^{-2}$$

The expected hit density for QED electrons for all the layers for a magnetic field of 0.5T and 0.2T are estimated and are given in Table 4.1. The QED electrons scale linearly with the detector integration time. The magnetic field of 0.2T corresponds to a planned run dedicated to the measurement of low-mass di-electrons, and is the worst case scenario in terms of detector occupancy. Table 4.1 also summarises the expected maximum hit densities for primaries and secondaries.

Table 4.1 also shows the expected radiation levels[6].

Detector acceptance: This study focuses on the central rapidity region and therefore the detector has been assumed to have a barrel geometry. The ITS acceptance has been determined based on its matching with the current external barrel detectors, as

discussed in section 4.3.

4.3 Detector specification

The specification for the Upgraded ITS is summarized here.

4.3.1 Number of layers and their radii:

4.3.1.1 Layout overview

The Upgraded ITS has a barrel geometry with seven layers consisting of monolithic pixels [6]. The radii, material budget of the detection layers and the detector intrinsic resolution are quoted in Table 4.2. The corresponding parameters of the present ITS are also added for comparison. The layers in the upgraded ITS are grouped into two separate barrels- the Inner Barrel (IB), containing the three innermost layers and the Outer Barrel (OB), with the four outermost layers. Fig.4.1 shows the layout (top panel) and the schematic view of the cross section (bottom panel) of the Upgraded ITS.

Each layer is segmented azimuthally in mechanically independent units called Staves. The Staves are fixed to a support structure to form Half-Layers. A Stave represent a complete detector element and consists of the following:

- Space Frame: a carbon fiber support structure for a single stave.
- Cold Plate: carbon ply to embed the cooling pipes.
- Hybrid Integrated Circuit: hosts the Flexible Printed Circuit (FPC) on which the pixel chips are bonded.
- Half-Stave: The Outer Barrel Stave is further segmented in azimuth in two halves called Half-Stave.
- Module: The Outer Barrel staves are also segmented longitudinally to Modules. Each Module consists of a Hybrid Integrated Circuit glued onto a carbon plate named as Module Plate.

The Staves for the Inner Barrel and the Outer Barel are illustrated in Fig.4.2.

4. DETECTOR PERFORMANCE

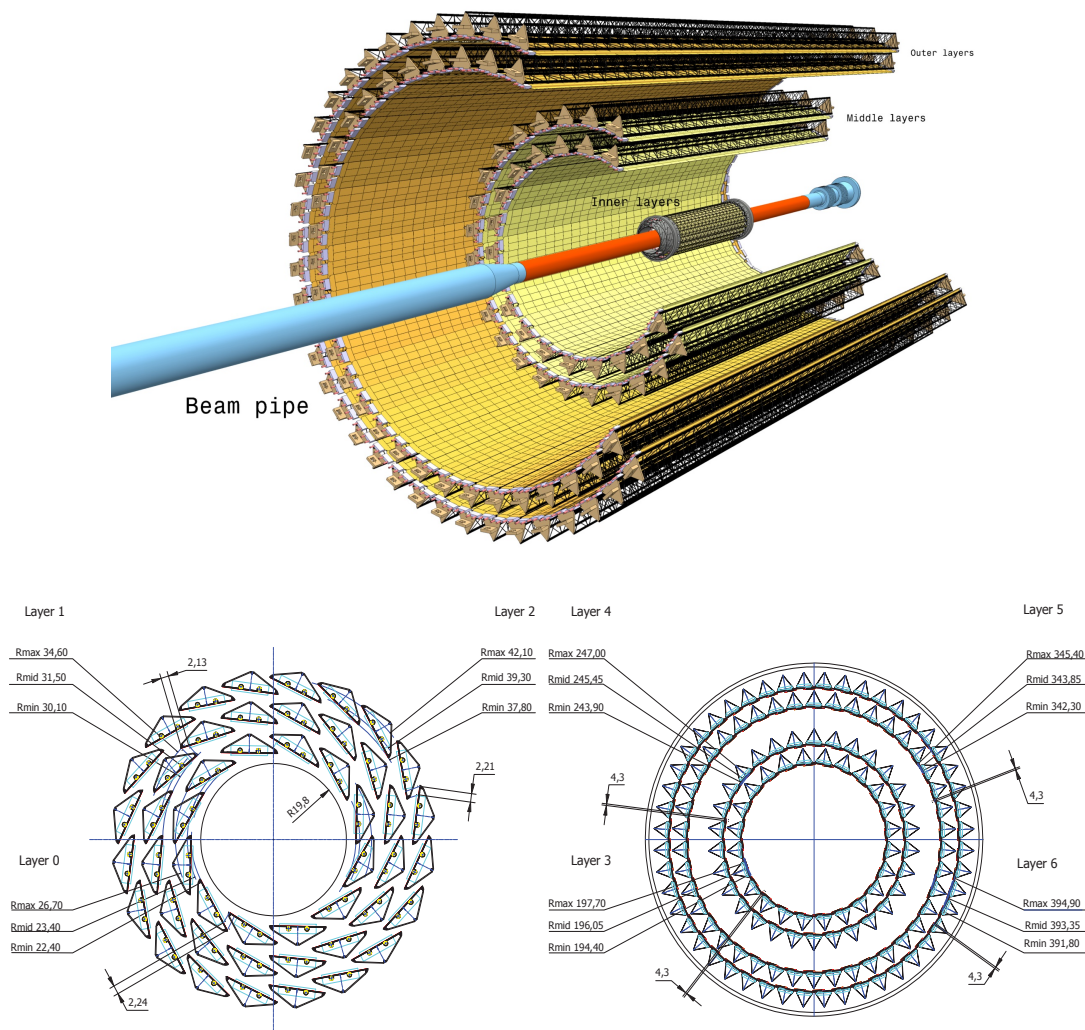


Figure 4.1: The top panel shows the layout of the Upgraded ITS [6]. The layer radii are optimized to provide improved tracking resolution. The first three layers (Inner Barrel) have the smallest possible radial distance from each other. To maximise the p_T resolution, the distance between the innermost and outermost layers should be as large as possible. The lower panel shows the schematic view of the cross section of the Inner Barrel (left) and the Outer Barrel (right).

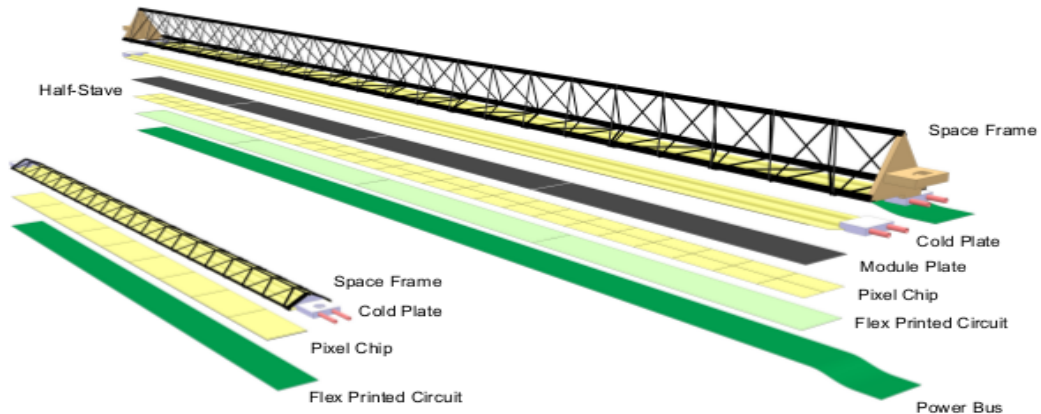


Figure 4.2: Illustration of Inner Barrel (left) and the Outer Barrel (right) Staves of the Upgraded ITS [6].

4.3.1.2 Layer radii optimization

The optimization of the radial positions of the layers is based on the objectives as listed below.

- Good tracking efficiency and p_T resolution for both tracking modes: ITS stand-alone and combined ITS+TPC:

Historically, ALICE performs two kinds of track-finding in the ITS: ITS combined with TPC and ITS standalone. In the case of ITS combined with TPC track-finding, the tracks found in the TPC are used as seeds to find their prolongation in the ITS using a Kalman filter approach [36, 37]. The acceptance in the TPC drops sharply below $p_T \approx 100 \text{ MeV}/c$, where the stand-alone ITS tracking comes into play. In this case, the ITS clusters not attached to TPC+ITS matched tracks are associated with tracks started from helical seeds constructed out of the primary vertex and two points taken from the two innermost pixel layers of the ITS.

Thus, a high ITS stand-alone tracking efficiency allows the reconstruction of low- p_T particles that cannot be reconstructed by the TPC, for example, low-mass di-electrons and the mesons D^+ and D_s^+ . At high p_T , the stand-alone ITS tracking can also reconstruct tracks that cross the TPC in the dead area between sectors, or close to it, where the TPC tracking performance degrades. A high ITS stand-alone tracking efficiency provides more robustness to the global tracking for the

4. DETECTOR PERFORMANCE

reconstruction of events with high pileup in the TPC and large distortions of its electric field. The availability of an independent ITS track reconstruction which is efficient in a large momentum range, allows for the evaluation of the overall ALICE tracking efficiency, as well as other systematic effects in the reconstruction, in a data-driven way.

- Good impact parameter resolution for track extrapolation towards the vertex:
The impact parameter resolution is mainly determined by the measurements of the track position in the two innermost layers, preferably having the first layer as close as possible to the beam line. To ensure that the impact parameter resolution of a track does not strongly deteriorate if one of the points close to the primary vertex is not attached to it, the first three layers (Inner Barrel) should have the smallest possible radial distance from each other. Such a layout is expected to be optimal for both ITS stand-alone and ITS+TPC combined tracking modes. In order to maximise the p_T resolution, the distance between the innermost and outermost layers should be as large as possible. This is reinforced by the fact that the matching with the TPC tracks profits from a small extrapolation distance between the TPC inner wall and the ITS outermost layer.
- Provide some redundancy against failures of detector modules.

4.3.2 Material budget:

With the recent developments in MAPS, the fabrication of thin sensors are possible which contributes to the reduction of material budget. The mechanical support, power distribution, cooling system and read-out system can also be optimized for a lower material budget. In the simulations described in the section 4.5, an effective material budget of 0.3 % and 0.8 % of the radiation length was assumed for the three inner layers (Inner Barrel) and the four outer layers (Outer Barrel) respectively.

4.3.3 Detector intrinsic resolution:

The segmentation of the detector determines the intrinsic spatial resolution of the reconstructed track points. A small segmentation is also important to keep the occupancy at a low value. An excellent resolution of the first layer is fundamental for the impact

4.3 Detector specification

Table 4.2: Specifications of the Upgraded ITS in terms of layers radii, intrinsic resolution and material budget. Specifications of the present ITS is also shown for comparison. The upgraded beam pipe will be narrower than the present one.

Detector	Layer	Radius r (cm)	Intrinsic resolution ($r\phi, z$) μm	Material Budget $X/X_0\%$
Upgraded ITS	L0	2.34	(5,5)	0.3
	L1	3.15	(5,5)	0.3
	L2	3.93	(5,5)	0.3
	L3	19.61	(5,5)	0.8
	L4	24.55	(5,5)	0.8
	L5	34.39	(5,5)	0.8
	L6	39.34	(5,5)	0.8
	Beam pipe	1.98		0.22
Present ITS	SPD	3.9	(12,100)	1.14
	SPD	7.6	(12,100)	1.14
	Th. shield	11.5		0.65
	SDD	15.0	(35,25)	1.13
	SDD	23.9	(35,25)	1.26
	Th. shield	31.0		0.65
	SSD	38.0	(20,830)	0.83
	SSD	43.0	(20,830)	0.83
		Beam pipe	2.9	

parameter resolution at high particle momenta where the multiple scattering effects become negligible. For the outer layers, a good resolution is also important to improve the momentum resolution and the tracking efficiency in the ITS stand-alone mode. The simulation studies assume an intrinsic spatial resolution of $5\ \mu\text{m}$ for the all the layers in both $r\phi$ and z directions for the baseline ITS Upgrade configuration.

4.3.4 Acceptance:

The ITS acceptance is defined by taking into account its matching with the other external barrel detectors in ALICE: TPC, TRD, TOF and EMCAL. The acceptance of the TPC corresponds to $|\eta| < 0.92$ for tracks traversing its full radial extension. The

4. DETECTOR PERFORMANCE

TRD and TOF have the same acceptance as the TPC ($|\eta| < 0.92$), while the EMCAL acceptance is smaller. The TPC can also efficiently reconstruct tracks traversing half of its radial extension, extending its acceptance to $|\eta| < 1.22$. In Pb–Pb interactions at $\sqrt{s_{NN}} = 5.5$ TeV the luminous region would spread around the nominal IP with a longitudinal Gaussian distribution with $\sigma_z^{\text{lumi}} = 5.61$ cm [38]. The longitudinal length of each ITS layer is defined to accept all tracks within a given η range from this luminous region. The Upgraded ITS would accept tracks with $|\eta| < 1.22$ coming from the 90% most luminous region ($|z_{vtx}| < 1.39\sigma_z^{\text{lumi}}$).

4.3.5 Timing and readout rate:

The interaction rates during ALICE Run 3 will be 200 kHz for pp and 50 kHz for Pb–Pb collisions. These rates may induce a significant pile-up rate in the detector, depending on the integration time, which has an impact on event reconstruction and analysis. If the total occupancy from triggered and pile-up interactions significantly exceeds the occupancy of a central Pb–Pb collision, the reconstruction efficiency drops due to the ambiguity of the cluster to track association. With 50 kHz interaction rate and $20\mu\text{s}$ ($30\mu\text{s}$) integration time window, on average about one (two) extra Pb–Pb collision will be read-out on top of the triggered event. In about 10% of the triggers five or more extra collisions will be piled up assuming an integration time window of $30\mu\text{s}$. To prevent significant losses of the reconstruction efficiency, especially at low p_T , the time resolution in the highest occupancy layers should not exceed about $20\mu\text{s}$. A similar time resolution is desirable also for the outer layers in order to facilitate the cluster matching throughout the whole detector.

4.4 Simulation tools

A Fast Estimation Tool (FET) is used to study the performance of the Upgraded ITS. This is a semi-analytic method and provides an excellent determination of the tracking resolution (both for spatial and the momentum components) as a function of detector configuration. The results of the FET have been confirmed (within about 5% accu-

racy) by the study with a Monte Carlo (MC) based on transport code and a detailed description of the geometry.

The FET is based on a code originally developed by the STAR HFT collaboration [39]. It permits to model a simplified description of the detector layout with cylindrical layers. The detector performance can be studied and optimized by defining the properties of the detector layers: radius, material budget and the intrinsic detector resolution in $r - \phi$ and z components. This tool adopts a tracking method as described in [36]. The original STAR HFT code was extended and adapted in various ways, e.g. to describe also the ITS upgrade stand-alone tracking capabilities. The tracking code was replaced with the Kalman filter technique [36], [37], which is implemented in the ALICE software framework [35]. The intrinsic (or cluster) resolution of a layer and the traversed material depend on the detector segmentation and the inclination angle of the charged particle with respect to the layer normal. This is taken into account by calculating the track-parameter covariance matrix elements at the various stages of the track reconstruction. A detailed description of the method and its extensions can be found in [40].

4.5 Detector performance studies

4.5.1 Comparison with the current ALICE ITS

In this section, the performance of the Upgraded ITS is compared with the current ITS with respect to impact parameter resolution, pointing resolution, momentum resolution and tracking efficiency. Table 4.2 shows the properties of the Upgraded and the current ITS.

4.5.1.1 Impact parameter resolution

The impact parameter resolution defines the capability of a vertex detector to separate secondary vertices of heavy-flavour decays from the main interaction vertex (primary vertex). It is defined as the dispersion of the distribution of the Distance of Closest Approach (DCA) between reconstructed (primary) tracks and the main collision vertex. Thus it is an important measure of the achieved tracking precision. Fig.4.3 shows the schematic view of the D_0 decay in the $D^0 \rightarrow K^- \pi^+$ channel. The impact parameter

4. DETECTOR PERFORMANCE

resolution is given by $\sigma_{d_K^0}$ (the resolution of d_K^0) and $\sigma_{d_\pi^0}$ (the resolution d_π^0) for kaon and pion respectively.

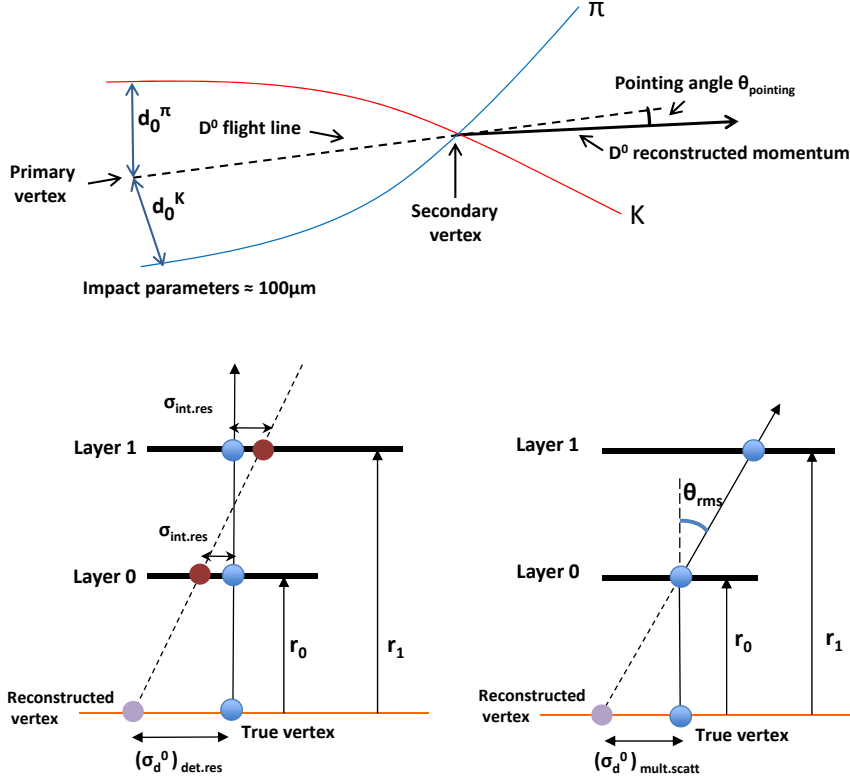


Figure 4.3: Schematic view of the D_0 decay in the $D^0 \rightarrow K^- \pi^+$ channel (top panel). The resolutions of the impact parameters d_K^0) and d_π^0 gives the impact parameter resolution $\sigma_{d_K^0}$ and $\sigma_{d_\pi^0}$ for kaon and pion respectively. The lower panel shows the contributions of detector resolution and coulomb scattering on the impact parameter resolution.

The impact parameter resolution has contributions from the detector intrinsic resolution and multiple coulomb scattering.

$$\sigma_{d^0} = (\sigma_{d^0})_{\text{det.res.}} \oplus (\sigma_{d^0})_{\text{mult.scattering}} \quad (4.2)$$

The bottom panel of the Fig.4.3 shows a scheme of the contributions of detector intrinsic resolution (left) and multiple coulomb scattering (right) on the impact parameter. The first term on the right hand side of Equation 4.2, $(\sigma_{d^0})_{\text{det.res.}}$ is independent of the momentum of the traversing particle. It depends only on the intrinsic resolution

and the radial position of the detector. From the bottom left panel of Fig.4.3,

$$(\sigma_{d^0})_{det.res.} = \sigma_{int.res.} \sqrt{\frac{(r_0^2 + r_1^2)}{(r_1 - r_0)^2}} \quad (4.3)$$

where r_0 and r_1 are the radii of the first layer and second layer of the vertex detector respectively and $\sigma_{int.res.}$ is the detector intrinsic resolution.

The second term on the right hand side of the Equation 4.2 depends on the momentum and on the amount of material crossed by the particle. A charged particle suffers from Multiple Coulomb Scattering when it traverses through the material of the tracking detector. This results in small deviations of the track due to successive small angle deflections symmetrically distributed around the incident direction [20]. The scattering angle follows roughly a Gaussian distribution with an rms of,

$$\theta_{rms} = \frac{13.6 \text{ MeV}}{\beta.p.c} .z. \sqrt{\frac{X}{X_0}} [1 + 0.038 \ln(\frac{X}{X_0})] \quad (4.4)$$

where β , p and z are the velocity, momentum and charge of the particle respectively. The detector material thickness through which the particle traversed is represented by X and X_0 is the radiation length for the scattering medium. The ratio X/X_0 represents the material budget. One has,

$$(\sigma_{d^0})_{mult.scattering} = \theta_{rms}.r_0 \quad (4.5)$$

Thus the impact parameter resolution can be expressed as:

$$\sigma_{d^0} = \sigma_{int.res.} \sqrt{\frac{(r_0^2 + r_1^2)}{(r_1 - r_0)^2}} \oplus r_0 . \frac{13.6 \text{ MeV}}{\beta.p.c} .z. \sqrt{\frac{X}{X_0}} [1 + 0.038 \ln(\frac{X}{X_0})] \quad (4.6)$$

For a particle moving in the transverse plane, considering the material thickness and the layer radii constant, the above expression can be written in the form:

$$\sigma_{d^0} = A \oplus \frac{B}{p_T} \quad (4.7)$$

where A depends on the detector intrinsic resolution and B depends on the material budget.

Thus, the impact parameter resolution depends on the detector intrinsic resolution, material budget and the radial positions of the first two detector layers.

4. DETECTOR PERFORMANCE

Qualitatively, the impact parameter resolution in $r - \phi$, can also be represented as the convolution of the primary vertex resolution and the track pointing resolution.

$$\sigma_{d^0} = \sigma_{vertex} \oplus \sigma_{pointing} \quad (4.8)$$

For Pb–Pb collisions the uncertainty on the primary vertex position, whose determination is based on a large number of reconstructed tracks, is negligible with respect to that of the track spatial position, and therefore the d^0 resolution coincides with the track pointing resolution.

$$\sigma_{d^0} \approx \sigma_{pointing} \quad (4.9)$$

Fig. 4.4 shows a comparison of the impact parameter resolution (top panels) and pointing resolution (bottom panels) between the present and upgraded ITS. The left and right panels show the resolution in $r - \phi$ and z .

At p_T around 0.4 GeV/ c , the improvement in the pointing resolution in $r - \phi$ of the upgraded ITS is about a factor 3 over the present ITS. In z , the gain in resolution is even higher, reaching a factor of about 5 at p_T around 0.4 GeV/ c .

Since the impact-parameter resolution depends mainly on the radial position, thickness, and granularity of the innermost layer(s), it is essentially identical for both combined TPC+ITS and ITS stand-alone tracking modes.

4.5.1.2 Momentum resolution

Figure 4.5 shows the momentum resolution (σ_{p_T}/p_T) comparison between the Upgraded ITS and the current ITS, obtained in the combined TPC+ITS and ITS stand-alone tracking modes. The upgraded ITS yields a dramatic improvement in the stand-alone tracking mode. The p_T resolution in the stand-alone mode benefits significantly from the improved intrinsic resolution and the overall low material budget of the upgraded ITS which reduces the effects of multiple scattering.

In the ITS+TPC combined tracking mode, at p_T below 0.5 GeV/ c , the Upgraded ITS has an improved resolution with respect to the current performance due to the reduction of the material budget of the innermost layers.

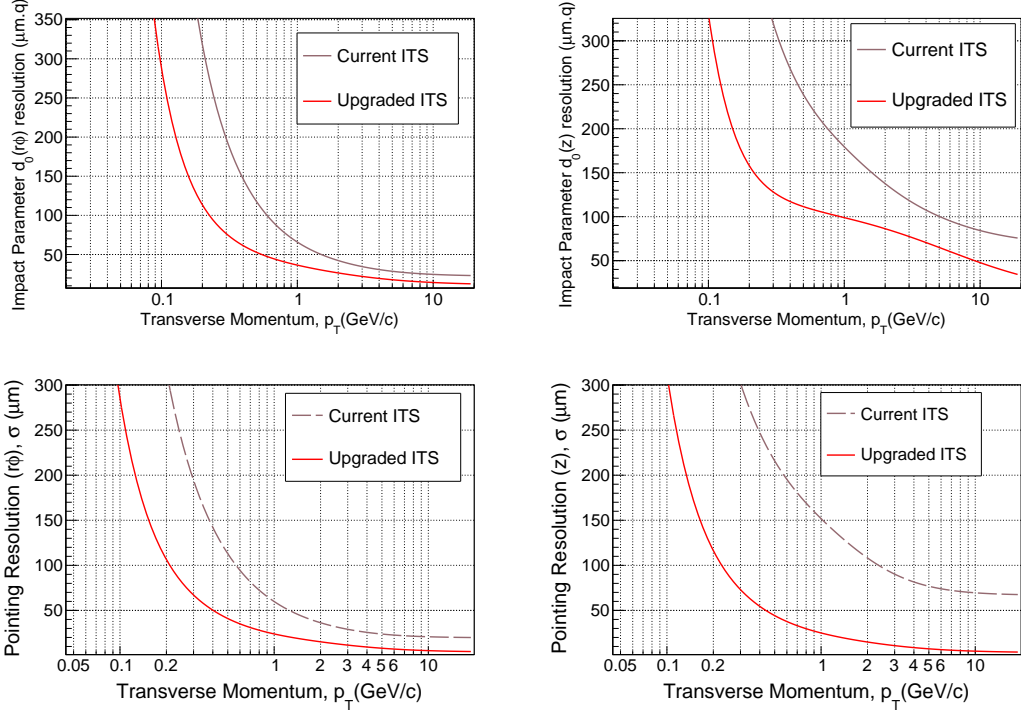


Figure 4.4: Impact-parameter resolution (top) and pointing resolution (bottom) for primary charged pions as a function of the transverse momentum for the current ITS and the upgraded ITS in the transverse plane, $r - \phi$ (left panel) and in the longitudinal direction, z (right panel).

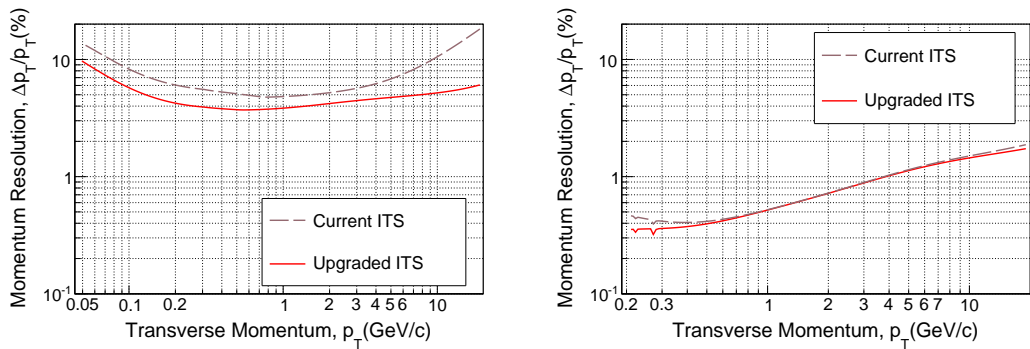


Figure 4.5: Transverse momentum resolution as a function of p_T for primary charged pions for the upgraded ITS. The results for the ITS stand-alone (left) and ITS-TPC combined tracking mode (right) are shown.

4. DETECTOR PERFORMANCE

4.5.1.3 Tracking efficiency

The tracking efficiency for the Upgraded ITS is defined as the ratio of the number of reconstructed tracks with at least four correct clusters associated to the tracks and no wrongly associated cluster (from other particles) to the number of “trackable” tracks (i.e. tracks passing through at least four layers). The baseline configuration of the Upgraded ITS assumes a layer detection efficiency of 95% for all layers. The tracking efficiency as a function of p_T is shown in Figure 4.6 for the current ITS and the Upgraded ITS in both stand-alone and combined ITS+TPC tracking mode. There is an impressive improvement of the tracking efficiency for tracks with $p_T < 1 \text{ GeV}/c$ and lower.

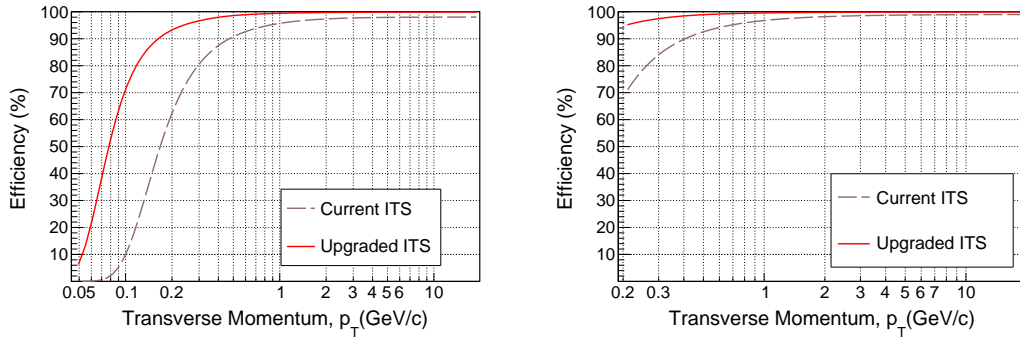


Figure 4.6: Track-matching efficiency between the TPC and upgraded ITS for primary charged pions.

4.5.2 Performance for improved or degraded sensor parameters

This section describes the performance studies of some alternative configurations of the Upgraded ITS and their comparison with the baseline upgrade configuration. The baseline upgrade configuration features seven layers of monolithic pixels with an intrinsic resolution of $(5 \mu\text{m}, 5 \mu\text{m})$ in $r - \phi$ and z respectively and a total material budget per layer of $0.3\% X_0$ and $0.8\% X_0$ for the inner and outer barrel respectively. There is a possibility that, based on the ongoing studies, some of the detector specifications specially in the outer barrel may still evolve. To evaluate such a scenerio, some alternative configurations with variations in the key parameters: intrinsic resolution and material budget of the detection layers, are studied and compared with the baseline configuration.

4.5.2.1 Performance with variations in the sensor intrinsic resolution

The detector performance is studied with the variation of intrinsic resolution, particularly for the following configurations. The material budget is fixed to $X/X_0 = 0.3\%$ and $X/X_0 = 0.8\%$ for the inner and outer barrel respectively.

- an intrinsic resolution of $(4\ \mu\text{m}, 4\ \mu\text{m})$ for all layers in $r - \phi$ and z (baseline configuration);
- an intrinsic resolution of $(5\ \mu\text{m}, 5\ \mu\text{m})$ for all layers in $r - \phi$ and z ;
- an intrinsic resolution of $(7\ \mu\text{m}, 7\ \mu\text{m})$ for all layers in $r - \phi$ and z ;
- an intrinsic resolution of $(9\ \mu\text{m}, 9\ \mu\text{m})$ for all layers in $r - \phi$ and z ;
- an intrinsic resolution of $(5\ \mu\text{m}, 5\ \mu\text{m})$ in $r - \phi$ and z and $(9\ \mu\text{m}, 9\ \mu\text{m})$ in $r - \phi$ and z for the inner and outer barrel respectively;
- an intrinsic resolution of $(5\ \mu\text{m}, 5\ \mu\text{m})$ in $r - \phi$ and z and $(12\ \mu\text{m}, 12\ \mu\text{m})$ in $r - \phi$ and z for the inner and outer barrel respectively;

The design goal of the ITS upgrade is to have pixels with the same granularity for all the layers. The last two configurations mentioned above are considered to study a scenario where the outer barrel has pixels with lower granularity as a consequence of increased pixel size. This situation may arise if there is a need to decrease the power density in the outer barrel.

Fig. 4.7 shows the pointing resolution in the bending ($r - \phi$) and longitudinal (z) direction for ITS standalone tracking and ITS-TPC combined tracking for detector configurations with different intrinsic resolution. For the standalone ITS tracking, the pointing resolution in $(r - \phi)$ remains unaffected at $p_T < 0.2\ \text{GeV}/c$. The configuration with an intrinsic resolution of $(7\ \mu\text{m}, 7\ \mu\text{m})$ and $(9\ \mu\text{m}, 9\ \mu\text{m})$ for all layers starts to deteriorate at $p_T > 0.2\ \text{GeV}/c$. At $p_T = 0.8\ \text{GeV}/c$, the former deteriorates by a factor of about 1.2 and the latter deteriorates by a factor of 1.3 from the baseline configuration. The pointing resolution for the other configurations are not affected by variations of the intrinsic resolution in the range considered for these simulations. The pointing resolution in z shows a similar behavior.

4. DETECTOR PERFORMANCE

For the ITS-TPC combined tracking, the configuration with an intrinsic resolution of $(7\ \mu\text{m}, 7\ \mu\text{m})$ and $(9\ \mu\text{m}, 9\ \mu\text{m})$ for all layers suffers a slight deterioration of the pointing resolution throughout the range considered for these simulations.

In Fig. 4.8, the top panel shows the momentum resolution. The bottom panels show the tracking efficiency. The left and the right panels show the ITS stand-alone and the ITS-TPC combined tracking, respectively. The tracking efficiency is hardly affected by the variation of the intrinsic resolution. The momentum resolution is unaffected by the variation in the intrinsic resolution at $p_T < 0.3\ \text{GeV}/c$. The relative transverse momentum resolution is in the range 3.7% to 4.5% for $0.3\ \text{GeV}/c < p_T < 2\ \text{GeV}/c$, in particular, the configurations with an intrinsic resolution of $(7\ \mu\text{m}, 7\ \mu\text{m})$ and $(9\ \mu\text{m}, 9\ \mu\text{m})$ are affected. For $p_T > 2\ \text{GeV}/c$, the configuration with intrinsic resolution of $(5\ \mu\text{m}, 5\ \mu\text{m})$ and $(12\ \mu\text{m}, 12\ \mu\text{m})$ for the inner and outer barrel respectively, also starts to deteriorate.

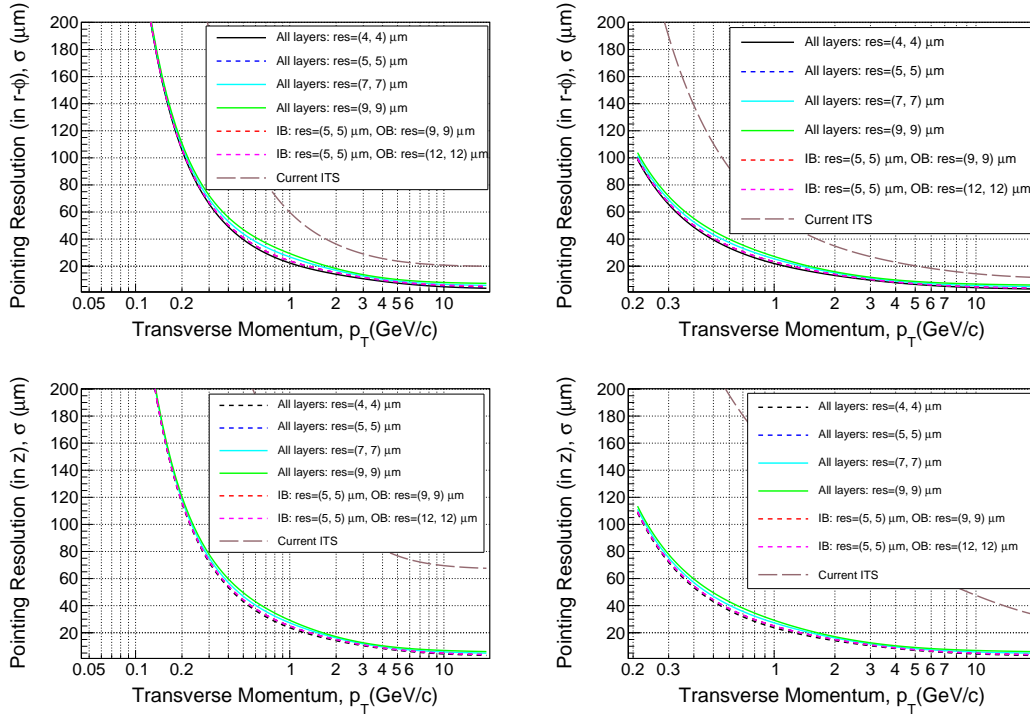


Figure 4.7: Pointing resolution as a function of p_T for detector configurations with varying intrinsic resolutions compared to the baseline upgrade configuration. The current ITS configuration is also included. Left and right panels show the ITS stand-alone and the ITS-TPC combined tracking, respectively.

The momentum resolutions for the ITS-TPC combined tracking is almost unaffected by the variation of the intrinsic resolution.

This study shows that a relaxation of the intrinsic resolution for all the layers would result in a deterioration of the detector performance. On the other hand, the effects on the detector performance would be in the acceptable limits if the intrinsic resolution is relaxed only for the outer barrel to (9 μm , 9 μm) and maintaining that of the inner barrel to (5 μm , 5 μm).

4.5.2.2 Performance with variations in the material budget

The variation of the detector performance with varying material budget is studied. In particular, the following configurations are considered. The intrinsic resolution is fixed to (5 μm , 5 μm) in $r - \phi$ and z respectively for all the layers.

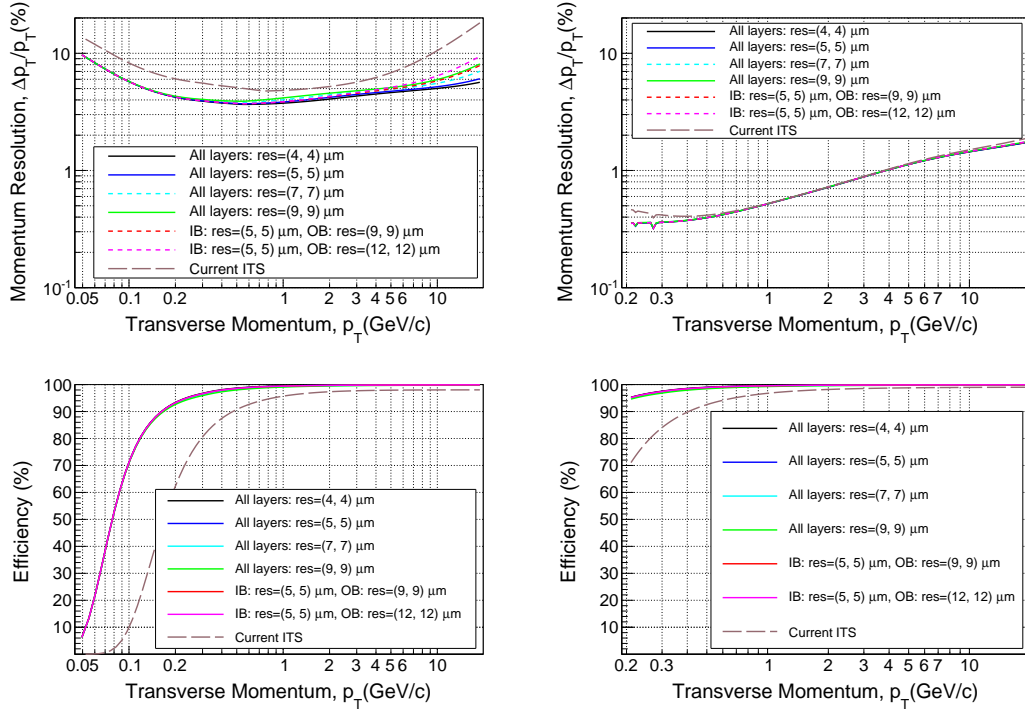


Figure 4.8: Momentum resolution (top panels) and tracking efficiency (bottom panels) as a function of p_T for detector configurations with varying intrinsic resolutions compared to the baseline upgrade configuration. The current ITS configuration is also included. Left and right panels show the ITS stand-alone and the ITS-TPC combined tracking, respectively.

4. DETECTOR PERFORMANCE

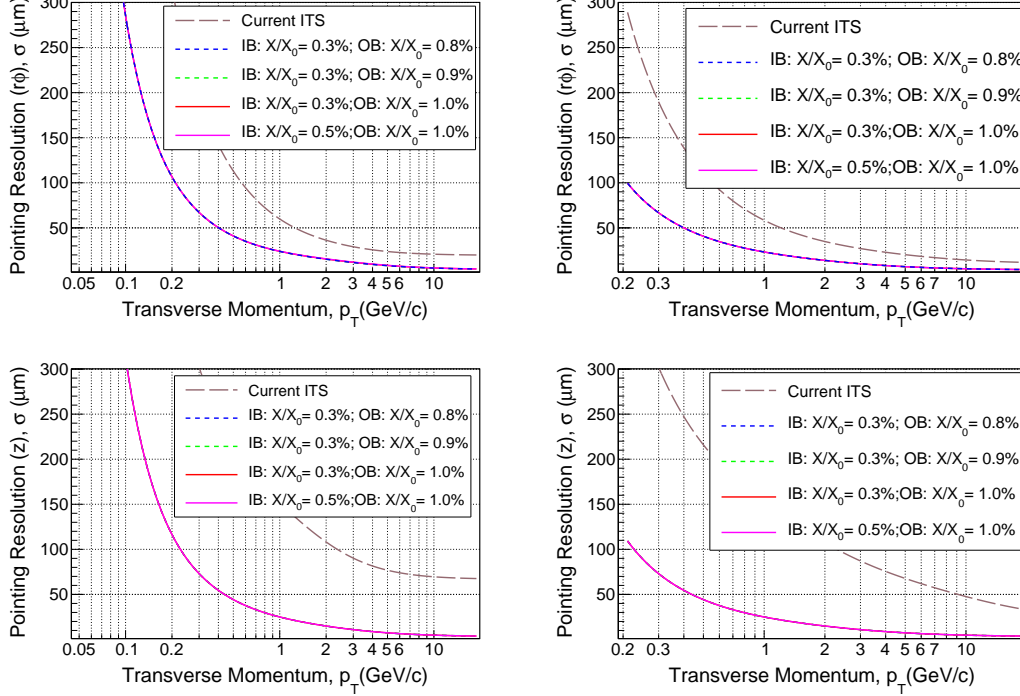


Figure 4.9: Pointing resolution as a function of p_T for detector configurations with varying material budget compared to the baseline upgrade configuration. The current ITS configuration is also included. Left and right panels show the ITS stand-alone and the ITS-TPC combined tracking, respectively.

- the inner and outer barrel having a material budget of $X/X_0 = 0.3\%$ and $X/X_0 = 0.8\%$ respectively;
- the inner and outer barrel having a material budget of $X/X_0 = 0.3\%$ and $X/X_0 = 0.9\%$ respectively (more recent value for the baseline configuration);
- the inner and outer barrel having a material budget of $X/X_0 = 0.3\%$ and $X/X_0 = 1.0\%$ respectively;
- all layers of the inner and outer barrel presenting a larger material budget of $X/X_0 = 0.5\%$ and $X/X_0 = 1.0\%$ respectively.

The first configuration mentioned above represents the baseline configuration. In the next two configurations, the material budget for the inner barrel has been assumed to remain the same as the baseline configuration ($X/X_0 = 0.3\%$) while the material

budget for the outer barrel is varied. The fourth configuration assumes a larger material budget for all the layers.

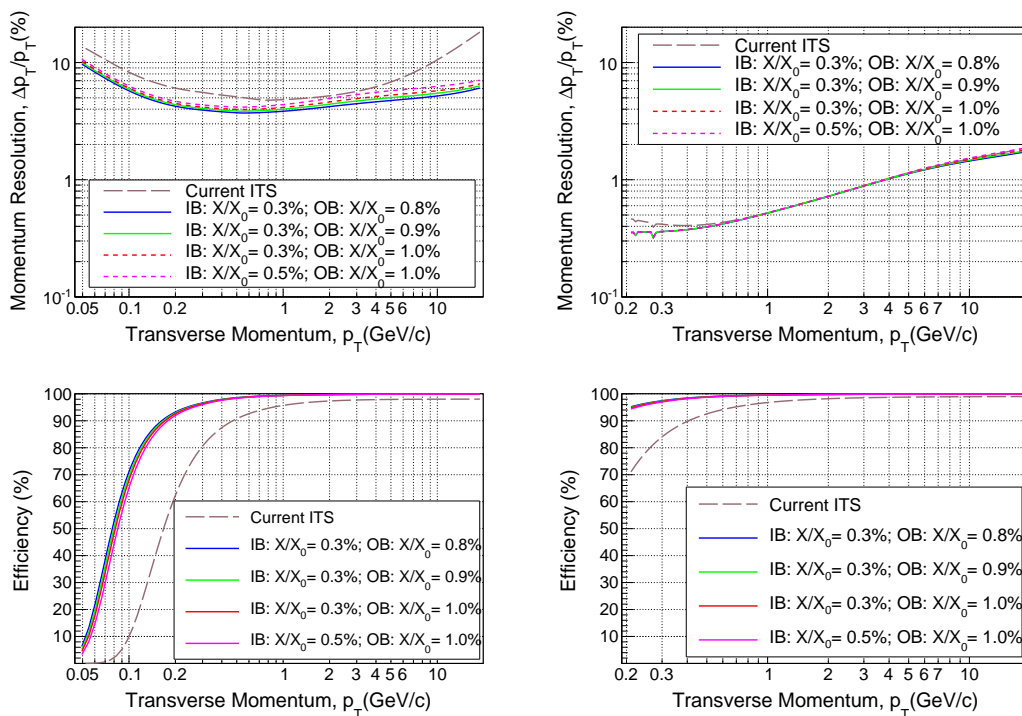


Figure 4.10: Momentum resolution as a function of p_T for detector configurations with varying material budget compared to the baseline upgrade configuration. The current ITS configuration is also included. Left and right panels show the ITS stand-alone and the ITS-TPC combined tracking, respectively.

Fig. 4.9 shows the pointing resolution in the bending ($r - \phi$) and longitudinal (z) direction for ITS standalone tracking and ITS-TPC combined tracking for detector configurations with varying material budget.

The pointing resolution is unaffected by the variations of material budget for the ITS standalone and ITS-TPC combined tracking.

In Fig. 4.10 the top panel shows the momentum resolution. The bottom panels show the tracking efficiency. The left and the right panels show the ITS stand-alone and the ITS-TPC combined tracking, respectively. The stand-alone tracking efficiency and momentum resolution are slightly affected by the increase of the material budget of the Outer Barrel. At $p_T = 0.2$ GeV/c, the tracking efficiency is in the range 92% to

4. DETECTOR PERFORMANCE

94%. The relative transverse momentum resolution is in the range 3.9% to 4.5% for $200 \text{ GeV}/c < p_T < 1 \text{ GeV}/c$.

The momentum resolutions for the ITS-TPC combined tracking is slightly affected only at high p_T .

This study shows that the increase of material budget in the Outer Barrel to $1.0\%X_0$, could be acceptable as this does not affect the pointing resolution and affects the momentum resolution only slightly.

4.5.3 Performance with a further reduction of beam pipe radius

As mentioned in Section 4.2, the baseline scenario for the ALICE upgrade includes the installation of a new beam pipe with an inner radius of 1.9 cm (average radius of 1.94 cm, considering a thickness of 0.8 cm). Studies show that it is possible to further reduce the beam pipe radius down to 1.72 cm (average radius of 1.76 cm). This section studies a scenerio with a reduced average beam pipe radius of 1.76 cm and evaluate if there is a significant improvement in performance with respect to the baseline upgrade scenerio. In this configuration, the Inner Barrel also has a reduced radii (L0:2.136 cm, L1:2.863 cm, L2:3.59 cm) but the Outer Barrel radii remains the same as in the baseline upgrade configuration. A second configuration is also studied where the average beam pipe radius is reduced to an intermediate value of 1.86 cm, keeping the Inner Barrel and Outer Barrel radii same as that of the baseline configuration.

Fig.4.11 shows the pointing resolution in $r - \phi$ (top panels) and z (bottom panels). The left and right panels show the ITS stand-alone and the ITS-TPC combined tracking, respectively. There is a marginal improvement at low p_T for an average beam pipe radius of 1.86 cm. The resolution shows further improvement with the reduction of both the average beam pipe radius (1.76 cm) and the Inner Barrel radii. The reduction of beam pipe radius does not translate to a significant gain in physics performance. Moreover, the reduced Inner Barrel radius would increase the occupancy resulting in a higher fake track rate. On the other hand, the reduction of the average beam pipe radius to 1.86 cm without changing the Inner Barrel radius could be useful from a mechanical point of view because the installation of the Inner Barrel could be easier.

This study concludes that a further reduction of beam pipe radius and the Inner Barrel radii does not give significant gain. Nevertheless, a reduction of the beam pipe

radius by 1 mm keeping the Inner Barrel radii at the baseline values could be considered to facilitate the installation of the Inner Barrel.

Fig. 4.12 shows the momentum resolution (top panels) and tracking efficiency (bottom panels) comparison with variation in the beam pipe radius. The left and right panels show ITS standalone tracking and ITS-TPC combined tracking respectively. The reduction of beam pipe radius does not affect the momentum resolution and tracking efficiency of the upgraded detector.

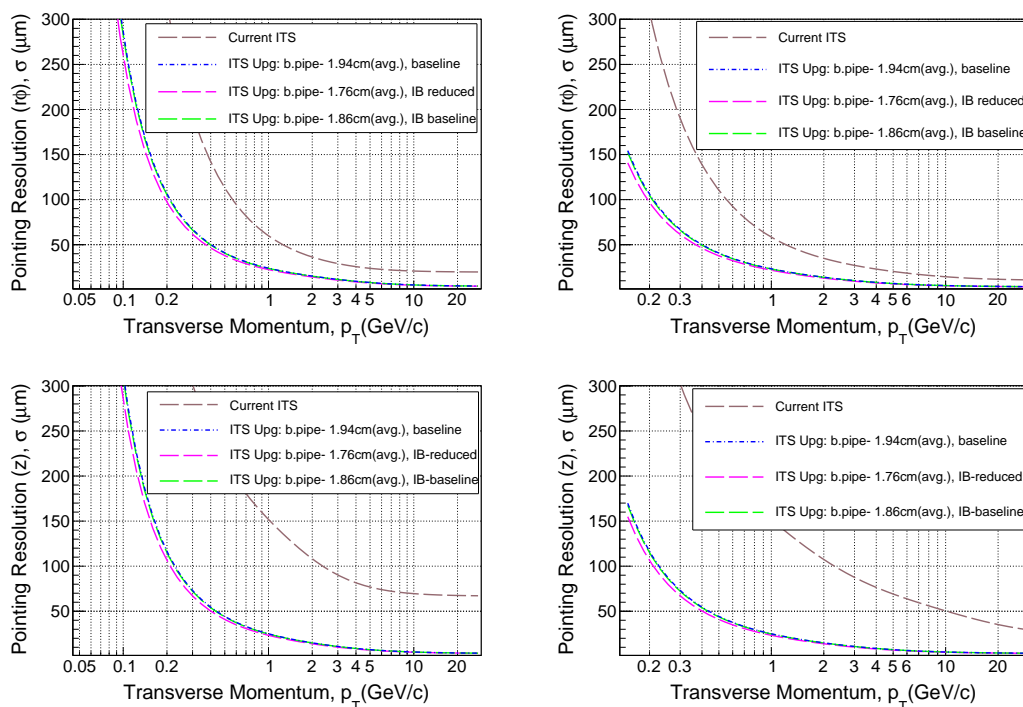


Figure 4.11: Pointing resolution as a function of p_T for detector configurations with varying beam pipe radius compared to the baseline upgrade configuration. The current ITS configuration is also included. Left and right panels show the ITS stand-alone and the ITS-TPC combined tracking, respectively.

4. DETECTOR PERFORMANCE

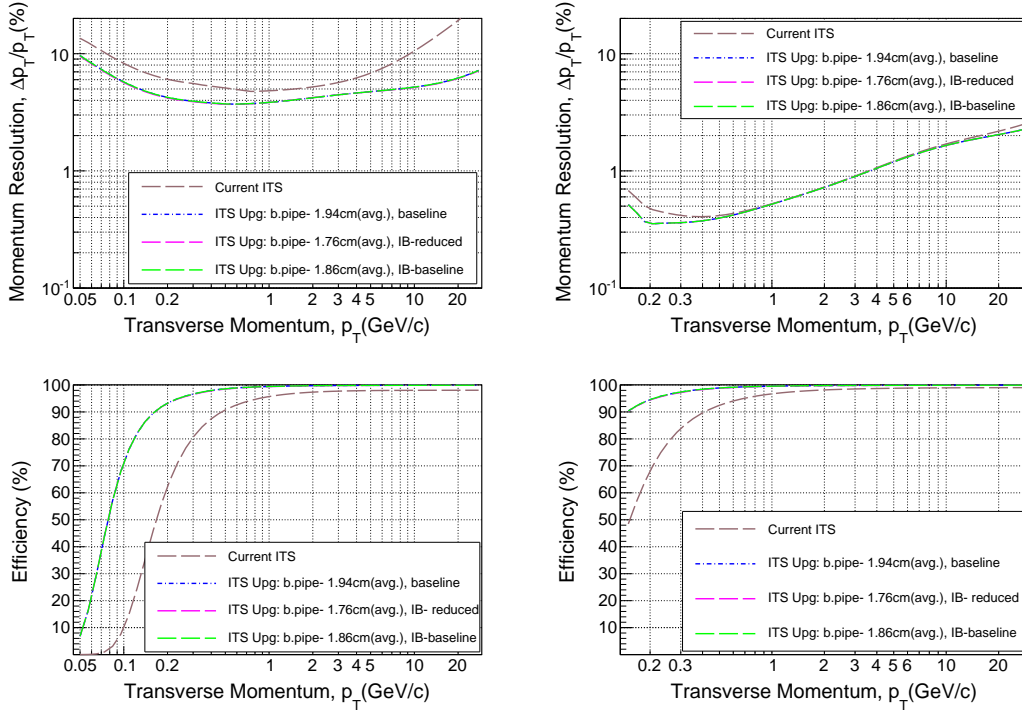


Figure 4.12: Momentum resolution (top panels) and tracking efficiency (bottom panels) as a function of p_T for detector configurations with varying beam pipe radius compared to the baseline upgrade configuration. The current ITS configuration is also included. Left and right panels show the ITS stand-alone and the ITS-TPC combined tracking, respectively.

4.5.4 Redundancy studies

This section investigates the effect of a dramatic reduction of detection efficiency on the detector performance. This reduction may be due to the effect of a dead layer or layers with reduced detection efficiency.

Fig. 4.13 shows the effect of a reduced overall detection efficiency of the layers on the global tracking efficiency. The reduced detection efficiency might be due to either limited acceptance and dead areas, or intrinsic inefficiency of the detector. The baseline configuration assumes a detection efficiency of 95% which is conservative, given the fact that typical values of detection efficiency for non dead zones of silicon detectors are around 99%. The case of having all the seven layers (at the same time) with an efficiency of 100%, 85%, 75% and 65% have been simulated and compared with the baseline configuration.

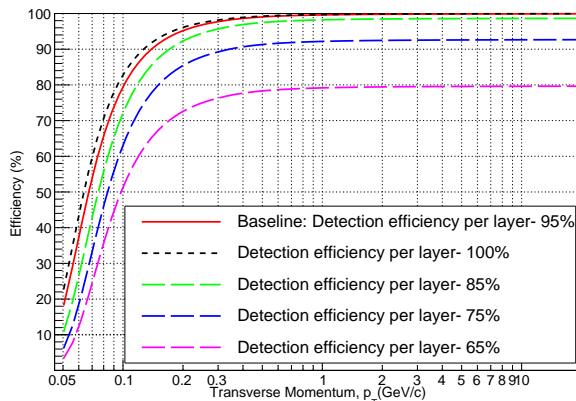


Figure 4.13: Tracking efficiency as a function of p_T for the upgraded ITS detector, assuming different reduced detection efficiency for all seven layers of the layout.

Figure 4.14 considers a case where one of the layers is completely dead. The left panel shows the effect of the absence of each of the seven layers (one at a time), on the ITS standalone tracking efficiency. The right panel extracts the two worst cases: the absence of the second (Layer 1) and the third layer (Layer 2) contribute the most to the reduction of the tracking efficiency.

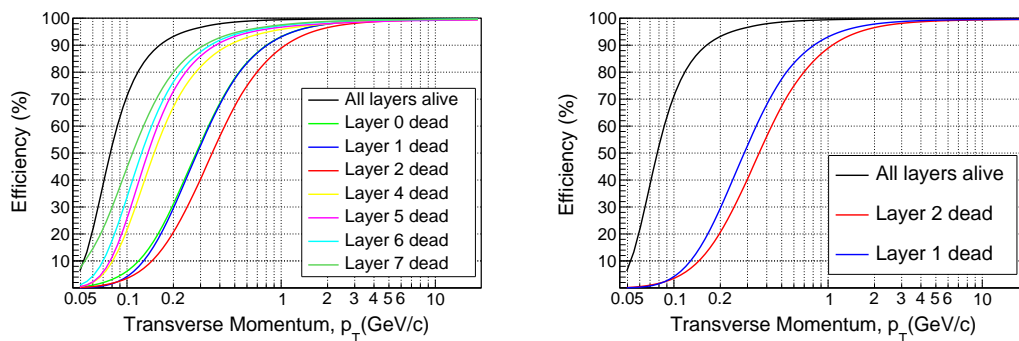


Figure 4.14: Tracking efficiency for the upgraded ITS in presence of a dead layer. The right panel shows two worst case scenarios for the tracking efficiency where layer 1 (blue) or layer 2 (red) is dead is compared to the case where all layers are properly working.

Figure 4.15 shows the performance in the presence of a dead layer with respect to the momentum resolution. In the standalone tracking mode, the two worst case scenarios are the absence of the third layer (Layer 2) and the seventh layer (Layer 6). The absence of the third layer contributes the most to the degradation of the momentum resolution

4. DETECTOR PERFORMANCE

at $p_T > 1 \text{ GeV}/c$. At $p_T < 1 \text{ GeV}/c$, the absence of the seventh layer is the worst case. The presence of dead layers does not have a significant effect on the momentum resolution for combined ITS and TPC tracking.

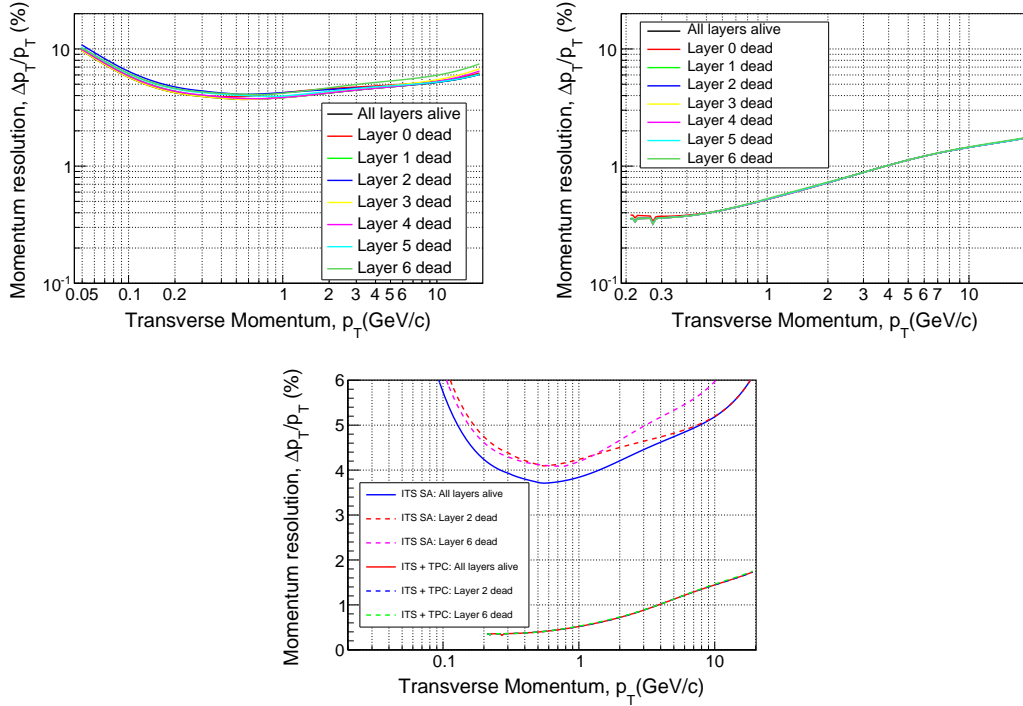


Figure 4.15: Momentum resolution for the upgraded ITS in the presence of dead layers. The top left panel and the top right panel considers the ITS standalone tracking and ITS plus TPC combined tracking respectively. The bottom panel shows the worst case scenarios for the momentum resolution which are compared to the case where all layers are properly working. The momentum resolution for combined ITS and TPC tracking stays practically unchanged.

Figure 4.16 shows the impact parameter resolution in the presence of a dead layer. The worst case scenerio is the absence of the first layer (Layer 0). The absence of the other layers does not affect the impact parameter resolution significantly.

This study shows that a dead layer in the Upgraded ITS would have significant effects on the detector performance with respect to tracking efficiency and resolution. This confirms that rapid accessibility to the detector is a key priority in the design of the upgraded ITS, which would enable prompt action in case such a situation arises.

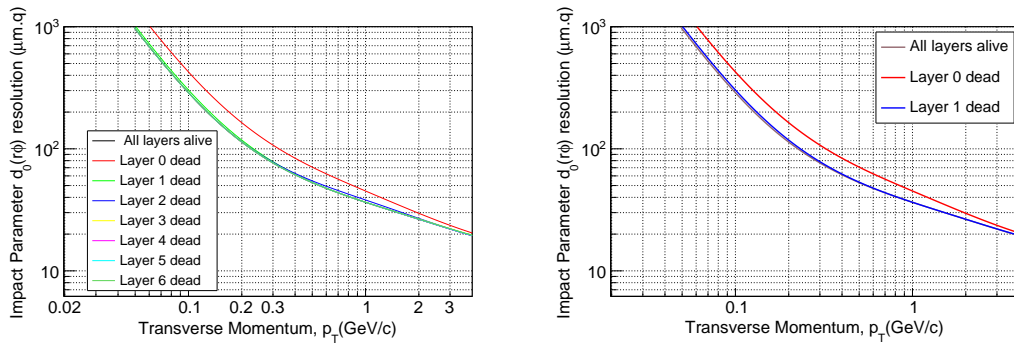


Figure 4.16: Impact parameter resolution for the upgraded ITS in the presence of dead layers. The right panel shows the worst case scenario which is compared to the case where all the layers are properly working.

4. DETECTOR PERFORMANCE

5

Conclusion

ALICE has an elaborate upgrade programme based on the upgrade of the LHC in 2018-19 during the second Long Shutdown (LS2). Within this upgrade strategy, the Inner Tracking System (ITS) upgrade forms an important cornerstone, providing improved vertexing and readout capabilities. The new ITS will consist of seven layers of Monolithic Active Pixel Sensors using the TowerJazz 0.18 μm technology.

The work presented in this thesis can be categorized in two parts. The first part concerns the results of characterization of some of the pixel prototype circuits developed for the ITS upgrade. The second part discusses the detector performance studies of the upgraded ITS.

The results of characterization of the prototype circuits: MIMOSA32, MIMOSA32Ter and Explorer-1 are presented. MIMOSA32 and MIMOSA32Ter were the first prototypes designed with the TowerJazz technology. The characterization results validated the technology in terms of charge collection and radiation tolerance. The results also concluded that the addition of a deep p-well (a feature of the technology) maintains satisfactory performance even after irradiation. This was a starting point for future prototypes with the deep p-well in a full CMOS process, thus allowing in-pixel sophisticated signal processing circuits. Thus the technology is qualified for the ALICE ITS upgrade pixel sensor.

Explorer-1 prototype circuits with different starting materials were also characterized. The results showed the dependence of the ratio of the collected charge to the input capacitance (Q/C) on the back bias voltage and the spacing between the collection electrode and the adjacent p-well. The results concluded that Q/C improves

5. CONCLUSION

with higher back bias voltage and increased spacing. The understanding of the Q/C ratio and its optimization would help towards building a final detector with reduced power consumption. This would provide a margin to reduce the material budget of the detection layers, improving the detector performance. With these results, the future prototypes of Explorer could concentrate on optimizing the size of the input transistors to study its effects on the Random Telegraph Signal noise. In parallel, optimization of the signal processing circuits would also be carried out in other prototypes.

The performance of a baseline configuration of the upgraded detector is presented in terms of impact parameter resolution, momentum resolution and tracking efficiency both in standalone tracking mode and ITS-TPC combined tracking. The performance was compared with the current ITS to study the improvements in the upgraded ITS. The performance is affected by the radial position and material budget of the layers and the detector intrinsic resolution. The detector specifications in this regard are still evolving specially for the Outer Barrel (the outermost four layers). The effects of variation of the specifications in terms of material budget and intrinsic resolution on the detector performance was studied. This would help to finalize the detector specifications for an optimized detector performance. The studies also concluded that a reduction in the beam pipe radius (lower than the baseline upgrade scenario) would not affect detector performance but may facilitate the installation of the Inner Barrel. Redundancy studies showed that the presence of a dead layer can degrade the detector performance significantly. This defines a key requirement of easy and rapid accessibility to the detector in the design of the upgraded ITS.

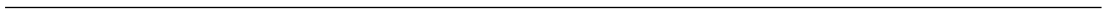
Presently, the first full scale pixel chip prototypes of the different design streams are being fabricated. Throughout 2014 and early 2015 the characterization and further optimizations of these full scale prototypes will be carried out which will lead towards a decision on the final architecture for the upgrade. The submission of a prototype final circuit for the ITS upgrade is foreseen in late 2015. Mass production of the final circuit is planned for 2016. The construction of the detector modules, tests, assembling and pre-commissioning will be carried out throughout 2016-2017. The detector will be commissioned at surface in late 2018 and will be installed in the ALICE cavern in 2019. In 2020, the upgraded ALICE detector will start its operations for the high luminosity Pb-Pb run.

Acknowledgements

The work of this thesis was financially supported by the Department of Physics, University of Cagliari in the form of *Assegno di Ricerca*. INFN Cagliari provided the infrastructural facilities and travel support. The ALICE Italy collaboration gave me a chance to work on my thesis work as a INFN fellow at CERN in 2013.

I collaborated with Gianluca Usai, Davide Marras, Alberto Collu and Carlo Pugioni to develop the test system for the MIMOSA sensors with useful inputs from the IPHC Strasbourg group. Valerio Altini helped to develop the data monitoring software. Thanushan Kugathasan, one of the developers of the Explorer sensors, helped me with the correction of the draft concerning the Explorer sensors. Jacobus van Hoorne is one of the main developers of the analysis framework of the Explorer sensors which I have used for studying the Explorer-1 sensor. Paolo Martinengo was responsible for the test beam organisation for the pixel sensors. Felix Reidt was responsible for the development of the test system of the Explorer sensors. Hartmut Hillemanns organized the irradiation of the MIMOSA and Explorer sensors.

I acknowledge the discussions with Giuseppe Bruno, Massimo Masera, Ruben Shakhoyan, Luciano Musa, Andrea Dainese, Jouri Belicov and Cristina Terrevoli on the experimental conditions, detector specifications and detector performance estimation in the ALICE upgrade scenerio. Corrado Gargiulo and Vito Manzari provided me with the details of the mechanical aspects of the new ITS.



Thank you ..

आ नो भद्राः क्रतवो यन्तु विश्वतः अदब्धासो अपरीतास उद्भिदः

This is a saying in Sanskrit from one of the most ancient scriptures, the *Rig Veda*. The literal meaning is something like this: *let knowledge or noble thoughts come from everywhere, never deceived, unhindered and victorious*. This is true for my PhD. I never planned to do a PhD in physics with an engineering background. It was possible due to the invaluable experience I gained from my association with ALICE in different detector collaborations, before enrolling into and also during my PhD. I would like to take this opportunity to thank all my friends in ALICE from whom I have learnt so much in the past years. It is difficult to acknowledge their true support in these few pages.

I would like to thank Gianluca Usai, Corrado Cicalo, Alberto Masoni, Alessandro De Falco, Giovanna Puddu, Davide Marras, Mauro Arba, Alberto Collu, Carlo Pugioni, Marcellino Tuveri, Mariano Cadoni, Umberto D'Alesio, Daniele Mura, Alessandro Cardini, Sandro Cadeddu, Paolo Randaccio, Viviana Fanti, Biaggio Saitta, Paolo Ruggerone, Antonio Silvestri, Cristina Terrevoli, Elisa Incani, Ester Casula, Luigi La Delfa, Maria Grazia Dessi, Francesca Maccioni, Maria Assunta Lecca, Eloisa Piludu and all my colleagues from Cagliari for their support over the past years. I am grateful to Tiziana Cubeddu for her continuous help in the past many years.

Many thanks to Luciano Musa, Vito Manzari, Massimo Maserà, Andrea Dainese, Petra Riedler, Hartmut Hillemanns, Thanushan Kugathasan, Paolo Martinengo, Felix Reidt, Costanza Cavichhioli, Cesar Augusto Marin Tobon, Markus Keil, Magnus Mager, Walter Snoyes, Monica Kofarago and all my colleagues from the ITS upgrade collaboration. The support from Jacobus van Hoorne and Giuseppe Bruno was fundamental.

Apart from the ALICE ITS upgrade collaboration, my association with the ALICE Zero Degree Calormeter (ZDC) and the Dimuon Spectrometer collaborations played a

very important part in my career. I am thankful to all my collaborators and friends from these collaborations.

Life in ALICE and at CERN wouldn't have been great without the privileged company of my friends Federico Ronchetti, Gilda Scioli, Michele Floris, Caterina Deplano, Indranil Das, Martino Gagliardi, Livio Bianchi, Francesco Bossu, Barbara Guerzoni, Ombretta Pinazza, Torsten Alt, Paolo Mereu, Pietro Cortese, Alessandro Ferretti, Roberto Divia, Franco Carena, Artur Szostak, Paola La Rocca, Grazia Luparello, Giacomo Volpe, Giacomo Contin, Andrea Alici, Daniele De Gruttola, Stefania Bufalino, Chiara Oppedisano, Adriana Telesca, Francesca Bellini and many others. The enlightening discussions with my friend Rob Veenhof was a privilege.

I am grateful to Swapan Sen, Sandip Sarkar and Sukalyan Chattopadhyay of SINP, India who were instrumental in my participation in the ALICE collaboration.

I would like to acknowledge the overwhelming support of my friends in Cagliari, specially Paolo Seu, Caterina Falconi, Ivo Pirisi, Gianmario Mereu, Walter Serrau, Callisto Pili, Elisabetta Siddi, Stefania Basciu, Cinzia Mocci, Stefano Scordo, Luca Pilia, Davide Espa, Daniele Siddi, Fabio Carta, Claudia Caddeo, Maria Carla Zurru and Simona Zurru. I will never have enough words to thank my friend Corrado Cicalo, whose support has always been fundamental. My friend, Sara La Sala influenced some of my choices for the quotations used in the beginning of this document. It may rightly seem that there are too many quotes, but it is just due to my fascination towards Indo - European languages and ancient scriptures.

My friends in India, the great Heras of Hera Thek - Arkadeb Ghosal, Tanmay Chakraborty, Anirban Majumdar, Soumyajyoti Chakrabarty, Sumit Paul, Santanu Das, Santanu Sarkar, Mrinmay Biswas, Arup Chatterjee, Biplab Halder, Amitabh Saha, Pinaki Roy, Moloy Das, Yogiraj Ray and many others have always been a motivational force. I have always received great support from my friends Somtirtha Ganguly, Partha Dhar Gupta, Subhrajyoti Mukherjee, Subhrajyoti Pramanik and Subhamoy Majumdar.

I am grateful to my parents Gayotri Siddhanta and Subhamoy Siddhanta, my brother Satyarup Siddhanta and my uncles Ashish Siddhanta, Shyamal Chandra Majumdar, Debaprasad Chaudhuri and their families who always supported my strange academic choices.

I consider my PhD as an important part of a continuous journey in my research career. This journey started in ALICE and I hope that it will continue in the future.

Bibliography

- [1] ALICE Collaboration. ALICE: Physics Performance Report, Vol. I. *J. Phys.*, G30:1517–1763, 2004. doi:10.1088/0954-3899/30/11/001. 1
- [2] ALICE Collaboration. ALICE: Physics Performance Report, Vol. II. *J. Phys.*, G32:1295, 2006. doi:10.1088/0954-3899/32/10/001. 1
- [3] ALICE Collaboration. The ALICE experiment at the CERN LHC. *JINST*, 3(S08002), 2008. doi:10.1088/1748-0221/3/08/S08002. 1
- [4] ALICE Collaboration. Upgrade of the ALICE Experiment: Letter of Intent. Technical Report CERN-LHCC-2012-012,LHCC-I-022, CERN, Geneva, 2012. URL: <http://cds.cern.ch/record/1475243?ln=en>. 6
- [5] ALICE Collaboration. Addendum of the Letter Of Intent for the Upgrade of the ALICE Experiment: The Muon Forward Tracker. Technical Report CERN-LHCC-2013-014, LHCC-I-022-ADD-1, CERN, Geneva, 2013. URL: <https://cds.cern.ch/record/1592659?ln=en>. 6
- [6] L. Musa et al. Technical Design Report for the Upgrade of the ALICE Inner Tracking System. Technical Report CERN-LHCC-2013-024, CERN, Geneva, Nov 2013. URL: <https://cds.cern.ch/record/1625842?ln=en>. 6, 10, 47, 64, 65, 66, 67, 68, 74, 75, 76, 77
- [7] The Particle Data Group. Review of particle physics. *Phys. Rev. D.*, 86(1):010001, 2012. doi:10.1103/PhysRevD.86.010001. 7, 14
- [8] M. He, R. J. Fries, R. Rapp. D_s meson as a quantitative probe of diffusion and hadronization in nuclear collisions. *Phys. Rev. Lett.*, 110(112301), 2013. doi:10.1103/PhysRevLett.110.112301. 8

BIBLIOGRAPHY

- [9] Y. Oh et al. Ratios of heavy baryons to heavy mesons in relativistic nucleus-nucleus collisions. *Phys. Rev. C*, 79(044905), 2009. doi:10.1103/PhysRevC.79.044905. 8
- [10] A. Grelli et al. (ALICE Collaboration). Quark Matter 2012, Washington D.C, 2012. URL: <http://qm2012.bnl.gov>. 8, 9
- [11] S. Sakai et al. Quark Matter 2012, Washington D.C, 2012. URL: <http://qm2012.bnl.gov>. 8, 9
- [12] L. Musa et al. Upgrade of the Inner Tracking System Conceptual Design Report. Technical Report CERN-LHCC-2012-013, LHCC-P-005, CERN, Geneva, Aug 2012. URL: <http://cds.cern.ch/record/1475244?ln=en>. 10
- [13] L. Rossi, P. Fischer, T. Rohe, N. Wermes. *Pixel Detectors: From Fundamentals to Applications*. Springer, 2005. 14, 17
- [14] W. R. Leo. *Techniques for Nuclear and Particle Physics Experiments: A how-to approach*. Springer-Verlog, 1994. 14, 16
- [15] L. Landau. On the energy loss of fast particles by ionization. *J. Phys. USSR*, 8(201), 1944. 15
- [16] P. V. Vavilov. Ionization losses of high energy heavy particles. *Soviet Physics JETP*, 5(749), 1957. 15
- [17] O. Blunck and S. Leisegang. Zum energieverlust schneller elektronen in dünnen schichten. *Z. Physik*, 128(500), 1950. 15
- [18] P. Shulek et al. Fluctuations of ionization loss. *Sov. J. Nucl. Phys*, 4(400), 1967. 15
- [19] H. Bichsel. Straggling of heavy charged particles: Comparison of born hydrogenic-wave-function approximation with free-electron approximation. *Phys. Rev.*, B1(2854), 1970. doi:10.1103/PhysRevB.1.2854. 15
- [20] G. R. Lynch, O. I. Dahl. Approximations to multiple coulomb scattering. *Nucl. Instrum. Methods*, B(58):6–10, 1991. doi:10.1016/0168-583X(91)95671-Y. 15, 83

- [21] L. Greiner et al. A MAPS based vertex detector for the STAR experiment at RHIC. *Nucl. Instrum. Meth.*, A650(1):68–72, 2011. doi:{10.1016/j.nima.2010.12.006}. 18, 64
- [22] J. A. Ballin et al. Monolithic Active Pixel Sensors (MAPS) in a quadruple well technology for nearly 100% fill factor and full CMOS pixels. *Sensors*, 8(9):5336, 2008. doi:{10.3390/s8095336}. 21
- [23] W. Snoeys et al. Layout techniques to enhance the radiation tolerance of standard CMOS technologies demonstrated on a pixel detector readout chip. *Nucl.Instr. and Meth. in Phys. Res.*, A(439):349–360, 2000. doi:10.1016/S0168-9002(99)00899-2. 33
- [24] S. Siddhanta et al. The Readout System for the ALICE Zero Degree Calorimeters. *IEEE Transactions of Nuclear Science*, 58(4):1759–1765, 2011. doi:10.1109/TNS.2011.2159514. 35
- [25] M. Deveaux et al. Random telegraph signal in monolithic active pixel sensors. *IEEE Nuclear Science Symposium Conference Record*, ():3098–3105, 2008. doi:10.1109/NSSMIC.2008.4775010. 46
- [26] W. Snoeys. Monolithic pixel detectors for high energy physics. *Nucl.Instr. and Meth.*, A(731):125, 2013. doi:10.1016/j.nima.2013.05.073. 47
- [27] S. Martoiu, H. Muller, A. Tarazona, J. Toledo. Development of the scalable readout system for micro-pattern gas detectors and other applications. *JINST*, 8:C03015, 2013. doi:10.1088/1748-0221/8/03/C03015. 52
- [28] G. Schneider. Installation of the central beryllium beam pipe in the alice experiment. EDMS: 1113439, 2011. URL: <https://edms.cern.ch/document/1113439/2>. 72
- [29] ALICE Collaboration. Charged-particle multiplicity density at midrapidity in central pb-pb collisions at $\sqrt{S_{NN}} = 2.76$ tev. *Phys. Rev. Lett.*, 105:252301, Dec 2010. doi:10.1103/PhysRevLett.105.252301. 72

BIBLIOGRAPHY

- [30] X. Wang, M. Gyulassy. Hijing: A monte carlo model for multiple jet production in pp, pa, and aa collisions. *Phys. Rev. D*, 44:3501–3516, Dec 1991. doi:10.1103/PhysRevD.44.3501. 72
- [31] A. Alscher, K. Hencken, D. Trautmann, G. Baur. Multiple electromagnetic electron-positron pair production in relativistic heavy-ion collisions. *Phys. Rev. A*, 55:396–401, 1997. doi:10.1103/PhysRevA.55.396. 73
- [32] K. Hencken, G. Baur, D. Trautmann. Production of QED pairs at small impact parameter in relativistic heavy ion collisions. *Phys. Rev. C*, 69:054902, 2004. doi:10.1103/PhysRevC.69.054902. 73
- [33] K. Hencken, Y. Kharlov, S. Sadovsky. Ultraperipheral trigger in alice. ALICE-INT-2002-11, 2002. URL: <https://edms.cern.ch/document/357571/1/ALICE-INT-2002-011.pdf>. 73
- [34] S. Sadovsky, K. Hencken, Y. Kharlov. Generator for e^+e^- pairs in pbbp collisions at lhc. ALICE-INT-2002-27, 2002. URL: <https://edms.cern.ch/document/357571/1/ALICE-INT-2002-027.pdf>. 73
- [35] AliRoot: ALICE Off-line framework for simulation, reconstruction and analysis . <http://aliceinfo.cern.ch/Offline>. URL: <http://aliceinfo.cern.ch/Offline>. 73, 81
- [36] P. Billoir. Track fitting with multiple scattering: A new method. *Nuclear Instruments and Methods in Physics Research*, 225:352 – 366, 1984. doi:DOI:10.1016/0167-5087(84)90274-6. 77, 81
- [37] R. Frühwirth. Application of kalman filtering to track and vertex fitting. *NIM*, A262:444–450, 1987. doi:http://dx.doi.org/10.1016/0168-9002(87)90887-4. 77, 81
- [38] O. Brüning, P. Collier, P. Lebrun, S. Myers, R. Ostojic, J. Poole, P. Proudlock. *LHC Design Report*. CERN, Geneva, 2004. doi:10.5170/CERN-2004-003-V-1. 80
- [39] STAR Collaboration. The STAR heavy flavor tracker, conceptual design report. submitted to DOE at CD1 review, 2009. URL: http://phys.kent.edu/~margetis/hft/HFT_CDR_Final.pdf. 81

BIBLIOGRAPHY

- [40] A. Mastroserio et al. Simulation tools for the its upgrade. ALICE Internal Note, 2012. URL: http://aliceinfo.cern.ch/ITSUpgrade/sites/aliceinfo.cern.ch/ITSUpgrade/files/documents/Upgrade_IN.pdf. 81